TAMPEREEN TEKNILLINEN YLIOPISTO
TAMPERE UNIVERSITY OF TECHNOLOGY

Juha Harra

On the Synthesis, Morphology, and Applications of Engineered Aerosol Nanoparticles

Julkaisu 1345 • Publication 1345

Tampere 2015

Tampereen teknillinen yliopisto. Julkaisu 1345
Tampere University of Technology. Publication 1345

Juha Harra

On the Synthesis, Morphology, and Applications of Engineered Aerosol Nanoparticles

Thesis for the degree of Doctor of Science in Technology to be presented with due permission for public examination and criticism in Tietotalo Building, Auditorium TB104, at Tampere University of Technology, on the 20th of November 2015, at 12 noon.

Tampereen teknillinen yliopisto - Tampere University of Technology
Tampere 2015

Doctoral candidate: Juha Harra, M.Sc.
Aerosol Physics Laboratory
Department of Physics
Tampere University of Technology
Tampere, Finland

Supervisor: Jyrki Mäkelä, Prof.
Aerosol Physics Laboratory
Department of Physics
Tampere University of Technology
Tampere, Finland

Pre-examiners: Jorma Jokiniemi, Prof.
Fine Particle and Aerosol Technology Laboratory
Department of Environmental Science
University of Eastern Finland
Kuopio, Finland

Martin Seipenbusch, Dr.
Particle-based Functional Materials
Institute of Chemical Process Engineering
University of Stuttgart
Stuttgart, Germany

Opponent: Georgios Sotiriou, Dr.
Institute of Pharmaceutical Sciences
Department of Chemistry and Applied Biosciences
ETH Zürich
Zürich, Switzerland

ISBN 978-952-15-3628-1 (printed)
ISBN 978-952-15-3648-9 (PDF)
ISSN 1459-2045

Abstract

Nanotechnology, the manipulation of matter at the scale of 1 – 100 nm, is present in everyday life and continues extending into new areas of application. Aerosol synthesis routes, the production of nanoparticles in the gas phase, are known to be continuous, highly controllable, and even suitable for fabricating different types of nanostructured metamaterials—materials with properties not found in nature. In this thesis, single and multicomponent engineered aerosol nanoparticles with different morphologies were synthesized for applications involving interactions between light and matter. The synthesized nanoparticles included spherical silver particles, titania-encapsulated iron oxide particles, silver-decorated silica particles, and silver – titania composite doublet particles. Furthermore, the studied applications for the nanoparticles were magnetically separable photocatalyst nanopowders and nanostructured metal – dielectric metamaterials with linear and nonlinear optical properties, more specifically, localized surface plasmon resonance and second-harmonic generation, respectively.

The aerosol synthesis techniques utilized for the nanoparticle production in this thesis included particle size selection, sintering, encapsulation, and coating. The sintering of the size-selected silver agglomerates to spheres continued the trends found from the literature. In the simple encapsulation process, liquid precursor containing solid particles was sprayed into a tubular furnace where the precursor thermally decomposed on the surface of the solid particles, forming multicomponent particles. This approach was demonstrated by synthesizing titania-encapsulated iron oxide particles. As titania and iron oxide are known to be photocatalytic and magnetic, respectively, the produced nanopowder could find use as a magnetically separable photocatalyst. The silver coatings on the silica and titania carrier particles, accomplished by physical vapor condensation, were found to form different types of morphologies due to the migration of the silver on the carrier particles.

The wavelength of the localized surface plasmon resonance of spherical silver particles deposited on glass substrates was tuned between 400 – 450 nm with the particle size. Due to the random deposition process, particle – particle contacts on the substrate caused broadening of the extinction spectrum with higher area fractions. On the other hand, the silver-decorated silica nanoparticles maintained the narrow plasmon resonance band even with high particle number densities. This enabled the fabrication of thicker bulk-type optical materials. The nonlinear optical properties of bulk-type multilayer nanostructures consisting of alternating layers of silver-decorated silica nanoparticles and pure silica were investigated. It was proposed that the porous particle layers were in a key role in the formation of the required non-centrosymmetric structure. Furthermore, both the silver particles and the multilayer structure were important for the second-harmonic generation, whose intensity increased with the number of layers. The fabricated structures could be further optimized in order to increase the conversion efficiency of the second-order nonlinear optical process.

Tiivistelmä

Nanoteknologia, aineen manipulointi 1 – 100 nm mittakaavassa, hyödyttää ihmisiä arjessa ja tuottaa jatkuvasti uusia keksintöjä. Aerosolisynteesimenetelmillä nanohiukkasia voidaan tuottaa kaasufaasissa jatkuvasti ja hallitusti. Lisäksi aerosolimenetelmiä voidaan hyödyntää nanorakenteisten metamateriaalien valmistuksessa. Metamateriaalit ovat keinotekoisia materiaaleja, joiden ominaisuudet eroavat luonnonmateriaaleista. Tässä työssä tuotettiin yksi- ja monikomponenttisia aerosolinanohiukkasia erilaisilla morfologioilla sovelluskohteisiin, jotka liittyvät valon ja aineen vuorovaikutukseen. Tuotetut nanohiukkaset olivat pallomaisia hopeahiukkasia, titaanidioksidilla koteloituja rautaoksidihiukkasia, hopeakoristeltuja silikahiukkasia ja hopea – titaanidioksidikaksoishiukkasia. Tutkittuja sovelluskohteita olivat magneettisesti eroteltavat fotokatalyyttiset nanojauheet ja nanorakenteiset metalli – dielektriset metamateriaalit, joilla on lineaarisia ja epälineaarisia optisia ominaisuuksia kuten hiukkasten pintaplasmoniresonanssi ja taajuuden kahdennus.

Tässä työssä käytettyjä aerosolisynteesimenetelmiä olivat hiukkaskoon valitseminen, sintraus, kotelointi ja päällystäminen. Tulokset kokovalikoitujen hopea-agglomerattien sintraamisesta pallomaisiksi olivat yhdenmukaisia kirjallisuudesta löytyvien tulosten kanssa. Yksinkertaisessa kotelointiprosessissa nestemäinen prekursori, joka sisälsi kiinteitä hiukkasia, pirskotettiin putkiuuniin. Uunissa prekursori hajosi termisesti koteloiden kiinteän hiukkasen sisäänsä. Tällä menetelmällä tuotettiin titaanidioksidilla koteloituja rautaoksidihiukkasia. Koska titaanidioksidilla tiedetään olevan fotokatalyyttisiä ja rautaoksidilla magneettisia ominaisuuksia, valmistettua nanojauhetta voidaan mahdollisesti hyödyntää magneettisesti eroteltavana fotokatalyyttinä. Fysikaalisella höyryn kondensaatiolla tuotettujen hopeapäällysteiden havaittiin muodostavan erilaisia morfologioita silika- ja titaanidioksidihiukkasten päälle. Tämä johtui muodostuneiden hopeahiukkasten liikkeestä kantajahiukkasten päällä.

Lasialustalle kerättyjen hopeahiukkasten plasmoniresonanssin aallonpituutta säädettiin 400 – 450 nm välillä muuttamalla hiukkasten kokoa. Sattumanvaraisen keräysprosessin vuoksi hiukkasten väliset kontaktit levensivät ekstinktiospektriä, kun hiukkasten lukumäärä pinnalla kasvoi. Sen sijaan hopeakoristellut silikahiukkaset säilyttivät kapean resonanssikaistan jopa suurilla hiukkastiheyksillä. Näin ollen hiukkasista oli mahdollista rakentaa paksumpia optisia näytteitä. Tässä työssä tutkittiin monikerroksisten nanorakenteiden, jotka koostuivat vuorottelevista kerroksista hopeakoristeltuja silikahiukkasia ja puhdasta silikaa, epälineaarisia optisia ominaisuuksia. Hiukkaskerrosten huokoisuudella ajateltiin olevan suuri merkitys tarvittavan epäkeskussymmetrisen rakenteen muodostumisessa. Tämän lisäksi sekä hopeahiukkaset että kerrosrakenne olivat tärkeitä taajuuden kahdentumisessa, jonka voimakkuus riippui kerrosten lukumäärästä. Valmistettuja rakenteita voidaan vielä optimoida epälineaarisen optisen prosessin vahvistamiseksi.

Preface

The work presented in this thesis has been carried out at the Aerosol Physics Laboratory of the Department of Physics at Tampere University of Technology (TUT) during the years 2010 – 2015. The research was a part of a Finnish – Japanese project funded by the Academy of Finland (decision no. 136080). The financial support from the TUT's graduate school is greatly acknowledged. Furthermore, I thank for the personal grants given by the Jenny and Antti Wihuri Foundation and the Finnish Foundation for Technology Promotion (Tekniikan edistämissäätiö, TES).

I thank my supervisor Prof. Jyrki Mäkelä for giving me both guidance and liberties at an optimized ratio. The pre-examiners, Prof. Jorma Jokiniemi and Dr. Martin Seipenbusch, are acknowledged for their helpful comments and suggestions. Anssi Arffman and Heino Kuuluvainen are to thank for kindly "peer-reviewing" this thesis. All the co-authors of the publications included in this thesis, without whom the papers would not have seen the daylight, deserve major credit. Especially, I want to mention Paxton Juuti for helping me in the laboratory measurements, and Dr. Mikko Aromaa, Dr. Eleftheria Roumeli, and Dr. Jaakko Yli-Ojanperä for the interesting discussions. Dr. Mariusz Zdanowicz, Dr. Jouni Mäkitalo, and Matti Virkki, as well as, Prof. Martti Kauranen and Prof. Goëry Genty from the Optics Laboratory of the Department of Physics at TUT introduced me to the curious world of nonlinear optics. The material characterization would not have succeeded without the substantial help from Juha-Pekka Nikkanen and Dr. Mari Honkanen from the Department of Materials Science at TUT. Veli-Pekka Plym from the workshop of the Department of Physics is acknowledged for building some of the tools required to accomplish this task.

I thank Heino Kuuluvainen and Dr. Matti Happonen, fellow doctoral candidates, who have shared the office room with me during my efforts, for numerous critical discussions about science and everything. The management, Prof. Jorma Keskinen in front, as well as, all the current and former employees of the Aerosol Physics Laboratory are to thank for creating an extremely pleasant working environment. Aero café, the not too official meeting place of the laboratory, has truly being a forum where no topic is beyond any scope.

My parents, siblings, and all my friends deserve my gratitude for showing very little interest towards my efforts in the nanoscale. Instead, they have managed to keep me in a world much larger in scale. Mom, I miss you, and I wish you could still be here. Finally, my wife Jenni, even though I don't say it too often, your support has been priceless. Also, I thank and blame you for introducing me to the great socializer known as coffee.

Tampere, October 2015
Juha Harra

Contents

Abstract **iii**

Tiivistelmä **v**

Preface **vii**

Symbols and abbreviations **xi**

List of publications **xiii**

Author's contribution **xv**

1 Introduction **1**
1.1 Aim and scope 3

2 Engineered aerosol nanoparticles **5**
2.1 Generation of nanoparticles 5
2.2 Particle size, shape, and morphology 6
2.3 Aerosol-assisted fabrication of metamaterials 8

3 Light and nanostructures **11**
3.1 Localized surface plasmon resonance 11
3.2 Second-harmonic generation 12
3.3 Photocatalysis on titania 13

4 Experimental methods **15**
4.1 Synthesis 15
4.2 Deposition 17
4.3 Characterization 19

5 Results and discussion **23**
5.1 Tailoring the particle morphology 23
5.2 Applications 30

6 Conclusions and final remarks **37**

Bibliography **39**

Publications **51**

Symbols and abbreviations

θ	angle of incidence (°)
λ	wavelength (nm)
Ag	silver
CVS	chemical vapor synthesis
CPC	condensation particle counter
CS	condensation sink
d	particle diameter (nm)
DMA	differential mobility analyzer
EC	evaporation–condensation
EDS	energy-dispersive X-ray spectroscopy
ELPI	electrical low pressure impactor
ESP	electrostatic precipitator
Fe_2O_3	iron oxide
FIB	focused ion beam
GMD	geometric mean diameter (nm)
GSD	geometric standard deviation
IPA	isopropyl alcohol
LFS	liquid flame spray
LSPR	localized surface plasmon resonance
MB	methylene blue
N_2	nitrogen
SAED	selected area electron diffraction
SEM	scanning electron microscope
SHG	second-harmonic generation

SiO_2	silicon dioxide (a.k.a. silica)
SMPS	scanning mobility particle sizer
T	temperature (°C)
TEM	transmission electron microscope
TEOS	tetraethyl orthosilicate
TiO_2	titanium dioxide (a.k.a. titania)
TTIP	titanium isopropoxide
UV–Vis	ultraviolet–visible spectroscopy
XRD	X-ray diffraction

List of publications

This thesis is a compound thesis consisting of an introductory review and the following four publications, which are cited in the text according to their roman numerals presented below. The publications are reproduced with kind permissions from the publishers.

Paper I Juha Harra, Jouni Mäkitalo, Roope Siikanen, Matti Virkki, Goëry Genty, Takayoshi Kobayashi, Martti Kauranen, and Jyrki M. Mäkelä, "Size-controlled aerosol synthesis of silver nanoparticles for plasmonic materials," *Journal of Nanoparticle Research*, vol. 14, no. 6, p. 870, 2012. doi: 10.1007/s11051-012-0870-0

Paper II Juha Harra, Juha-Pekka Nikkanen, Mikko Aromaa, Heikki Suhonen, Mari Honkanen, Turkka Salminen, Saara Heinonen, Erkki Levänen, and Jyrki M. Mäkelä, "Gas-phase synthesis of encapsulated iron oxide – titanium dioxide composite nanoparticles by spray pyrolysis," *Powder Technology*, vol. 243, pp. 46 – 52, 2013. doi: 10.1016/j.powtec.2013.03.027

Paper III Juha Harra, Paxton Juuti, Janne Haapanen, Miika Sorvali, Eleftheria Roumeli, Mari Honkanen, Minnamari Vippola, Jaakko Yli-Ojanperä, and Jyrki M. Mäkelä, "Coating of silica and titania aerosol nanoparticles by silver vapor condensation," *Aerosol Science and Technology*, vol. 49, no. 9, pp. 767 – 776, 2015. doi: 10.1080/02786826.2015.1072263

Paper IV Mariusz Zdanowicz, Juha Harra, Jyrki M. Mäkelä, Esa Heinonen, Tingyin Ning, Martti Kauranen, and Goëry Genty, "Ordered multilayer silica-metal nanocomposites for second-order nonlinear optics," *Applied Physics Letters*, vol. 103, no. 25, p. 251907, 2013. doi: 10.1063/1.4852795

Author's contribution

All of the publications included in this thesis are a result of collaborations with other researchers. Here, brief summaries of the publications are presented along with the author's contribution.

Paper I Spherical size-selected silver nanoparticles were synthesized by evaporation–condensation and deposited on glass substrates as quasilayers of particles. The optical plasmonic properties of these metamaterials were investigated. The author planned and executed the fabrication of the metamaterials, analyzed the measurement data, and wrote most of the paper.

Paper II Titania-encapsulated iron oxide nanoparticles were synthesized by spray pyrolysis and collected into a nanopowder whose photocatalytic and magnetic properties were studied. The author planned and executed the production of the nanopowder, analysed the measurement data, and wrote most of the paper.

Paper III Silica and titania nanoparticles were coated with silver by physical vapor condensation. The author planned and executed the production of the nanoparticles. With the exception of the crystallinity analyses, the measurement data was analyzed by the author. Moreover, the author wrote most of the paper.

Paper IV Multilayer nanostructures consisting of alternating layers of silver-decorated silica nanoparticles and pure silica were fabricated. The linear and nonlinear optical properties of the fabricated metamaterials, plasmon resonance and second-harmonic generation, respectively, were studied. The first authorship was shared between the author and Mariusz Zdanowicz, who was responsible of the optical measurements and analyses. The author planned and executed the generation of the nanoparticles, and analyzed the aerosol and microscope data. Furthermore, the author prepared all of the figures and co-wrote the paper.

1 Introduction

"There's plenty of room at the bottom", a lecture given by Richard Feynman in 1959 (Feynman, 1992), is considered the conceptual launch for nanotechnology, a term later coined in the mid-1970s (Taniguchi, 1974). Nanotechnology can be understood as the manipulation of matter in the scale of $1-100$ nanometer, one billionth of a meter. Even though such dimensions are a few orders of magnitude larger than the size of a single atom, they are still beyond the scope of optical microscopy. Thus, the nanoworld began to truly unravel just a few decades ago, after the enormous progress in the characterization and manipulation of nano-sized features. Nowadays, the products of nanotechnology are an invisible but inseparable part of the everyday life, not to mention what nanotechnology has to offer for the future. Nanoparticles and -structures can be found from building materials, health products, textiles, food supplies, and sports equipment, to mention but a few. Moreover, current state-of-the-art nanotechnology enables the fabrication of metamaterials—artificial materials with properties novel even to nature.

The properties of nanoparticles differ from the corresponding bulk material due to their extremely small dimensions. For instance, the interaction between light and a nanoparticle is highly localized, enabling the fabrication of smaller optical devices. Furthermore, the increased surface area with decreased particle size, as volume stays constant, is relevant for catalytic reactions taking place on the material surfaces. Besides the particle size, also the shape of the particles determines many of their properties. Nanosized spheres, cubes, rods, and tubes, all have their own distinct properties and areas of application. Even more complex particle structures can be achieved when different materials are combined at the nanoscale. This gives the opportunity to engineer multicomponent nanoparticles with either enhanced or multiple unique properties. In order to take full advantage of these multicomponent nanoparticles, the control over the morphology of the produced particles is highly important.

Several different techniques, utilizing solid, liquid, and gas phase processes, have been used in the production of nanomaterials. These techniques can be roughly divided into two categories, top-down and bottom-up. In the former approach, larger bulk pieces are reduced in size, until the nanoscale is reached. Examples of techniques that follow the top-down principle are, for example, mechanical grinding and lithography, which can be used for fabricating arrays of different shaped nanostructures on a substrate (Haynes and Van Duyne, 2001). In the latter approach, nanoparticles are assembled from individual atoms or molecules. The bottom-up techniques include, for instance, the production of nanoparticle colloids through chemical reactions in a solution. These wet chemistry techniques have been used for synthesizing both single and multicomponent nanoparticles with various different shapes (Liz-Marzán, 2004).

Besides solid and liquid phase, nanoparticles can also be synthesized in the gas phase

through both physical and chemical reactions. In the aerosol-based production of nanomaterials, the generation, as well as, the tailoring of the particle size, shape, and morphology can be realized in the gas phase. Several upsides follow from this, such as, the synthesis processes are highly controllable, pure, continuous, inexpensive, and scalable (Kruis et al., 1998; Strobel and Pratsinis, 2007; Swihart, 2003). Moreover, the particles can be monitored *in situ* during the synthesis processes with aerosol measurement instruments that give information regarding, for example, the particle size, density, chemical composition, and concentration (Hinds, 1999; Kulkarni et al., 2011). In addition, the individual nanoparticles can be deposited on a desired substrate directly from the gas phase, thus, aerosol nanoparticles can be used in the fabrication of nanostructured metamaterials.

Currently, aerosol-synthesized nanoparticles, such as, carbon black, fumed silica, and pigmentary titania, are produced annually several million metric tons (Skillas et al., 2011) for everyday products, including, car tires, paints, foods, toothpastes, sunscreens, and many others (Elvers, 2009). Moreover, an ongoing European project aims to scale-up the aerosol-production of metal nanoparticles by physical synthesis methods to 100 kg/day (BUONAPART-E, 2014). Recent advances in the synthesis of engineered nanoparticles by aerosol methods have included the introduction of, for example, crumpled graphene particles (Luo et al., 2011), coated Janus-like hybrid particles (Sotiriou et al., 2011a), and semiconductor nanowires (Heurlin et al., 2012), any of which that could very well be the next success stories in the field of nanotechnology.

Evidently, the products of nanotechnology are utilized at ever increasing rate. Thus, in order to build improved and novel nanosystems, it is important to increase the understanding in the manipulation of the engineered nanoparticles. In this thesis, different methods for the synthesis of single and multicomponent aerosol nanoparticles are presented and studied, with the emphasis on the size, shape, and morphology tailoring of the particles for applications involving interactions between light and matter. The engineered aerosol nanoparticles synthesized in this thesis include spherical silver particles (**Paper I**), titania-encapsulated iron oxide particles (**Paper II**), silver-decorated silica particles (**Paper III** and **IV**), and silver–titania composite doublet particles (**Paper III**). Furthermore, the applications for the engineered nanoparticles include magnetically separable photocatalyst nanopowders (**Paper II**), as well as, nanostructured metamaterials with linear and nonlinear optical properties, more specifically, localized surface plasmon resonance (**Paper I** and **IV**) and second-harmonic generation, respectively (**Paper IV**).

In Chapter 2 of this thesis, relevant aerosol processes for the synthesis of engineered nanoparticles are reviewed. They include the generation of aerosol nanoparticles via the gas-to-particle and the liquid-to-particle conversion, as well as, methods for tailoring the size, shape, and morphology of single and multicomponent aerosol nanoparticles. Furthermore, the aerosol-assisted fabrication of metamaterials is briefly discussed. The applications for the fabricated nanostructured metamaterials explored in this thesis involve interaction between light and matter. These applications, localized surface plasmon resonance, second-harmonic generation, and photocatalysis, are introduced in Chapter 3. The experimental methods, including synthesis, deposition, and characterization of the engineered aerosol nanoparticles and fabricated metamaterials, as well as, the obtained results are reviewed in Chapter 4 and 5, respectively. The introductory review of this thesis concludes with the final remarks presented in Chapter 6. The publications included in this thesis are appended in the end of the thesis.

1.1 Aim and scope

This doctoral thesis aims to provide new information on the synthesis and applications of engineered single and multicomponent nanoparticles produced with aerosol techniques. The size, shape and morphology of the particles are tailored in the gas phase using methods, such as, sintering, encapsulation, and coating. Furthermore, the synthesized nanoparticles are incorporated into metamaterials with linear and nonlinear optical properties. The main objectives of this thesis are formulated below.

- Develop and study processes for tailoring the size, shape, and morphology of single and multicomponent engineered aerosol nanoparticles
- Incorporate the engineered aerosol nanoparticles into metamaterials by a direct deposition from the gas phase
- Investigate the linear and nonlinear optical properties of the metamaterials fabricated by the aerosol-assisted methods

The first objective was realized in all publications of this thesis. More specifically, size-selected spherical silver nanoparticles were produced by sintering in **Paper I**, whereas, in **Paper III**, a physical vapor coating process was used to produce silver-decorated silica nanoparticles, as well as, rather surprisingly silver–titania composite doublet particles. Moreover, in **Paper II**, a simple particle encapsulation method was introduced, and the technique was demonstrated by synthesizing titania-encapsulated iron oxide nanoparticles.

The second objective was realized in **Paper II**, where the produced particles were collected into a nanopowder with photocatalytic and magnetic properties. Furthermore, in **Paper I** and **IV**, the synthesized nanoparticles were deposited on glass substrates in order to fabricate quasilayer and multilayer nanostructures, respectively. Moreover, the linear and nonlinear optical properties of these metamaterials were characterized, connecting to the final objective of this thesis. A linear optical property of metal nanoparticles, localized surface plasmon resonance, was studied in **Paper I** and revisited again in **Paper IV**. In **Paper IV**, aerosol techniques were used, for the first time, in the fabrication of nonlinear optical metamaterials. More specifically, the used techniques allowed the fabrication of novel bulk-type structures with second-order nonlinear optical properties.

2 Engineered aerosol nanoparticles

2.1 Generation of nanoparticles

The synthesis routes for aerosol nanoparticles can be roughly divided into two categories, gas-to-particle and droplet-to-particle (Gurav et al., 1993; Skillas et al., 2011), as depicted in Figure 2.1. In the former synthesis route, the particles are formed from the individual atoms or molecules of the gas via a nucleation process. The required supersaturation for the nucleation is achieved by either cooling the vapor or by generating atoms or molecules from gaseous precursors through chemical reactions. The nucleated particles grow by condensation of the vapor atoms or molecules, and coagulation with other particles. As this is a bottom-up approach, the obtained particle sizes can be extremely small. However, the gas-to-particle route usually leads to highly agglomerated nanoparticles.

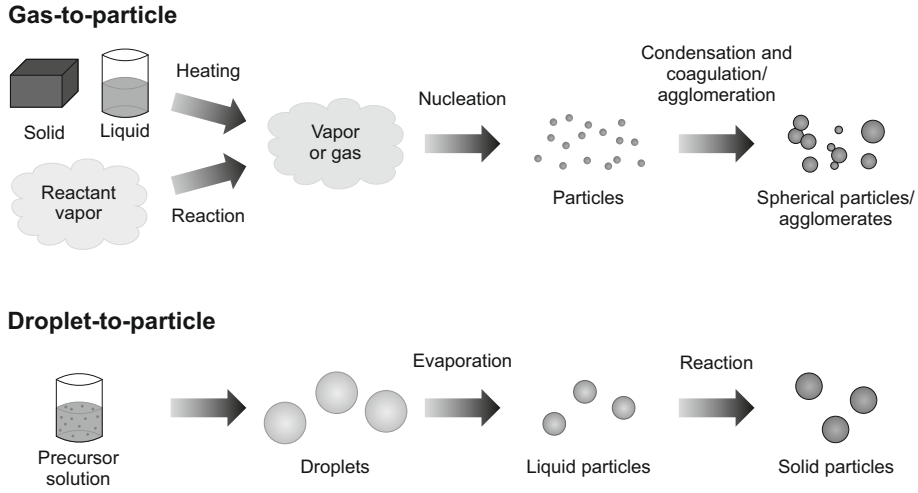

Figure 2.1: A schematic of the basic physical and chemical processes involved in the particle formation and growth by the gas-to-particle and the droplet-to-particle conversion.

In the droplet-to-particle route (or the spray process), a liquid precursor solution is atomized into a gas flow. First, the solvent evaporates from the sprayed droplets, after which solid particles are formed from the liquid precursor through chemical reactions, such as thermal decomposition or hydrolysis. The generated particles are usually spherical, as they are formed directly from the liquid droplets. Furthermore, the particle size can be controlled with the concentration of the solution. The difficulty of finding suitable precursors is a major drawback of the droplet-to-particle route.

High temperatures are usually required in order to provide the necessary energy for the physical and chemical aerosol processes, such as, evaporation of materials and thermal decomposition of precursors, respectively. Energy sources utilized in the nanoparticle production include, for example, flames (Pratsinis, 1998), furnaces (Scheibel and Porstendörfer, 1983), sparks (Schwyn et al., 1988), and lasers (El-Shall et al., 1994). Although, in this thesis, flames are used to produce powders of nanoparticles (**Paper II** and **III**), mainly tubular flow furnaces are utilized in the nanoparticle production. Compared to many other energy sources, in furnaces, the whole gas flow is heated, making the process rather energy inefficient. On the other hand, more controllable temperatures and temperature gradients are achieved.

The gas-to-particle conversion was utilized in the nanoparticle generation in **Paper I**, where bulk silver was heated at temperatures above its melting point (961.78 °C, Haynes, 2016), and the particles were formed by a physical evaporation–condensation (EC) process. A different type of a gas-to-particle route, chemical vapor synthesis (CVS) (Heel and Kasper, 2005), was exploited in **Paper IV**, where the thermal decomposition of tetraethyl orthosilicate (TEOS) vapor led to the nanoparticle formation. The droplet-to-particle conversion was utilized in **Paper II** by thermally decomposing liquid titanium isopropoxide (TTIP) particles in a spray pyrolysis process. The thermal decomposition of TEOS and TTIP leads to silica and titania nanoparticles, respectively, according to the following reactions (Okuyama et al., 1986):

$$\mathrm{Si(OC_2H_5)_4} \rightarrow \mathrm{SiO_2} + 4\mathrm{C_2H_4} + 2\mathrm{H_2O} \tag{2.1}$$

$$\mathrm{Ti(OC_3H_7)_4} \rightarrow \mathrm{TiO_2} + 4\mathrm{C_3H_6} + 2\mathrm{H_2O}, \tag{2.2}$$

where the by-products are water vapor, as well as, gaseous ethane and propene, respectively. Furthermore, the formed water can result in the simultaneous hydrolysis of the precursors. The thermal decomposition of TTIP has been reported to occur already at temperatures above 100 °C (Moravec et al., 2001), whereas, the decomposition of TEOS requires higher temperatures; over 700 °C according to Okuyama et al. (1986).

2.2 Particle size, shape, and morphology

Particle size-selection

Many of the properties of nanoparticles are determined by their size. Although, the process parameters, such as temperatures, flow rates, and concentrations, allow to tailor the particle size to some extent, the size distributions of aerosol nanoparticles are often quite polydisperse. In some applications, such as coatings and catalysts, this is usually not a major issue. However, for example, electronic and optical applications often require rather strict monodispersity from the nanoparticles.

A standard aerosol instrument, a differential mobility analyzer (DMA) (Knutson and Whitby, 1975), can be used to select a narrow particle size distribution from the aerosol. In brief, an applied voltage between two coaxial cylinders generates an electric field which will change the path of charged aerosol particles, allowing particles with a certain mobility to exit the instrument through a gap in the center cylinder. As for the particle mobility, it depends on the particle charge, which often can be assumed to be one elementary charge, and the mobility diameter. This equivalent diameter corresponds to the geometrical diameter for spherical particles, whereas, for agglomerates the mobility diameter is larger than the volume equivalent diameter. As only a small portion of the nanoparticles

passes the DMA, a great amount of nanomaterial is lost in the size-selection process. On the other hand, a very narrow particle size distribution, with a geometric standard deviation (GSD) less than 1.1, can be achieved. The particle size-selection by the DMA was utilized in **Paper I** and **III**.

Spherical particles by sintering

As an individual aerosol particle collides with another particle in the gas phase, they stick to form agglomerates. This coagulation process depends on the particle size, concentration, temperature, and residence time (Hinds, 1999). The formed agglomerates are fractal-like structures consisting of several spherical primary particles. Such structures are optimal building blocks, for example, for fillers and gas sensors. However, as many applications require spherical particles, the ability to tailor the particle morphology is extremely vital. Consequently, spherical aerosol nanoparticles can be obtained by sintering the formed agglomerates in a heated gas flow.

During the sintering, necks starts to develop between the adjacent primary particles of the agglomerate. By increasing the residence time or temperature, the diameter of the primary particles increases by fusioning with each other. Meanwhile, the mobility diameter of the agglomerate decreases, eventually becoming identical to the primary particle diameter for a fully sintered sphere (Eggersdorfer and Pratsinis, 2014). Different sintering mechanisms can be broadly dived into surface transport (e.g. evaporation/condensation, surface diffusion) and bulk transport processes (e.g. grain boundary diffusion, viscous/plastic flow) (Karlsson et al., 2005). The actual dominant sintering mechanisms depend on the particle material and process conditions. Furthermore, particle sintering at elevated temperatures can lead to higher degree of crystallinity (Magnusson et al., 1999), as well as, phase transformations (Ahonen et al., 2001). In this thesis, sintering was used to obtain spherical silver nanoparticles (**Paper I**), as well as, silica and titania nanoparticles (**Paper III** and **IV**).

Morphology of multicomponent particles

Besides the particle size and shape, the morphology of multicomponent nanoparticles strongly affects their properties. For example, the catalytic material needs to be on the surface of a particle, whereas, potentially harmful materials can be coated with a protective layer. Several aerosol methods can be used to produce multicomponent nanoparticles, either by mixing different materials before the particle generation or by adding new materials further in the production process. Generally, the morphology of the produced particles can be tuned to some extent by the process parameters, such as, relative amounts of the materials, temperatures, and residence times. However, the material properties, such as, saturation vapor pressures, surface energies, and chemical properties, determine the morphology of the end product.

In Figure 2.2, examples of different morphologies for spherical multicomponent particles are presented. Here, the morphologies are roughly divided into two categories, internally and externally structured. The internal structure can be, for example, a metal alloy (Zihlmann et al., 2014) or a Janus-like particle (Sotiriou et al., 2011a), containing segregated parts of different materials. More relevant to this thesis are the externally structured multicomponent nanoparticles: core–shell/encapsulated (**Paper II**), decorated (**Paper III** and **IV**), and composite doublet (**Paper III**).

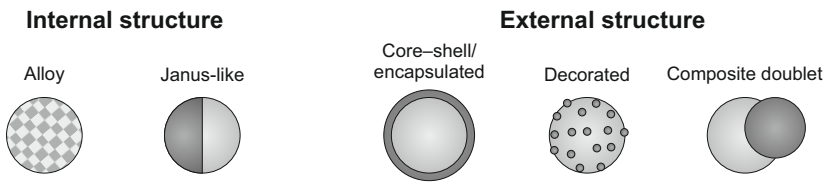

Figure 2.2: Examples of different types of morphologies for spherical composite particles divided into two categories.

Ceramic nanoparticles, such as silica, titania, and alumina, coated with noble metals (palladium, silver, platinum, and gold) can be utilized as gas sensors (Mädler et al., 2006), catalysts (Keskinen et al., 2006), antibacterials (Sotiriou et al., 2011b), and in optical applications (**Paper IV**; Boies et al., 2011). Aerosol techniques, both chemical and physical routes, have been used for the coating process. The chemical routes include flame synthesis (Keskinen et al., 2006) and chemical vapor deposition (Binder et al., 2007), whereas, physical routes usually rely on the coagulation of smaller metal particles and larger ceramic carrier particles (Boies et al., 2011; Pfeiffer et al., 2015; Sigmund et al., 2014a).

Due to the small amount of the coating material, as well as, the surface energies between the metal and ceramic materials (Pfeiffer et al., 2015), typically, the decorated morphology, consisting of small metal nanodots on a ceramic particle, is obtained. Especially in optical applications, a ceramic core–noble metal shell structure could be desirable (Oldenburg et al., 1998). However, to the best knowledge of the author, such morphology has not been produced by aerosol synthesis methods. On the other hand, core–shell structures with other types of materials have been successfully synthesized (Karlsson et al., 2004; Sigmund et al., 2014b; Teleki et al., 2008). In **Paper III**, silica and titania nanoparticles were coated with silver by vapor condensation, obtaining decorated and composite doublet morphologies, respectively.

2.3 Aerosol-assisted fabrication of metamaterials

Aerosol-synthesized nanoparticles can be collected on a desired substrate directly from the gas phase by different deposition methods, such as, thermophoresis, impaction, and electrostatic force. This opens up the possibility to incorporate or utilize aerosol particles in various types of nanostructured metamaterials with unusual properties not found in nature, such as, electrical, optical, magnetic, and catalytic (Kruis et al., 1998; Magnusson et al., 2014). The deposition of nanoparticles from the gas phase typically leads to quasilayers of randomly positioned particles. As the deposition time is increased, highly porous structures of nanoparticle layers begin to emerge.

In flame synthesis, the temperature difference between the hot flame and the cold substrate allows direct particle deposition, mainly due to the thermophoretic forces. The agglomerated particles generated in the flame can be used as different types of functional coatings with properties, such as, photoactivity and hydrophobicity (Aromaa et al., 2012; Keskinen et al., 2006). In addition, the porous nanostructures of deposited particles have been utilized as gas and biosensors (Mädler et al., 2006; Sotiriou et al., 2010). Furthermore, gas sensors composed of macroscopic conical structures of size-selected flame-synthesized agglomerates have been fabricated by impaction collection (Keskinen et al., 2009).

Quasilayers of electrostatically deposited aerosol nanoparticles have been used in the fabrication of semiconductor nanomaterials, such as quantum dots (Deppert et al., 1994) and nanowires (Messing et al., 2009). In **Paper I**, the optical properties of quasilayers of spherical silver nanoparticles on glass substrates were explored. Furthermore, electrostatic deposition of nanoparticles allows the patterning of surfaces with a resolution of approximately 100 nm (Kim et al., 2006), and even the assembly of three-dimensional structures (Lee et al., 2011).

In order to build bulk-type metamaterials, different nanocoating techniques, such as spin coating, atomic layer deposition, thermal evaporation, and electron beam evaporation, can be utilized. For instance, after particle deposition on a substrate, spin coating has been used to embed nanoparticles in a flexible polymer film (Blattmann et al., 2015; Sotiriou et al., 2013). Such films can have, for example, magnetic, optical, and conductive properties, depending on the material of the nanoparticle fillers. Atomic layer deposition and vacuum thermal evaporation are techniques that have been used to grow ultrathin films on deposited nanoparticles for water splitting (Valenti et al., 2015) and solar cell (Jung et al., 2014) applications, respectively. Furthermore, in **Paper IV** of this thesis, electron beam evaporation was used in the fabrication of multilayer nanostructured metamaterials with linear and nonlinear optical properties.

3 Light and nanostructures

3.1 Localized surface plasmon resonance

The absorption and scattering of light, that is, the linear optical properties of metal nanoparticles immersed in a dielectric environment are dominated by a phenomenon known as the localized surface plasmon resonance (LSPR) or particle plasmons (Kreibig and Vollmer, 1995). These particle plasmons rise from the coherent oscillations of the conduction electrons as a response to the oscillating electric field of the incident light, as schematically illustrated in Figure 3.1. The resonance wavelength (λ) depends on the size, shape, and material of the particles, as well as, on the refractive index of the dielectric environment (Kelly et al., 2003).

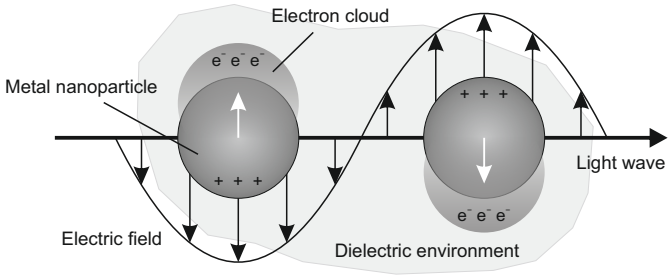

Figure 3.1: An illustration of the plasmon oscillations for spherical metal nanoparticles in a dielectric environment, showing the displacement of the electron cloud in response to the oscillating electric field of the light.

In everyday life, the LSPR of nano-sized silver and gold particles manifests as intense colors (Liz-Marzán, 2004), most commonly yellow and red, respectively. Thus, these small metal particles have been used as decorative pigments in glass coloring, already since the time of the Romans (Freestone et al., 2007; Gross et al., 1999). Besides art coloring, the plasmonic nanoparticles have found use in a variety of different applications. Most notably, as the resonance wavelength is sensitive to the changes in the dielectric environment, LSPR-based devices have been used for chemical and biological sensing (Anker et al., 2008; Willets and Van Duyne, 2007). Other interesting applications include, for example, solar cells (Atwater and Polman, 2010), data storages (O'Connor and Zayats, 2010), cancer treatment (Hirsch et al., 2003), and nonlinear optical devices (Kauranen and Zayats, 2012).

During the recent years, the LSPRs of aerosol-synthesized metal nanoparticles have been utilized in ever-increasing rate. The plasmon resonances have been characterized from the extinction spectra of nanoparticles consisting of silver (**Paper I**; Pfeiffer et al., 2014),

silver/silica (**Paper IV**; Sotiriou and Pratsinis, 2010; Sotiriou et al., 2011b), silver/titania (Gunawan et al., 2009), gold (Svensson et al., 2013; Thimsen, 2011), gold/silica (Boies et al., 2011; Sotiriou et al., 2014a), gold/titania (Chiarello et al., 2008; Mädler et al., 2003), and silver–gold/silica (Sotiriou et al., 2014b). This has given information about the presence of metal particles, the particle size, concentration, morphology, agglomeration, interparticle distance, and oxidation state. Furthermore, Sotiriou et al. have succesfully employed flame-synthesized silver/silica particles in plasmonic biosensing and bioimaging (Sotiriou et al., 2010, 2011a, 2013), as well as, gold/silica particles in photothermal cancer treatment (Sotiriou et al., 2014a). Other applications for aerosol-synthesized plasmonic nanoparticles have included, for example, solar cells (Jung et al., 2014; Pfeiffer et al., 2014), photoelectrochemical water splitting (Thimsen et al., 2011; Valenti et al., 2015), and surface-enhanced spectroscopy (Du et al., 2015; Saarinen et al., 2014).

3.2 Second-harmonic generation

When a material is irradiated with high-intensity light, the response of the material polarization to the electric field of the light can become nonlinear. Thus, the oscillating polarization of a material with a nonlinear optical response generates light at new frequencies differing from the frequency of the incident light. In other words, the color of the light changes as it passes through the material. A lowest-order nonlinear optical process, second-harmonic generation (SHG) or frequency doubling, was first experimentally demonstrated by Franken et al. (1961), soon after the invention of the laser. In SHG, light at the doubled frequency and half the wavelength compared to the incident light is generated. Effectively, two photons at the frequency of the incident light are destroyed and a photon at the second-harmonic frequency is generated, as depicted by a photon diagram in Figure 3.2.

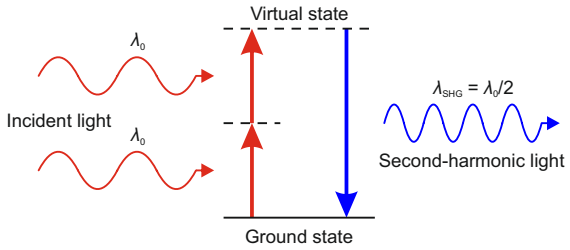

Figure 3.2: Second-harmonic generation depicted with a photon diagram. Two photons from the incident light with a wavelength of λ_0 are destroyed and a photon of the second-harmonic light at a wavelength of $\lambda_0/2$ is generated.

Only non-centrosymmetric materials, which are lacking inversion symmetry, can give rise to SHG (Boyd, 2008). Typical nonlinear materials are non-centrosymmetric crystals, such as potassium titanyl phosphate (KTP) (Zumsteg et al., 1976) and lithium triborate (LBO) (Chen et al., 1989), which are extensively used by the laser industry for the nonlinear frequency upconversion of infrared light, in order to obtain green and blue lasers (Risk et al., 2003). Furthermore, SHG techniques have been used for studying non-centrosymmetric structures found, for example, from biological materials (Campagnola and Loew, 2003) and nano-sized metal objects (Bautista et al., 2012). Also, as the inversion symmetry is necessarily broken at material interfaces, SHG techniques can be used to probe surface properties of materials (Shen, 1989).

In recent decades, enormous efforts have been made in the fabrication of various types of different metal–dielectric nanostructures for nanoscale optical devices. The research has been boosted by the rapid development of novel nano-fabrication techniques. However, due to the symmetry constraints, the observation of the second-harmonic signal from metal nanostructures has been mainly limited to surface geometries, such as rough metal surfaces (Chen et al., 1981), arrays of nanostructures fabricated by lithographic methods (Aouani et al., 2012; Grinblat et al., 2014; Klein et al., 2006; Kontio et al., 2009; Tuovinen et al., 2002), and quasilayers of nanoparticles deposited on dielectric substrates (Belardini et al., 2009; Zhang et al., 2011). Until the current research presented in this thesis (**Paper IV**), no efforts have been made to incorporate aerosol synthesis techniques in the fabrication of nonlinear optical metal–dielectric nanomaterials. In this thesis, aerosol-assisted fabrication was utilized in the fabrication of bulk-type second-order nonlinear optical materials.

3.3 Photocatalysis on titania

As incident light interacts with a semiconductor material, a photon with energy equal to or greater than the band gap (3.2 eV for anatase titania) of the material is absorbed. From this follows the excitation of an electron from the valence band of the semiconductor to the conduction band, generating a positive hole in the valence band. Through oxidation–reduction, the electron–hole pair reacts with oxygen and water molecules, generating hydroxyl radicals, which are highly oxidative. These radicals can further oxidize organic compounds forming carbon dioxide and water, for example, in air and water purification applications (Chong et al., 2010; Fujishima et al., 2000). Figure 3.3 shows a schematic presentation of the decomposition of organic material by the photocatalytic reaction on titania.

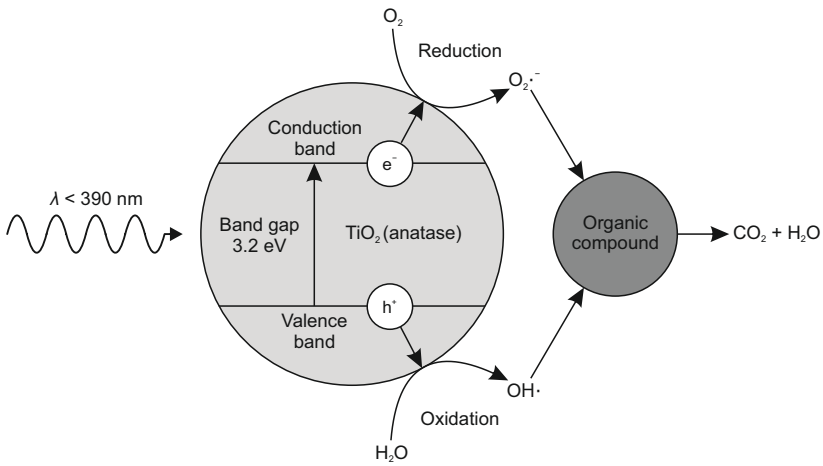

Figure 3.3: A schematic of the decomposition of organic material by the photocatalytic reaction on titania.

Due to the larger surface-to-volume ratio compared to bulk materials, nanoparticles are excellent candidates for photocatalytic applications. However, the recovery of these small particles with conventional methods, such as filtration, is not very efficient. In order to overcome this issue, magnetic recovery of the photocatalytic nanoparticles has

been introduced (Polshettiwar et al., 2011; Yao et al., 2015). Magnetically separable photocatalytic nanoparticles compose usually of photocatalytic titania and magnetic iron oxide, synthesized with wet-chemical methods (Álvarez et al., 2010; Gao et al., 2003; Watson et al., 2002). Within a few recent years, also aerosol synthesis techniques, flames (Buyukhatipoglu and Morss Clyne, 2010) and spraying processes (Costa et al., 2012; Jiang et al., 2014; Li et al., 2011), have been utilized in the production of such composite nanoparticles for magnetically separable photocatalyst nanopowders. In **Paper II** of this thesis, a novel approach to the synthesis of iron oxide–titania composite nanoparticles is taken by combining the advantages of the two aerosol techniques, the high-production rate of the flame, as well as, the controllability of the spraying process.

4 Experimental methods

This thesis consists of experimental work performed in several different research laboratories. The aerosol synthesis, measurements, and nanomaterial fabrication was conducted in the Aerosol Physics Laboratory of the Department of Physics at Tampere University of Technology (TUT). In addition, a part of the nanomaterial fabrication process, electron beam evaporation, was performed in the Optoelectronics Research Centre at TUT. The produced nanomaterials were characterized in the Department of Materials Science and Optoelectronics Research Centre at TUT, and in the Center of Microscopy and Nanotechnology at University of Oulu. Morever, the optical and photocatalytic measurements were conducted in the Optics Laboratory of the Department of Physics, and in the Department of Materials Science at TUT, respectively.

4.1 Synthesis

The nanoparticles produced in this thesis were synthesized using aerosol processes in closed flow systems at atmospheric pressures. In all publications, high-temperature tubular furnace reactors provided the thermal energy required for the physical and chemical processes, such as evaporation, chemical decomposition, and sintering. The furnaces were equipped with either quartz, at temperatures below 1000 °C, or alumina worktubes. The source materials and precursors for the synthesized nanoparticles were bulk silver (Ag) (purity 99.9 %) (**Paper I**, **III**, and **IV**); TTIP (97 %) (**Paper II**); TEOS (98 %) (**Paper IV**); and nanopowders of iron oxide (Fe_2O_3) (**Paper II**), titanium dioxide (a.k.a. titania) (TiO_2), and silicon dioxide (a.k.a. silica) (SiO_2) (**Paper III**).

A flame synthesis method called the liquid flame spray (LFS) (Tikkanen et al., 1997) was used to produce the nanopowders of iron oxide, silica, and titania, used as source materials in the subsequent synthesis processes. In brief, in the LFS, a liquid precursor is sprayed into a high-temperature hydrogen–oxygen flame. Ideally, the sprayed droplets evaporate, after which the vapor undergoes chemical reactions, leading to the gas-to-particle conversion. The formed particles grow from condensation and coagulation, usually resulting into a highly agglomerated end product (Eggersdorfer and Pratsinis, 2014). The properties of the produced nanoparticles can be tuned with the operation parameters, such as precursor concentration and feed rate, as well as, the gas flow rates and the particle collection distance from the burner. A more detailed description of the LFS can be found from the literature (Aromaa et al., 2007; Haapanen et al., 2015; Mäkelä et al., 2004).

Figure 4.1 shows a schematic illustration of the experimental setups, with the most relevant components, used in this thesis. The setups are divided into three parts: particle generation, size selection and sintering, and coating. Note that not all of these parts are

used in every experimental setup. Furthermore, the source materials and the furnace temperatures are listed in the figure. In all setups, nitrogen (N_2) was used as a carrier gas.

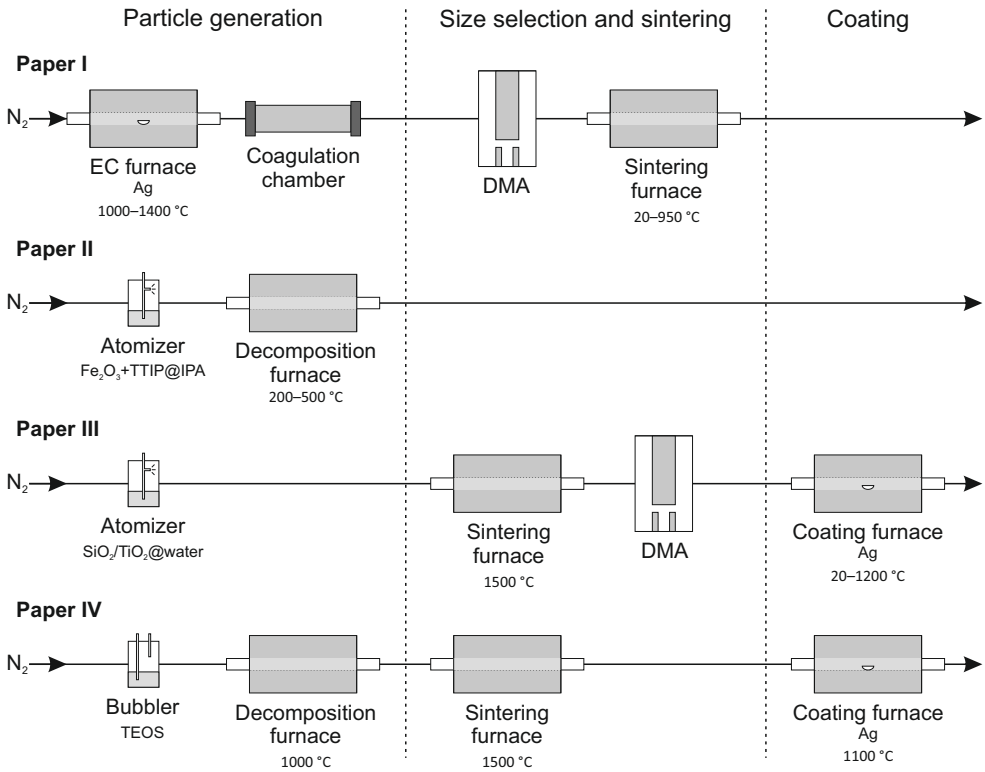

Figure 4.1: A schematic illustration showing the main components of the aerosol synthesis setups used in this thesis (**Paper I**–**IV**). The setups are divided into three parts: particle generation, size selection and sintering, and coating. The used materials and furnace temperatures are listed in the figure.

In **Paper I**, spherical and monodisperse silver particles with diameters of 50 – 130 nm were generated using an EC method (Scheibel and Porstendörfer, 1983) followed by particle size selection and sintering in the aerosol phase. First, silver was evaporated from a small piece of bulk silver situated in the center of a tubular furnace. Due to the temperature drop after the furnace, the silver vapor condenses into nanoparticles. As the goal was to produce relatively large nanoparticles, the agglomeration of the particles was enhanced by increasing the residence time with a coagulation chamber. Monodispersity of the particles was accomplished with a DMA, after which the silver agglomerates were sintered to spherical particles. Here, the DMA was placed before the sintering furnace in order to study the sintering process of the monodisperse particles.

Iron oxide agglomerates encapsulated by titania were produced in **Paper II**. A suspension containing LFS-generated iron oxide nanopowder and liquid TTIP in isopropyl alcohol (IPA) was sprayed into a tubular furnace with an atomizer aerosol generator. In the furnace, first the IPA solution evaporated from the droplets, and then the TTIP thermally decomposed to titania on the surface of the iron oxide agglomerates via the liquid-to-particle route, thus, encapsulating an iron oxide agglomerate inside a spherical

titania particle. Similar type of processes, spraying of nanoparticles suspensed in a liquid precursor, have been used to synthesize multicomponent particles. The produced particles have been, for example, zinc oxide nanoparticles embedded in a sub-micron silica sphere (Abdullah et al., 2004), and sub-micron mesoporous sphere composed of silver-decorated titania particles (Zhao et al., 2012), in contrast to the core–shell/encapsulated nanoparticles obtained in this thesis.

The coating process of spherical ceramic nanoparticles of silica and titania using silver vapor condensation was studied in **Paper III**. Aqueous suspensions of either LFS-generated silica or titania nanopowder was sprayed into a sintering furnace in order to obtain spherical carrier particles. These particles were then coated with silver in a furnace system containing three separate heating zones, with the bulk silver in the first furnace. The coating process resulted in silver-decorated silica particles or titania–silver composite doublets. A DMA between the sintering and the coating furnaces was used to study the effect of the particle size and the concentration to the acheived silver coating.

In the final publication of this thesis (**Paper IV**), silver-decorated silica nanoparticles were produced using a similar coating setup than in **Paper III**. The silica particles were synthesized using a CVS method (Heel and Kasper, 2005). TEOS vapor was introduced into a tubular furnace by bubbling nitrogen through liquid TEOS. After the decomposition of the TEOS vapor to silica via the gas-to-particle route, the formed nanoparticles were sintered to spherical. Finally, the silica particles were coated with silver in a single furnace containing a bulk piece of silver.

4.2 Deposition

The LFS-generated iron oxide, silica, and titania nanoparticles were collected into a nanopowder directly after the flame with an electrostatic precipitator (ESP) consisting of two parallel metal plates separated by a distance of approximately 60 mm. High voltage was applied to the plate that contained several corona wires used to charge the aerosol particles which were then collected on the grounded plate.

Nanoparticle deposition in the closed flow systems for electron microscopy characterization and on glass substrates was accomplished with an ESP preceded by a small corona charger. The charger used in this thesis was introduced by Harra (2010) and later utilized by Arffman et al. (2014) in the electrical detection of aerosol particles with a high-resolution low-pressure cascade impactor, whereas, the used ESP was similar to the one introduced by Krinke et al. (2002). In this thesis, the 5 mm inlet of the cylinder shaped ESP widened to 100 mm inside the device, leading to a decrease in the particle velocity. Inside the ESP, a perpendicular electric field of $2.5–4.0\,\mathrm{kV\,cm^{-1}}$ was applied between the ceiling and the round collection electrode with a diameter of 20 mm. The charged aerosol particles were deposited on the desired substrates placed on top of the collection electrode. Figure 4.2 shows a schematic illustration of the particle charging and subsequent deposition with an ESP. With the knowledge of the particle size and concentration obtained from aerosol measurements, it was possible to estimate the obtained area fraction of the deposited particles on the substrate.

Illustrations of the two different types of metamaterial nanostructures studied in this thesis, (a) a surface sample, and (b) a bulk-type sample, are shown in Figure 4.3, along with electron microscopy images. The studied surface sample was a quasilayer of spherical and monodisperse silver nanoparticles (**Paper I**), and the bulk-type sample was a multilayer structure with alternating layers of silver-decorated silica nanoparticles and pure silica

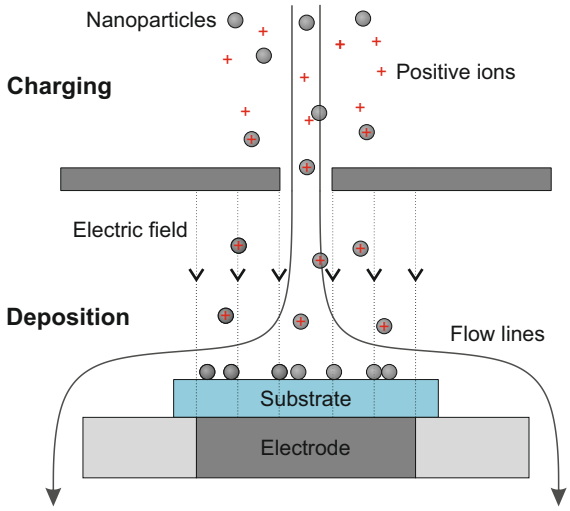

Figure 4.2: A schematic illustration of the particle charging and subsequent deposition on a substrate with an electrostatic precipitator (ESP).

(**Paper IV**). In the latter structure, the porous nanoparticle layers were covered with silica layers with an electron-beam dielectric coater. Due to the porosity, it was suggested that the silica partially penetrates the particle layer, as also illustrated in Figure 4.3b.

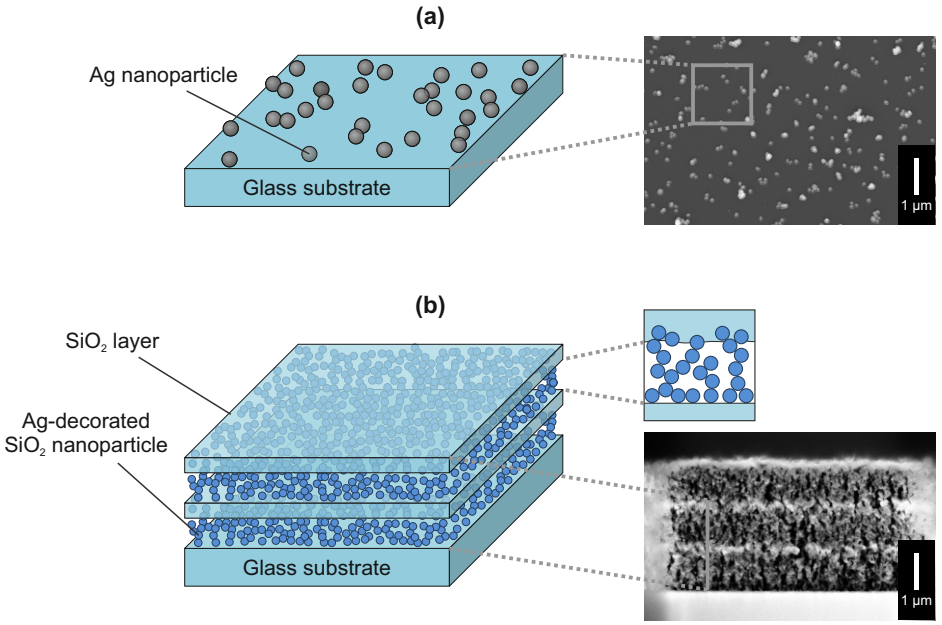

Figure 4.3: Illustrations and electron microscopy images of the two different types of metal–dielectric metamaterial nanostructures studied in this thesis: (a) a surface sample with a quasilayer of silver nanoparticles (**Paper I**), and (b) a bulk-type multilayer sample with porous layers of silver-decorated silica nanoparticles separated by layers of pure silica (**Paper IV**). The inset shows the proposed structure of the layers.

4.3 Characterization

Several characterization techniques were used to study the properties of the produced nanomaterials, both during the nanoparticle synthesis process and after the particle deposition. Table 4.1 lists the instruments and methods used in the publications of this thesis. The aerosol measurements refer to the instruments used to detect the aerosol particles during the synthesis process, whereas, the deposited particles were studied with electron microscopy imaging, and elemental and phase analysis. Other studied properties of the produced nanomaterials included optical, both linear and nonlinear, and photocatalytic properties.

Table 4.1: A list of the instruments and methods used for the characterization of the produced nanomaterials.

Paper	Particle materials	Aerosol measurements	Electron microscopy	Elemental and phase analysis	Other studied properties
I	Ag	SMPS CPC	TEM SEM	—	Linear optical
II	Fe_2O_3 TiO_2	SMPS	TEM	EDS XRD Raman	Photocatalytic (Magnetic)
III	SiO_2 TiO_2 Ag	SMPS CPC ELPI+	TEM	EDS SAED	—
IV	SiO_2 Ag	SMPS	TEM FIB	—	Linear optical Nonlinear optical

Aerosol measurements

Aerosol instruments were used to measure the particle number size distributions and monitor the nanoparticle production in the gas phase in all of the publications. Mainly, a scanning mobility particle sizer (SMPS) (Wang and Flagan, 1990) composed of a radioactive neutralizer (Krypton-85), a DMA, and a condensation particle counter (CPC) measured the size distribution of the generated particles at different stages of the synthesis processes. The number concentration of the nanoparticles in the gas phase was measured using a CPC with a cut point of 3 nm in **Paper I** and **III**. In addition, the total current measured by an electrical low pressure impactor (ELPI) (Järvinen et al., 2014; Keskinen et al., 1992) was utilized in **Paper III**, as the total current is directly proportional to the total condensation sink (CS) of the aerosol particles (Järvinen et al., 2015; Kuuluvainen et al., 2010). Moreover, the CS is the attachment rate of the condensing atoms and molecules onto the aerosol particles.

Electron microscopy imaging

Electron microscopy imaging is the most reliable method used in this thesis in order to obtain information about the nanoparticle morphology and the structure of the nanomaterials. A transmission electron microscope (TEM) was used to image individual particles deposited on carbon coated metal grids in all of the publications. Furthermore, an image processing and analysis software ImageJ (Schneider et al., 2012) was used to calculate the particle number size distributions from the obtained TEM micrographs

in **Paper I**. Moreover, a scanning electron microscope (SEM) was used to image the glass substrates containing the deposited nanoparticles shown in Figure 4.3a. The cross section of the multilayer nanostucture in **Paper IV** was fabricated using the focused ion beam (FIB) technique and imaged with a TEM (Figure 4.3b).

Elemental and phase analysis

The elemental composition of the nanoparticles produced in **Paper II** and **III** were studied with an analytical TEM equipped with an energy-dispersive X-ray spectroscopy (EDS) instrument. The measured EDS spectra were analyzed both qualitatively and quantitatively. For the latter, a commercial software was used to calculate the mass percents of the different elements.

The phase of the produced nanoparticles was analyzed in detail in **Paper II** and **III**. In **Paper II**, X-ray diffraction (XRD) was used to determine the phase of the both materials, titania and iron oxide, in the composite particles. As magnetite and maghemite phases of iron oxide have nearly identical XRD patterns (see e.g. Pinna et al., 2005), Raman spectroscopy was successfully used to distinguish the crystal structure of the produced nanoparticles. The crystallinity of the ceramic particles generated in **Paper III** was studied using the selected area electron diffraction (SAED) mode of the TEM.

Linear and nonlinear optical properties

Both linear and nonlinear optical properties of the nanoparticles deposited on glass substrates were studied in this thesis. Simplified schematic illustrations of the experimental setups are presented in Figure 4.4. The linear optical properties of the samples fabricated in **Paper I** and **IV** were studied by measuring their extinction spectra with ultraviolet–visible spectroscopy (UV–Vis) at wavelengths of approximately 300–1000 nm (Figure 4.4a). A clean glass substrate was used as a reference, and thus, only the contribution of the nanomaterial to the optical extinction was included in further analyses.

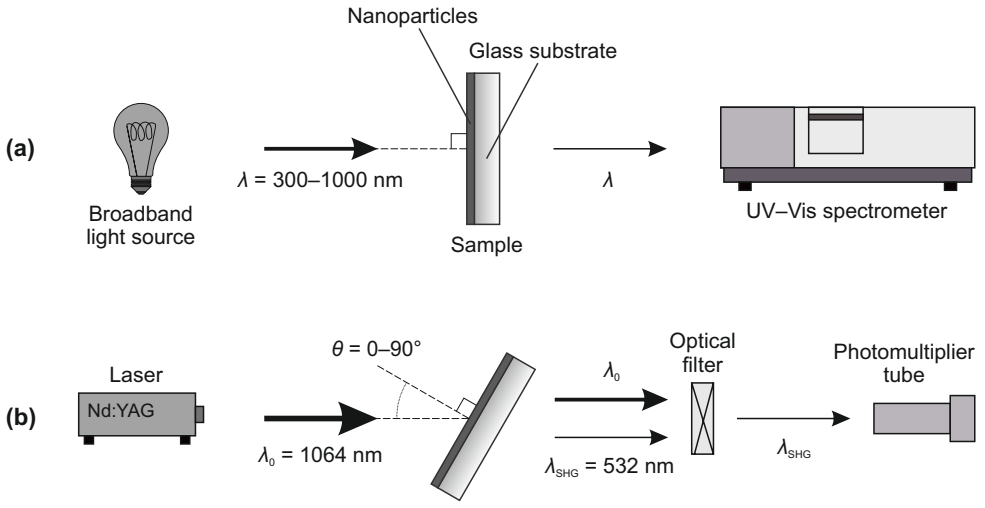

Figure 4.4: A schematic illustration of the experimental setup used to measure (a) the linear (**Paper I** and **IV**) and (b) the nonlinear optical properties (**Paper IV**) of the fabricated samples.

Besides optical extinction, also the second-harmonic generation of the fabricated multilayer nanomaterials was determined in **Paper IV**. This nonlinear optical response was measured as a function of the angle of incidence (θ) in a Maker-fringe setup (Maker et al., 1962) (Figure 4.4b). A fundamental beam of laser light with a wavelength of 1064 nm was focused on the sample plain resulting in the generation of the second-harmonic signal at a wavelength of 532 nm. The fundamental beam was filtered out after the sample, and the SHG signal was detected by a photomultiplier tube. A more detailed description of the measurement setups used to determine the optical properties of the fabricated metamaterials are presented in the doctoral dissertation of Mariusz Zdanowicz (2014).

Photocatalytic properties

In **Paper II**, the photocatalytic properties of the encapsulated iron oxide–titania nanopowder were measured by the discoloration of methylene blue (MB) under a UV lamp. The concentration of the MB in an aqueous solution was monitored at one hour intervals by first separating the powder particles from a small amount of the solution, and then measuring the absorbance of the MB at a wavelength of 665 nm with an experimental setup similar to the one presented in Figure 4.4a. These measurements were meant to demonstrate the photocatalytic activity of the produced nanopowder. As no reference nanopowders were used, the results must be treated qualitatively.

5 Results and discussion

5.1 Tailoring the particle morphology

Figure 5.1 shows a compilation of the different particle sizes, materials, and morphologies synthesized in this thesis. Illustrations of the particles are placed on a graph were the horizontal axis indicates the geometric mean diameter (GMD), and the vertical axis shows the geometric standard deviation (GSD), both measured in the aerosol phase with an SMPS. The measured GMDs are between approximately 50 and 150 nm, and the GSDs range from less than 1.1 to approximately 1.9. The narrow distributions with the lowest GSDs (shaded area in Figure 5.1) were accomplished with the particle size-selection through a DMA (**Paper I** and **III**), while the broader distributions obtained in **Paper II** are a result of the used air-blast atomizer (Chen et al., 2011).

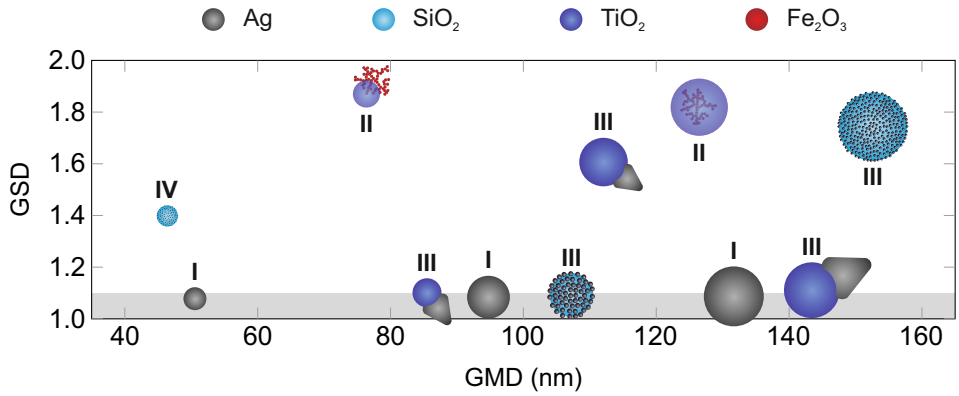

Figure 5.1: The range of particle sizes, materials, and morphologies synthesized in this thesis (**Paper I**–**IV**). The geometric mean diameter (GMD) and the geometric standard deviation (GSD) of the particles is presented on the horizontal and vertical axis, respectively. The shaded area (GSD < 1.1) corresponds to the nanoparticles size-selected with a differential mobility analyzer (DMA).

As seen from Figure 5.1, the synthesized nanoparticles compose of four materials, metallic silver, as well as, oxides of silicon, titanium, and iron. In the end products, silica had an amorphous structure and iron oxide was crystalline maghemite. With titania, both crystalline anatase and rutile were produced. Furthermore, the different particle morphologies synthesized in this thesis include both single and two-component nanoparticles: spherical (**Paper I**), encapsulated (**Paper II**), decorated (**Paper III**–**IV**), and composite doublet (**Paper III**). These morphologies were accomplished mainly using aerosol techniques of particle sintering (**Paper I**), coating (**Paper III**–**IV**), and encapsulation (**Paper II**).

Sintering of silver nanoparticles

Spherical silver particles in the size range of approximately from 1 nm (Alanen et al., 2015; Kangasluoma et al., 2013) to 200 nm (Arffman et al., 2015) have been produced with aerosol synthesis techniques in the recent years, mostly for test aerosols. In **Paper I**, fairly large spherical silver particles ($d_{\mathrm{sphere}} \approx 50-130$ nm) were produced by sintering DMA size-selected silver agglomerates ($d_{\mathrm{aggl.}} \approx 70-200$ nm) in a heated flow. The sintering process was investigated by measuring the mobility diameter of the particles as a function of the sintering temperature with an SMPS.

Figure 5.2 shows the mobility diameter for three different size-selections as a function of the sintering temperature, along with schematic illustrations of a silver particle at different stages of the sintering process. Three processes typical to the particle sintering can be distinguished from the figure: the compaction, the internal restructuring, and the evaporation. Starting from the room temperature, at first the mobility diameter of the agglomerates decreased fairly linearly due to the compaction, until a certain temperature, the compacting temperature (T_{c}), introduced by Karlsson et al. (2005), is reached. Even though, the mobility diameter stays constant after this temperature, internal restructuring shapes the particles from a spheroid-like to more spherical. According to e.g. Ashby (1974), Shimada et al. (1994), and Weber and Friedlander (1997), the dominant sintering mechanism for silver nanoparticles is grain boundary diffusion. Finally, near the bulk melting point of silver, the particle size begins to decrease again due to evaporation.

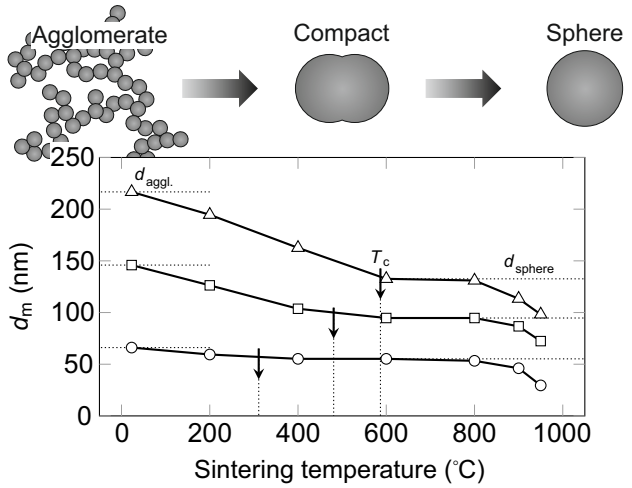

Figure 5.2: The mobility diameter of the size-selected silver nanoparticles as a function of the sintering temperature. The arrows indicate the compaction temperature, after which the mobility diameter remains constant until the particles began to evaporate near the bulk melting point. The schematic illustrations show the evolution of a particle from an agglomerate (mobility diameter $d_{\mathrm{aggl.}}$) to a compact particle, and finally to a spherical particle (d_{sphere}). (Adapted from **Paper I**.)

Several studies have investigated the sintering process of monodisperse silver nanoparticles, usually in the size range of 10 – 100 nm (Deppert and Magnusson, 2001; Ku and Maynard, 2006; Schmidt-Ott, 1988; Shimada et al., 1994; Weber and Friedlander, 1997). In a recent study by Arffman et al. (2015), spherical silver nanoparticles as large as 200 nm were produced by sintering polydisperse agglomerates at a fixed temperature of 800 °C. In

Figure 5.3, the mobility diameter of the size-selected silver agglomerates, as well as, the compacting temperature as a function of the diameter of the sintered spherical particles are presented. The findings of **Paper I** of this thesis are in agreement, and also continue the trends for larger particle sizes set in the literature.

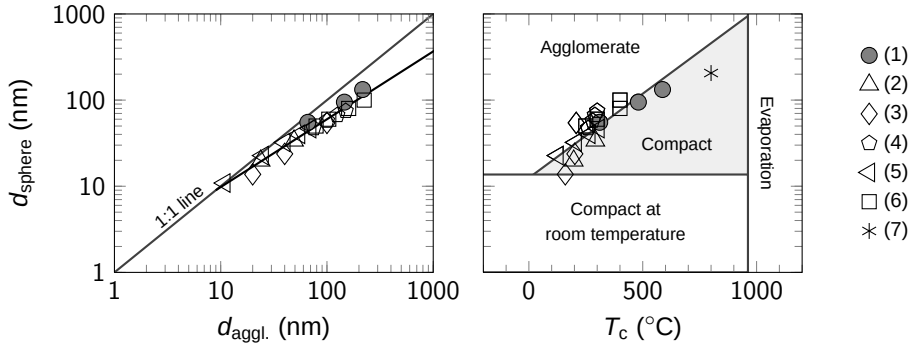

Figure 5.3: The mobility size of the size-selected silver agglomerates (left), and the compacting temperature (right) as a function of the diameter of the sintered spherical particles. The results of (1) **Paper I** are compared to the literature values by (2) Schmidt-Ott (1988), (3) Shimada et al. (1994), (4) Weber and Friedlander (1997), (5) Deppert and Magnusson (2001), (6) Ku and Maynard (2006), and (7) Arffman et al. (2015).

The two graphs in Figure 5.3 give a rough estimation of the requirements for producing specific-sized spherical silver nanoparticles by sintering agglomerates. The solid black line in the left-hand graph shows the required mobility size for the agglomerate size selection, whereas, the required sintering temperature is within the shaded area of the right-hand graph. Furthermore, the results suggest that particles with diameters smaller than approximately 10 – 20 nm are spherical already at the room temperature. This is in line with the reported sizes of the silver primary particles (∼7.5 – 22 nm) (Ku and Maynard, 2006; Schmidt-Ott, 1988; Shimada et al., 1994; Weber and Friedlander, 1997). In order to obtain fully spherical particles, the sintering temperature has to be somewhat higher than the compacting temperature, approximately 50 – 200 °C for spherical particles with diameters of 50 – 100 nm, according to Ku and Maynard (2006).

As all the referenced studies employ different experimental setups, it should be noted that different parameters, such as, the primary particle size, the sintering time, and the possible impurities will have an effect on the obtained results. For example, the theoretical sintering time, that is, the time required for the coalescence of two equally sized spheres, can change orders of magnitudes with relatively small changes in the temperature and primary particle size (see e.g. Nakaso et al., 2002; Shimada et al., 1994).

Coating of ceramic nanoparticles with silver

Ceramic carrier particles of amorphous silica and crystalline rutile titania were coated via silver evaporation and subsequent heterogeneous nucleation and vapor condensation in **Paper III**. Under investigation was the effect of the different coating parameters: the material, size, and concentration of the ceramic carrier particles; and the evaporation temperature of silver. The amount of the evaporated silver was estimated by measurements with an SMPS and calculations using the evaporation rates reported by Lu and Zhu (2007). The results along with the upper limit obtained by assuming that the gas was saturated

with silver (Alcock et al., 1984) are presented in Figure 5.4. Taking into account the losses of the evaporated silver vapor and the silver particles formed by homogeneous nucleation, it is obvious that the calculation provides higher values than the measurements.

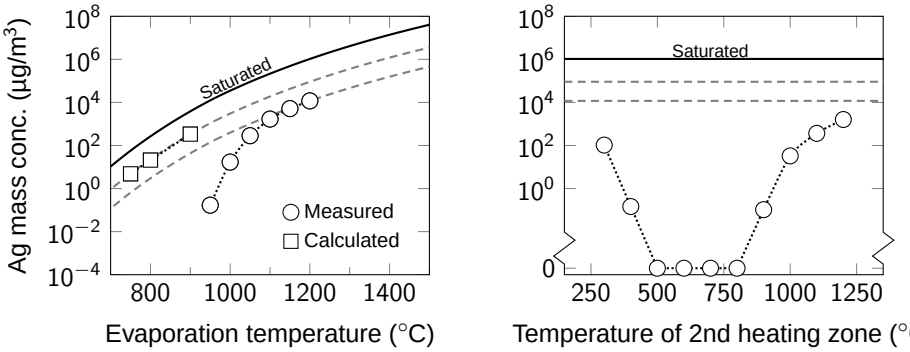

Figure 5.4: The total mass concentration of the evaporated silver as a function of the evaporation temperature measured with an SMPS and calculated using the evaporation rates determined by Lu and Zhu (2007) (left). The total mass concentration of silver particles measured with an SMPS and a CPC as a function of the temperature of the second heating zone at an evaporation temperature of 1200 °C (right). In both figures, the solid line corresponds to a full saturation concentration at the evaporation temperature, and the dashed gray lines represent fits of the functional form of the silver vapor pressure to the measured and calculated values. (Adapted from **Paper III**.)

In order to avoid the homogeneous nucleation of the evaporated silver, the temperature gradient after the evaporation of silver was optimized by adjusting the temperature of a second heating zone followed directly after the evaporation furnace. It was assumed that at the optimal temperature, no silver particles would exit the furnace system. After setting the evaporation temperature to 1200 °C, the concentration of the silver particles was measured with an SMPS and a CPC. Figure 5.4 shows that at low temperatures, the steep gradient between the evaporation furnace and the second heating zone allowed particle formation. On the other hand, at high temperatures the silver stayed in the vapor phase until particle formation after the second heating zone. However, when the temperature of the second heating zone was set to approximately 500 – 800 °C, no particles were detected, even with the CPC alone (cut point 3 nm). Thus, at these conditions, without the presence of the carrier particles, all the evaporated silver condensates onto the tube walls. The temperature of the second heating zone was set to 600 °C in the further particle coating experiments.

The effect of the silver coating on the particle mobility diameter, and the morphology of the coated particles were studied with an SMPS and a TEM, respectively. Figure 5.5 shows how the mobility diameter of the size-selected carrier particles began to increase after the evaporation temperature reached approximately the melting point of bulk silver. At the maximum evaporation temperature of 1200 °C, the mobility diameter of the silica and titania particles had increased approximately 10 and 20 nm, respectively. In addition to this discrepancy in the mobility diameters between the two materials, notable difference in the particle morphology are evident, as seen from the TEM micrographs in Figure 5.5. On the silica particles, the silver formed small nanodots or decorations. These decorated particles are probably the most common morphology obtained in the aerosol coating processes of ceramic particles with noble metals (Backman et al., 2004; Binder et al.,

2007; Boies et al., 2011; Pfeiffer et al., 2015; Sigmund et al., 2014a). However, on top of the titania particles, the silver formed a single larger structure leading to a morphology that could be described as a composite doublet.

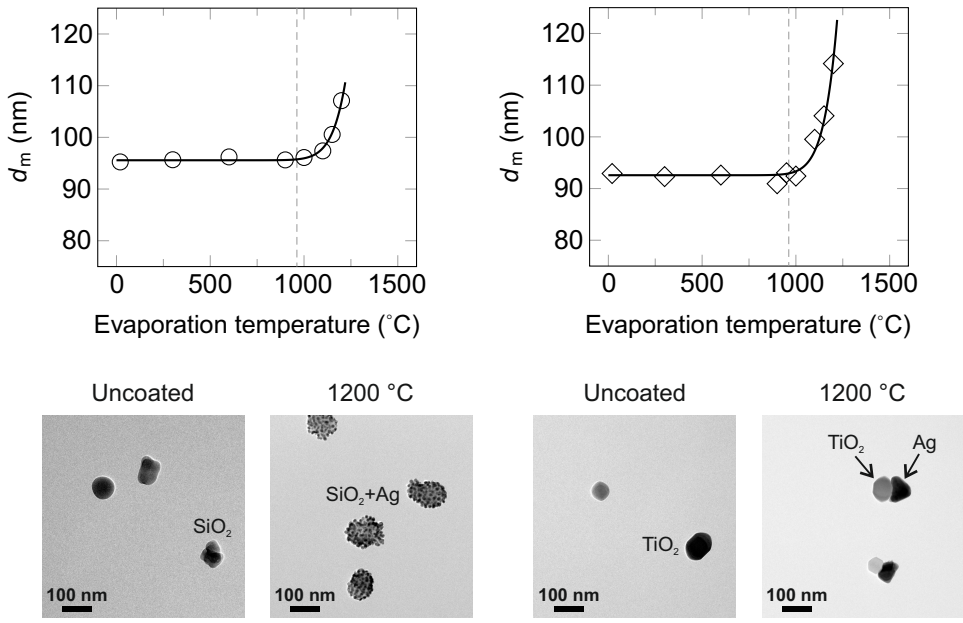

Figure 5.5: The mobility diameter of the size-selected approximately 90 nm silica (left) and titania (right) carrier particles as a function of the silver evaporation temperature. The dashed lines correspond to the melting point of bulk silver. The TEM micrographs show images of the uncoated and silver-coated silica and titania carrier nanoparticles, with decorated and composite doublet morphologies, respectively. (Adapted from **Paper III**.)

TEM micrographs, taken with a higher magnification, of approximately 90 nm silica and titania nanoparticles coated at different silver evaporation temperatures can be seen in Figure 5.6. In addition, the insets show typical SAED patterns of the particles at the corresponding temperatures. These patterns show diffusive rings and reflections corresponding to amorphous silica and crystalline rutile titania, respectively. The evaporation temperature had no effect on the phase of the carrier particles. However, at the evaporation temperature of 1200 °C, reflections from nanocrystalline silver on silica, and starting from 1000 °C, reflections from crystalline silver on titania were observed. Furthermore, the TEM micrographs show small silver nanodots on both carrier particle materials already at the evaporation temperature of 900 °C.

In the case of the silica, the size of the silver decorations increased with the temperature from approximately 1 to 10 nm. However, on the titania, the silver formed larger structures, already at 1000 °C, which can been seen to coalescence with each other at 1000 – 1100 °C. Titania particles smaller than 120 nm contained only one silver structure, whereas, several structures were observed on larger carrier particles. Furthermore, the silver structures had different shapes, including triangular, rod-like and hexagonal. Depending on the evaporation temperature and the diameter of the titania particle, the size of the silver structures could be tuned between 20 and 100 nm.

Figure 5.7 shows a schematic illustration of the proposed routes to different particle

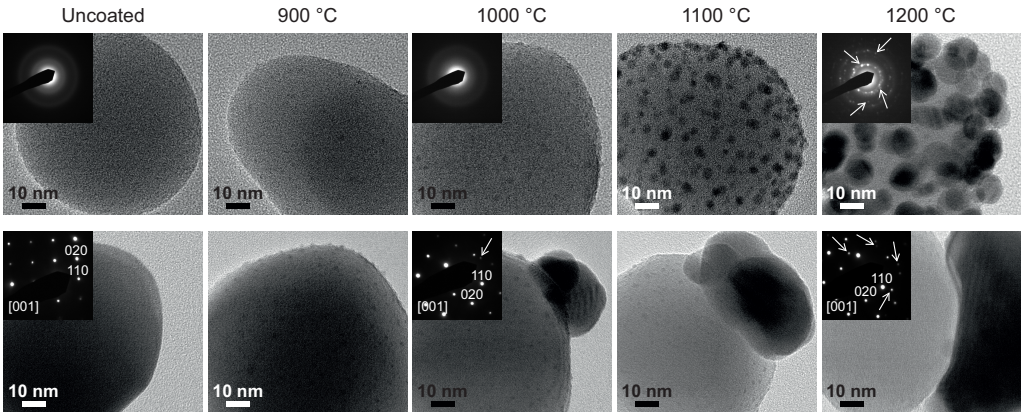

Figure 5.6: TEM micrographs of approximately 90 nm silica (top row) and titania (bottom row) nanoparticles coated with silver at different evaporation temperatures. The insets show typical SAED patterns from the particles at the corresponding temperatures. The patterns indicate amorphous silica and crystalline rutile titania particles. At the evaporation temperature of 1200 °C, reflections (marked with arrows) from nanocrystalline silver on silica, and starting at 1000 °C, reflections from crystalline silver structures on titania particles can be observed. (**Paper III**.)

morphologies. The migration of the small silver particles, and the subsequent particle collisions and coalescence on the titania carrier particles was suggested to be the cause for the composite doublet morphology. This is supported by the relatively high diffusion coefficient of silver (see e.g. Gontier-Moya et al., 2004), as well as, the formation of the different shaped silver structures, likely resulting from coalescence of two single crystals, as suggested by Harris (1995). Due to the amorphous structure of the silica, the particle surface is rougher, hindering the particle migration (Bartholomew, 2001). Furthermore, similar sintering experiments by Binder et al. (2010) with palladium-decorated silica and titania particles showed that the palladium was more stable on silica than on titania. However, in their study, the decorated morphology was maintained, most likely, due to the relatively low diffusion coefficient of palladium.

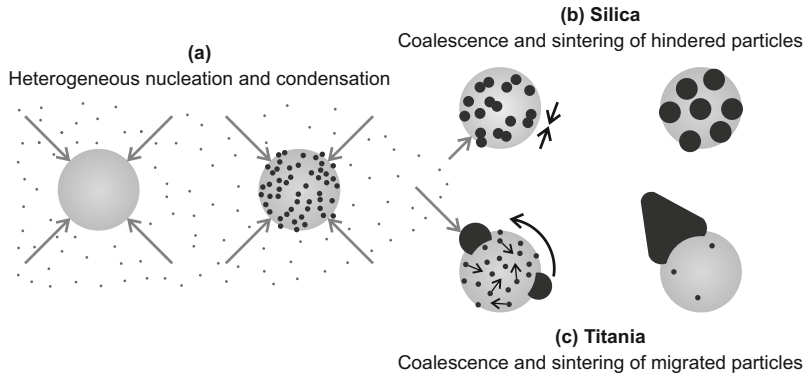

Figure 5.7: A schematic illustration of the formation of the ceramic–silver composite particles with different morphologies. (a) The initial steps are similar for both silica and titania carrier particles. Due to the differences in the Ag particle migration on (b) silica and (c) titania, decoration and composite doublets, respectively, are formed. (**Paper III**.)

Multicomponent nanoparticles by encapsulation

In **Paper II**, maghemite iron oxide agglomerates were encapsulated within spherical titania particles via a liquid-to-particle route. In the simple particle synthesis approach, iron oxide nanopowder and liquid TTIP suspensed in IPA was sprayed into a tubular furnace. After spraying, the alcohol evaporated, leaving a TTIP droplet containing a solid iron oxide agglomerate particle. As the TTIP thermally decomposed to solid titania, the formed spherical titania particle encapsulated the iron oxide agglomerate. At the furnace temperature of 500 °C, some of the TTIP evaporated before decomposition, forming small titania agglomerates through the gas-to-particle route, as also previously observed by Ahonen et al. (1999).

The ratio of iron oxide to titania, as well as, the particle size and morphology was tailored by the composition of the sprayed suspension. Figure 5.8 shows SMPS measurements of the particle number size distributions of pure iron oxide particles, as well as, encapsulated particles generated with two different precursor compositions. The weight percent of the solid iron oxide nanopowder was the same in both precursors; however, the weight percent of TTIP in the precursor 1 was an order of magnitude lower than in the precursor 2. The GMD of the particle size distribution remained unchanged at approximately 80 nm in the encapsulation process when using the precursor 1, suggesting that the titania only fills some of the voids in the iron oxide agglomerate, thus, resulting to a partially encapsulated particle. Due to the higher amount of the TTIP in the precursor 2, the GMD increased to approximately 130 nm, resulting to a fully encapsulated particle.

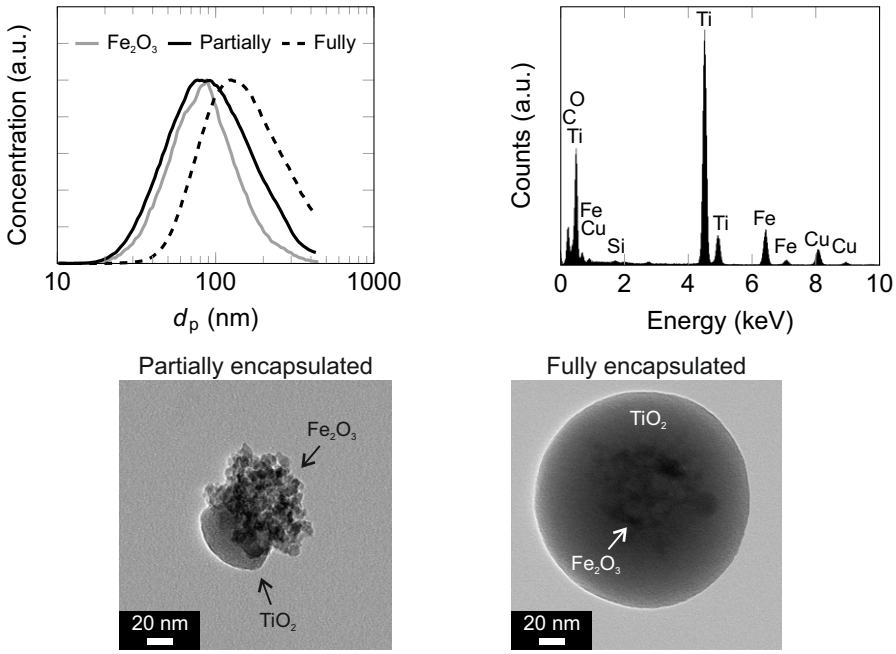

Figure 5.8: Particle number size distribution (top left) of pure iron oxide agglomerates and encapsulated particles produced with two different precursor compositions resulting to partially and fully encapsulated particles. The decomposition temperature in the encapsulation was 300 °C. TEM micrograph of a partially and a fully encapsulated iron oxide–titania particle (below). A typical EDS spectrum from a fully encapsulated particle (top right). The peaks of C, Cu, and Si were caused by the TEM grid and the equipment. (Adapted from **Paper II**.)

The conclusions made from the aerosol measurements were supported by the TEM micrographs shown in Figure 5.8. Furthermore, an EDS spectrum verified the presence of iron oxide in the fully encapsulated particles. EDS measurements were conducted for several individual fully encapsulated particles in order to find out the uniformity of the produced particles. The composition of the particles corresponded to the composition of the sprayed suspension, and no dependency on the particle size was detected. The elemental analysis also showed that some of the smallest particles contained no iron oxide. The number of these particles was estimated to be approximately 10 % of all the particles. In the particle mass, this constituted less then one percent.

5.2 Applications

Plasmonic silver nanoparticles

The LSPR of spherical silver particles with diameters of 50 – 130 nm (**Paper I**), as well as, approximately 50 nm silica particles decorated with 1 – 2 nm silver dots (**Paper IV**) were investigated in this thesis. Figure 5.9 shows a comparison of the extinction spectra of 90 nm silver particles and silver-decorated silica particles deposited on glass substrates with different area fractions and number of particle layers, respectively, along with TEM micrographs of the synthesized particles. The optical extinction is the negative logarithm of the transmittance ($-\log_{10} T$), and it includes both the absorption and the scattering of light.

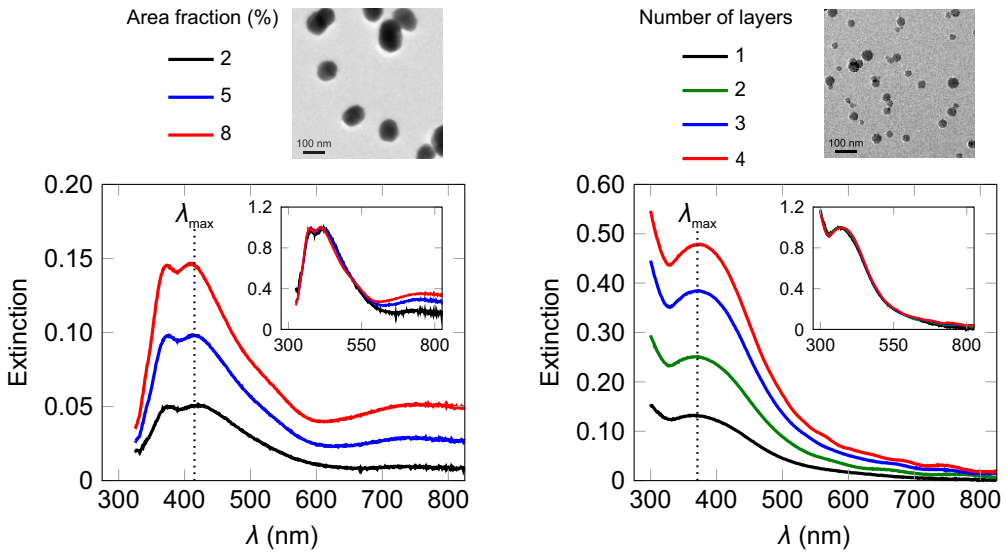

Figure 5.9: The optical extinction spectrum of 90 nm spherical silver particles on glass substrate with different area fractions (left) and silver-decorated silica particles with different number of 1 µm thick particle layers separated by silica layers (right). The nanoparticles are shown in the TEM micrographs. The insets show the spectra normalized to the maximum extinction of the LSPR. The wavelength of the LSPR is indicated by the dotted lines. (Adapted from **Paper I** and **IV**.)

A quasilayer of silver particles were deposited on a glass substrate with area fractions of approximately 2 – 8 %. The extinction spectra shows multiple peaks, two of which are

near 400 nm, and a broader peak at a longer wavelength. The theoretical calculations suggested that the two former peaks are caused by the dipolar and the quadrupolar resonances. The spectral broadening at the longer wavelength is likely caused by the particle–particle contacts on the substrate, as a consequence of the random deposition. This is supported by the normalized extinction spectra showing increasing extinction at the longer wavelength with increasing area fraction.

The silver-decorated silica particles were deposited in layers with thicknesses of approximately one micro meter separated by pure silica layers with thicknesses of approximately 200 nm. It was possible to fabricate such thick structures while maintaining the narrow plasmon resonance due to the silica in the particles. Clearly, this dielectric material prevented some of the contacts between the individual metal particles. Moreover, as the size of the silver dots in the decorated particles was considerably smaller than that of the spherical silver particles, the wavelength of the plasmon resonance was at smaller wavelengths. The increase in the extinction for decreasing wavelengths is due to the silica absorption.

A few recent studies have measured the extinction spectra of aerosol synthesized silver and silica–silver nanoparticles in various dielectric environments, such as deposited on glass substrates, as powders, in aqueous suspensions, or spin coated inside a polymer (PMMA). The different aerosol synthesis methods include mainly flames (Sotiriou and Pratsinis, 2010; Sotiriou et al., 2010, 2011b, 2013), but also sparks and furnaces (Du et al., 2015; Pfeiffer et al., 2014). Results from the literature along with the findings of this thesis are shown in Figure 5.10 where the wavelength of the LSPR is presented as a function of the size of the silver particles. Theoretical and measured reference values of silver particles embedded in environments with different refractive indices are also shown. A simple interpretation would be that $n = 1.0$ corresponds to air, 1.3 corresponds to water, and 1.5 corresponds to glass.

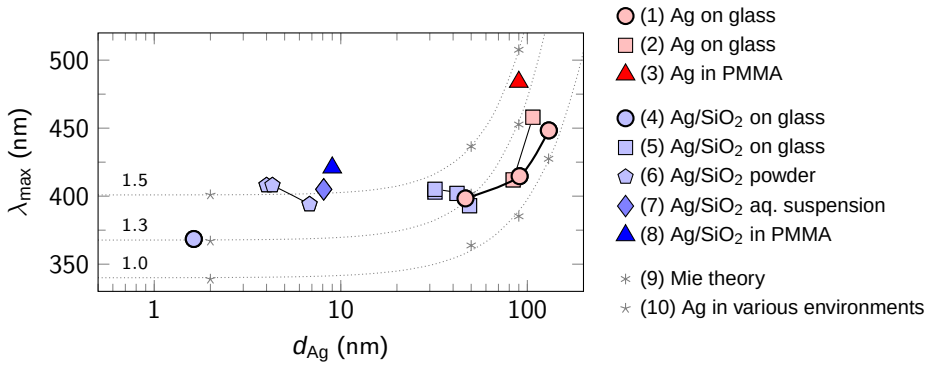

Figure 5.10: The wavelength of the localized surface plasmon resonance (LSPR) as a function of the diameter of spherical Ag nanoparticles. The results obtained in this thesis are compared to other studies involving aerosol-synthesized Ag nanoparticles: (1) **Paper I**, (2) Pfeiffer et al. (2014), and (3) Du et al. (2015); and Ag/SiO_2 composite nanoparticles: (4) **Paper IV**, (5) Sotiriou et al. (2010), (6) Sotiriou and Pratsinis (2010), (7) Sotiriou et al. (2011b), and (8) Sotiriou et al. (2013). The reference LSPR wavelengths of Ag nanoparticles in different environments ($n = 1.0–1.5$) are (9) calculated from Mie theory (see **Paper I**), and (10) reported by Kreibig (2008). The dotted lines are guides for an eye.

If the effect of the silica absorption is subtracted from the extinction spectrum of the

silver-decorated silica particles synthesized in **Paper IV**, the wavelength of the plasmon resonance is at approximately 400 nm, which is consistent with the literature values measured from flame-generated silver–silica nanoparticles. The results imply that the dielectric environment consist mainly on the silica, which has a refractive index near 1.5 (Haynes, 2016).

Both theoretical and measured values in Figure 5.10 show that the plasmon resonance wavelength for silver begins to red-shift after the particle size reaches approximately 50 nm. In **Paper I**, the wavelength was tuned in the range of approximately 400–450 nm. As the dielectric environment in the case of the deposited silver nanoparticles consist of two components, air and the glass substrate, the measured plasmon resonance wavelengths are naturally between the theoretical values predicted for the individual dielectric environments. The results for the spherical silver nanoparticles suggest that for smaller particles, the contribution of the glass substrate is higher. All in all, the plasmon resonance wavelength can be tuned by the particle size or the dielectric environment. The latter can be changed, for example, by spin-coating the deposited particles in a polymer matrix (Du et al., 2015).

Second-harmonic generation from multilayer nanostructures

The SHG of the multilayer silver-decorated silica particles was measured in **Paper IV**. In Figure 5.11, the SHG as a function of the angle of the incidence laser light is presented for samples containing 1–4 particle layers, as well as, for a plain glass substrate. The measurements show typical fringes caused by the sample geometry with a maximum SHG intensity at approximately 60°. Moreover, the SHG intensity increases with the number of particle layers. Figure 5.11 also presents the SHG intensity averaged over all angles of incidence as a function of the number of layers, showing that the SHG signal from the 4-layer sample was approximately 40 times stronger than the one measured from the plain glass substrate. Furthermore, the quadratic growth of a simplified thin film model fitted to the measurements agreed well with the obtained results. A more rigorous model for the second-harmonic response of the fabricated nanostructures was developed by Zdanowicz et al. (2014), who determined the components of the second-order susceptibility tensor.

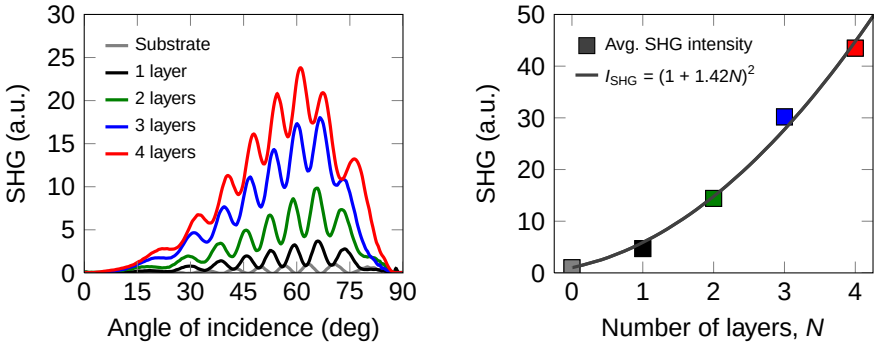

Figure 5.11: The intensity of the second-harmonic generation (SHG) as a function of the angle of the incidence laser light for the pure glass substrate and the samples with 1–4 layers (left). The averaged SHG intensity over all angles of incidence as a function of the number of layers (right). A model assuming that each layer is a thin film source of an SHG signal was fitted to the measurements. (Adapted from **Paper IV**.)

In order to study the origin of the SHG signal, two different types of control samples were prepared: a thicker 1-layer sample containing equal amount of material with the 4-layer sample (labeled CS1), and a 4-layer sample without the silver decorations (CS2). Illustrations of the samples are presented in Figure 5.12. The aim of the control samples was to study the effect of the layered structure and the silver decorations. The extinction spectrum of CS1 and the 4-layer sample were similar, as expected, since they contained the same amount of silver and silica. On the other hand, as there were no silver particles in the structure of CS2, the plasmon resonance was not present, only an increase in the extinction for decreasing wavelengths due to the silica absorption. Furthermore, CS1 had similar SHG than the thinner 1-layer sample, while the SHG intensity of CS2 was even lower than the glass substrate alone.

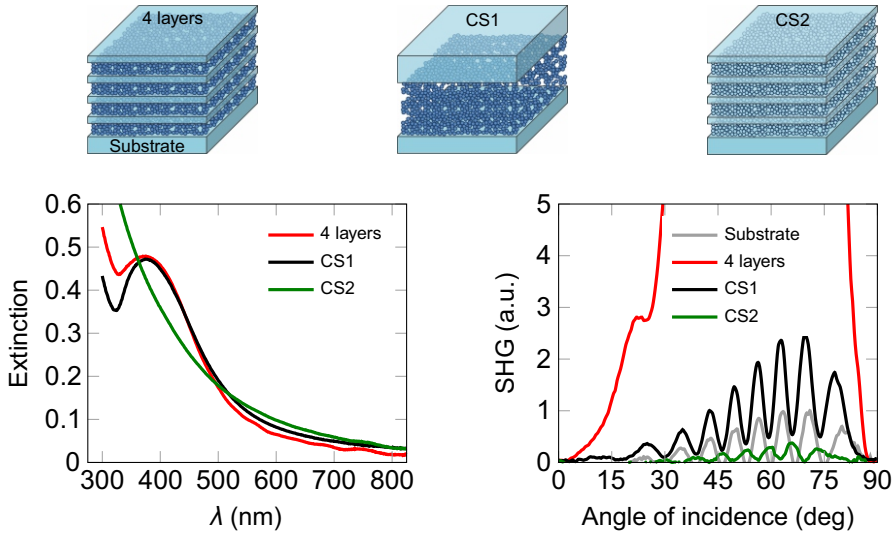

Figure 5.12: Illustrations of the different type of layered structures for studying the origin of the second-harmonic generation (SHG). The extinction spectra (left) and the SHG (right) of the samples. (Adapted from **Paper IV**.)

The optical measurements of the control samples showed that both the multilayer structure and the silver decorations play an important role in the nonlinear optical process. Furthermore, in order to produce the SHG, the sample needs to be non-centrosymmetric. Therefore, it was speculated that the silica layer fabricated by the electron-beam dielectric coater partially penetrates the top of the porous nanoparticle layer, resulting to differences between the top and the bottom particle layers, as illustrated in Figure 4.3.

The conversion efficiency of the second-order process ($\eta = I_{\mathrm{SHG}}/I_0$) for the 4-layer sample was estimated to be in the order of 10^{-12}. This value is quite modest but comparable to the efficiencies of other types of metal nanostructures reported in the literature ($\eta \approx 10^{-14}$–10^{-7}) (Aouani et al., 2012; Belardini et al., 2009; Cai et al., 2011; Feth et al., 2008; Grinblat et al., 2014; Klein et al., 2008; Lu et al., 2010; Park et al., 2012; Zhang et al., 2011; Zhou et al., 2010). The metal–dielectric metamaterials studied earlier have been surface geometries, while, the multilayer samples fabricated in this thesis, were bulk-type structures.

Based on the obtained results, the efficiency of the introduced multilayer structure could be improved by fabricating thinner particle layers, as well as, by adding more layers to

the structure. The optimization of the porosity of the particle layers and the amount of the silver could also lead to higher conversion efficiencies (Zdanowicz et al., 2014). Furthermore, enhancement in the SHG conversion is also expected when the incident laser light is operated at a wavelength closer to the LSPR (Kauranen and Zayats, 2012).

Magnetically separable photocatalyst nanopowder

As titania is known to have photocatalytic and iron oxide magnetic properties, the encapsulated iron oxide–titania nanoparticles synthesized in **Paper II** could find use as a magnetically separable photocatalyst nanopowder, for example, for water treatment applications. According to the Raman spectroscopy measurements (Figure 5.13), the iron oxide was identified as crystalline maghemite (γ-Fe_2O_3), typical phase for flame-generated iron oxide nanoparticles (Strobel and Pratsinis, 2009). Furthermore, no unwanted hematite was observed, however, due to the broad Raman bands, a minor contribution from magnetite phase cannot be completely excluded.

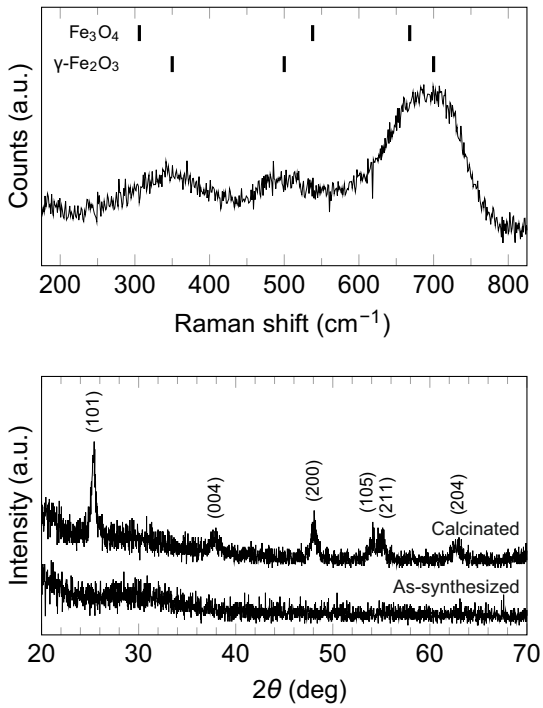

Figure 5.13: The Raman spectrum of the iron oxide nanoparticles (top), along with the positions of the peaks reported in the literature (de Faria et al., 1997; Shebanova and Lazor, 2003). The XRD pattern of the as-synthesized and calcinated fully encapsulated iron oxide–titania nanoparticles (bottom). The latter pattern shows peaks typical to crystalline anatase titania. (Adapted form **Paper II**.)

According to the XRD measurements (Figure 5.13), the titania in the as-synthesized fully encapsulated multicomponent nanoparticles was amorphous, as expected from the used temperatures (Moravec et al., 2001). However, amorphous titania is almost inactive as a photocatalyst (Ohtani et al., 1997). In order to obtain photocatalytic crystalline anatase titania, the particles were calcinated at 400 °C for one hour. The iron oxide could not be

detected from the XRD pattern of the fully encapsulated multicomponent particles, most likely due to the low concentration.

The photoactivity of both the partially and the fully encapsulated particles was measured by the decolorization of MB in an aqueous suspension. The partially encapsulated particles were found to be practically inactive as a photocatalyst, most likely due to their morphology; the titania particles were partly covered by the iron oxide agglomerates. Thus, the apparent surface area of the titania is considerably reduced by the masking iron oxide. On the other hand, the fully encapsulated particles showed photocatalytic activity as seen from Figure 5.14, where the relative absorbance of the MB is presented as a function of time. Even though, the photocatalytic mechanisms of iron oxide–titania nanocomposites have been studied earlier (see e.g. Beydoun et al., 2000), an extensive research is required to find out whether the iron oxide actually increases or decreases the photocatalytic activity of the titania in the encapsulated nanoparticles synthesized in this thesis.

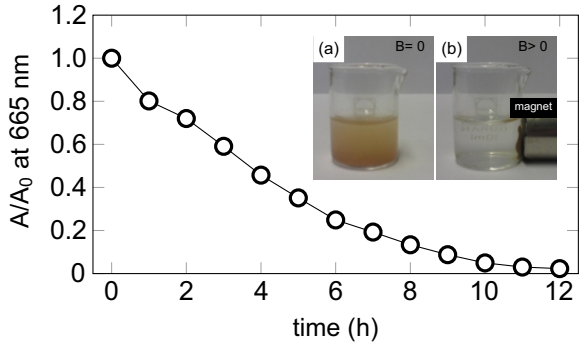

Figure 5.14: The relative absorbance of methylene blue at a wavelength of 665 nm as a function of the time with the fully encapsulated iron oxide–titanium dioxide nanoparticles as a photocatalyst. The inset shows photographs of the particles in an aqueous suspension (a) before and (b) after the application of an external magnetic field. (Adapted from **Paper II**.)

The magnetic properties of the prepared fully encapsulated iron oxide–titania composite particles were demonstrated qualitatively. Figure 5.14 shows a photograph of the nanopowder dispersed in an aqueous suspension. After the application of an external magnetic field caused by a permanent magnet, the powder particles were attracted to the wall of the glass container. The observations of the prepared nanoparticles indicate that the optimal magnetically separable photocatalyst nanopowder would be such where the iron oxide particles are fully encapsulated by the titania, and at the same time the particles should have high iron oxide/titania mass ratio.

6 Conclusions and final remarks

As the benefits of nanotechnology have become evident, novel nanoparticle synthesis methods, new types of nanostructures, and interesting applications are constantly sought after. Aerosol-based processes are highly intriguing options for the synthesis of nanoparticles and fabrication of metamaterials, as the gas phase techniques are considered tunable, inexpensive, and scalable even for industrial scale. In this thesis, aerosol-based techniques for the synthesis of single and multicomponent nanoparticles were explored. Furthermore, the size, shape, and morphology of the generated particles were tailored in the gas phase. Finally, the nanoparticles were incorporated by direct deposition from the gas phase into metamaterials, whose light–matter interactions were characterized.

The different types of nanoparticles, including spherical silver particles, titania-encapsulated iron oxide particles, silver-decorated silica particles, and silver–titania composite doublet particles, were synthesized and tailored using aerosol techniques, such as, particle size-selection, sintering, encapsulation, and coating. The particle size-selection with a differential mobility analyzer followed by a sintering step at elevated temperatures is a widely used aerosol technique for producing monodisperse spherical nanoparticles. The results obtained in this thesis were in line and continued the trends set by the previous studies found in the literature. It should be noted that monodisperse spherical aerosol nanoparticles can also be produced with other methods, such as, vapor condensation (Yli-Ojanperä et al., 2010; Zihlmann et al., 2014).

The simple particle encapsulation technique introduced in this thesis consisted of spraying a liquid precursor containing solid particles into a tubular furnace. Through a liquid-to-particle conversion, the precursor thermally decomposed, encapsulating the solid particle. This technique could be applied to the synthesis of multicomponent nanoparticles with different materials, provided that the decomposition of the liquid precursor occurs before the evaporation. In this thesis, the technique was demonstrated by synthesizing titania-encapsulated iron oxide nanoparticles. As titania and iron oxide are known to possess photocatalytic and magnetic properties, respectively, the produced particles could find use as magnetically separable photocatalyst nanopowder.

Ceramic silica and titania nanoparticles were coated with silver by physical vapor condensation. The homogeneous nucleation of the evaporated silver was minimized by optimizing the temperature gradient after the evaporation. It was found that the morphology of the multicomponent particles depended strongly on the material of the carrier particles. Silver formed small nanodots with diameter of 1–10 nm on silica particles, whereas, larger silver structures with diameter of 20–100 nm were formed on titania particles. Furthermore, the silver structures on these composite doublet particles had different shapes, such as, triangular, rod-like, and hexagonal. It was proposed that the silver migration on the titania particles was the main mechanism leading to this interesting morphology.

Localized surface plasmon resonance, a phenomenon that predominantly determines the linear optical properties of noble metal nanoparticles, can be utilized in applications, such as, colored coatings, biosensors, and solar cells. The use of aerosol techniques in the fabrication of plasmonic materials has increased rapidly in the recent years. In this thesis, the resonance wavelength of spherical silver nanoparticles deposited on a glass substrate was tuned between approximately 400 – 450 nm. In addition, as the particles were fairly large, higher order resonances were observed. However, due to the random particle deposition process, the particle – particle contacts on the substrate caused unwanted spectral broadening with higher area fractions. Silver-decorated nanoparticles, on the other hand, retained the narrow plasmon resonance even for high particle number densities, thus, allowing the fabrication of thicker bulk-type optical structures.

Multilayer nanostructures consisting of alternating layers of silver-decorated silica nanoparticles and pure silica were used as metamaterials with the ability to double the frequency of the incident laser light. This second-harmonic generation was measured for the first time from a nanostructure fabricated with aerosol techniques. Due to the porous structure of the deposited nanoparticle layers, non-centrosymmetric bulk-type materials, required for the second-order nonlinear optical process, were formed. As the fabricated nonlinear optical materials were not optimized, the achieved conversion efficiency could be further improved by at least a few orders of magnitude. Furthermore, the nonlinear optical properties of similar bulk-type multilayer nanostructures, fabricated by atomic layer deposition, are currently being studied (Alloatti et al., 2015; Clemmen et al., 2015).

All of the introduced and studied synthesis techniques and applications for the aerosol nanoparticles require further development and extensive research before they can be adapted to the industrial scale. However, I am confident that many of the issues considered in this thesis are of interest to people working with aerosol synthesis or nanotechnology in general. The enormous progress in the nanotechnology, even during the relatively short period of my doctoral thesis project, has become evident for me. Although, prediction is very difficult, especially about the future, it is very likely that the nano is here to stay.

Bibliography

Abdullah, M., Shibamoto, S., and Okuyama, K., "Synthesis of ZnO/SiO_2 nanocomposites emitting specific luminescence colors," *Optical Materials*, vol. 26, no. 1, pp. 95–100, 2004.

Ahonen, P. P., Kauppinen, E. I., Joubert, J. C., Deschanvres, J. L., and Van Tendeloo, G., "Preparation of nanocrystalline titania powder via aerosol pyrolysis of titanium tetrabutoxide," *Journal of Materials Research*, vol. 14, no. 10, pp. 3938–3948, 1999.

Ahonen, P. P., Joutsensaari, J., Richard, O., Tapper, U., Brown, D. P., Jokiniemi, J. K., and Kauppinen, E. I., "Mobility size development and the crystallization path during aerosol decomposition synthesis of TiO_2 particles," *Journal of Aerosol Science*, vol. 32, no. 5, pp. 615–630, 2001.

Alanen, J., Saukko, E., Lehtoranta, K., Murtonen, T., Timonen, H., Hillamo, R., Karjalainen, P., Kuuluvainen, H., Harra, J., Keskinen, J., and Rönkkö, T., "The formation and physical properties of the particle emissions from a natural gas engine," *Fuel*, vol. 162, pp. 155–161, 2015.

Alcock, C. B., Itkin, V. P., and Horrigan, M. K., "Vapour pressure equations for the metallic elements: 298–2500K," *Canadian Metallurgical Quarterly*, vol. 23, no. 3, pp. 309–313, 1984.

Alloatti, L., Kieninger, C., Froelich, A., Lauermann, M., Frenzel, T., Köhnle, K., Freude, W., Leuthold, J., Wegener, M., and Koos, C., "Second-order nonlinear optical metamaterials: ABC-type nanolaminates," *Applied Physics Letters*, vol. 107, no. 12, p. 121903, 2015.

Álvarez, P. M., Jaramillo, J., López-Piñero, F., and Plucinski, P. K., "Preparation and characterization of magnetic TiO_2 nanoparticles and their utilization for the degradation of emerging pollutants in water," *Applied Catalysis B: Environmental*, vol. 100, no. 1–2, pp. 338–345, 2010.

Anker, J. N., Hall, W. P., Lyandres, O., Shah, N. C., Zhao, J., and Van Duyne, R. P., "Biosensing with plasmonic nanosensors," *Nature Materials*, vol. 7, no. 6, pp. 442–453, 2008.

Aouani, H., Navarro-Cia, M., Rahmani, M., Sidiropoulos, T. P. H., Hong, M., Oulton, R. F., and Maier, S. A., "Multiresonant broadband optical antennas as efficient tunable nanosources of second harmonic light," *Nano Letters*, vol. 12, no. 9, pp. 4997–5002, 2012.

Arffman, A., Yli-Ojanperä, J., Kalliokoski, J., Harra, J., Pirjola, L., Karjalainen, P., Rönkkö, T., and Keskinen, J., "High-resolution low-pressure cascade impactor," *Journal of Aerosol Science*, vol. 78, pp. 97–109, 2014.

Arffman, A., Kuuluvainen, H., Harra, J., Vuorinen, O., Juuti, P., Yli-Ojanperä, J., Mäkelä, J. M., and Keskinen, J., "The critical velocity of rebound determined for sub-micron silver particles with a variable nozzle area impactor," *Journal of Aerosol Science*, vol. 86, pp. 32–43, 2015.

Aromaa, M., Keskinen, H., and Mäkelä, J. M., "The effect of process parameters on the Liquid Flame Spray generated titania nanoparticles," *Biomolecular Engineering*, vol. 24, no. 5, pp. 543–548, 2007.

Aromaa, M., Arffman, A., Suhonen, H., Haapanen, J., Keskinen, J., Honkanen, M., Nikkanen, J.-P., Levänen, E., Messing, M. E., Deppert, K., Teisala, H., Tuominen, M., Kuusipalo, J., Stepien, M., Saarinen, J. J., Toivakka, M., and Mäkelä, J. M., "Atmospheric synthesis of superhydrophobic TiO_2 nanoparticle deposits in a single step using Liquid Flame Spray," *Journal of Aerosol Science*, vol. 52, pp. 57–68, 2012.

Ashby, M. F., "A first report on sintering diagrams," *Acta Metallurgica*, vol. 22, no. 3, pp. 275–289, 1974.

Atwater, H. A. and Polman, A., "Plasmonics for improved photovoltaic devices," *Nature Materials*, vol. 9, no. 3, pp. 205–213, 2010.

Backman, U., Tapper, U., and Jokiniemi, J. K., "An aerosol method to synthesize supported metal catalyst nanoparticles," *Synthetic Metals*, vol. 142, no. 1–3, pp. 169–176, 2004.

Bartholomew, C. H., "Mechanisms of catalyst deactivation," *Applied Catalysis A: General*, vol. 212, no. 1–2, pp. 17–60, 2001.

Bautista, G., Huttunen, M. J., Mäkitalo, J., Kontio, J. M., Simonen, J., and Kauranen, M., "Second-harmonic generation imaging of metal nano-objects with cylindrical vector beams," *Nano Letters*, vol. 12, no. 6, pp. 3207–3212, 2012.

Belardini, A., Larciprete, M. C., Centini, M., Fazio, E., Sibilia, C., Bertolotti, M., Toma, A., Chiappe, D., and de Mongeot, F. B., "Tailored second harmonic generation from self-organized metal nano-wires arrays," *Optics Express*, vol. 17, no. 5, pp. 3603–3609, 2009.

Beydoun, D., Amal, R., Low, G. K.-C., and McEvoy, S., "Novel photocatalyst: Titania-coated magnetite. Activity and photodissolution," *Journal of Physical Chemistry B*, vol. 104, no. 18, pp. 4387–4396, 2000.

Binder, A., Heel, A., and Kasper, G., "Deposition of palladium nanodots of controlled size and density onto surface-modified SiO_2 particles by an atmospheric pressure CVS/MOCVD process," *Chemical Vapor Deposition*, vol. 13, no. 1, pp. 48–54, 2007.

Binder, A., Seipenbusch, M., and Kasper, G., "Sintering of Pd catalyst particles on SiO_2–TiO_2 carrier particles of different mixing ratios," *Journal of Physical Chemistry C*, vol. 114, no. 17, pp. 7816–7821, 2010.

Blattmann, C. O., Sotiriou, G. A., and Pratsinis, S. E., "Rapid synthesis of flexible conductive polymer nanocomposite films," *Nanotechnology*, vol. 26, no. 12, p. 125601, 2015.

Boies, A. M., Lei, P., Calder, S., and Girshick, S. L., "Gas-phase production of gold-decorated silica nanoparticles," *Nanotechnology*, vol. 22, no. 31, p. 315603, 2011.

Boyd, R. W., *Nonlinear Optics*, 3rd ed. Burlington, MA, USA: Academic Press, 2008.

BUONAPART-E, "Better upscaling and optimization of nanoparticle and nanostructure production by means of electrical discharges," http://www.buonapart-e.eu, 2014, accessed: 2015-09-10.

Buyukhatipoglu, K. and Morss Clyne, A., "Controlled flame synthesis of αFe_2O_3 and Fe_3O_4 nanoparticles: Effect of flame configuration, flame temperature, and additive loading," *Journal of Nanoparticle Research*, vol. 12, no. 4, pp. 1495 – 1508, 2010.

Cai, W., Vasudev, A. P., and Brongersma, M. L., "Electrically controlled nonlinear generation of light with plasmonics," *Science*, vol. 333, no. 6050, pp. 1720 – 1723, 2011.

Campagnola, P. J. and Loew, L. M., "Second-harmonic imaging microscopy for visualizing biomolecular arrays in cells, tissues and organisms," *Nature Biotechnology*, vol. 21, no. 11, pp. 1356 – 1360, 2003.

Chen, B. T., Fletcher, R. A., and Cheng, Y.-S., "Calibration of aerosol instruments," in *Aerosol Measurement: Principles, Techniques, and Applications*, 3rd ed., Kulkarni, P., Baron, P. A., and Willeke, K., Eds. Hoboken, NJ, USA: John Wiley & Sons, 2011, pp. 449 – 478.

Chen, C. K., de Castro, A. R. B., and Shen, Y. R., "Surface-enchanced second-harmonic generation," *Physical Review Letters*, vol. 46, no. 2, pp. 145 – 148, 1981.

Chen, C., Wu, Y., Jiang, A., Wu, B., You, G., Li, R., and Lin, S., "New nonlinear-optical crystal: LiB_3O_5," *Journal of the Optical Society of America B: Optical Physics*, vol. 6, no. 4, pp. 616 – 621, 1989.

Chiarello, G. L., Selli, E., and Forni, L., "Photocatalytic hydrogen production over flame spray pyrolysis-synthesised TiO_2 and Au/TiO_2," *Applied Catalysis B: Environmental*, vol. 84, no. 1 – 2, pp. 332 – 339, 2008.

Chong, M. N., Jin, B., Chow, C. W. K., and Saint, C., "Recent developments in photocatalytic water treatment technology: A review," *Water Research*, vol. 44, no. 10, pp. 2997 – 3027, 2010.

Clemmen, S., Hermans, A., Baets, R. G., Solano, E., Dendooven, J., Detavernier, C., Koskinen, K., Kauranen, M., and Brainis, E., "Atomic layer deposited second order nonlinear optical metamaterial for back-end integration with CMOS-compatible nanophotonic circuitry," *Optics Letters*, 2015, in press, available: http://www.osapublishing.org/abstract.cfm?msid=248367.

Costa, A., Ballarin, B., Spegni, A., Casoli, F., and Gardini, D., "Synthesis of nanostructured magnetic photocatalyst by colloidal approach and spray – drying technique," *Journal of Colloid and Interface Science*, vol. 388, no. 1, pp. 31 – 39, 2012.

de Faria, D. L. A., Silva, S. V., and de Oliveira, M. T., "Raman microspectroscopy of some iron oxides and oxyhydroxides," *Journal of Raman Spectroscopy*, vol. 28, no. 11, pp. 873–878, 1997.

Deppert, K. and Magnusson, M. H., "On the sintering behavior of nanoparticles," *Journal of Aerosol Science*, vol. 32, no. S1, pp. 227–228, 2001.

Deppert, K., Maximov, I., Samuelson, L., Hansson, H.-C., and Weidensohler, A., "Sintered aerosol masks for dry-etched quantum dots," *Applied Physics Letters*, vol. 64, no. 24, pp. 3293–3295, 1994.

Du, J., Harra, J., Virkki, M., Mäkelä, J. M., Leng, Y., Kauranen, M., and Kobayashi, T., "Surface-enhanced femtosecond real-time vibrational spectroscopy," 2015, in preparation.

Eggersdorfer, M. L. and Pratsinis, S. E., "Agglomerates and aggregates of nanoparticles made in the gas phase," *Advanced Powder Technology*, vol. 25, no. 1, pp. 71–90, 2014.

El-Shall, M. S., Slack, W., Vann, W., Kane, D., and Hanley, D., "Synthesis of nanoscale metal oxide particles using laser vaporization/condensation in a diffusion cloud chamber," *Journal of Physical Chemistry*, vol. 98, no. 12, pp. 3067–3070, 1994.

Elvers, B., Ed., *Ullmann's Encyclopedia of Industrial Chemistry*, 7th ed. Weinheim, Germany: Wiley-VHC, 2009.

Feth, N., Linden, S., Klein, M. W., Decker, M., Niesler, F. B. P., Zeng, Y., Hoyer, W., Liu, J., Koch, S. W., Moloney, J. V., and Wegener, M., "Second-harmonic generation from complementary split-ring resonators," *Optics Letters*, vol. 33, no. 17, pp. 1975–1977, 2008.

Feynman, R. P., "There's plenty of room at the bottom," *Journal of Microelectromechanical Systems*, vol. 1, no. 1, pp. 60–66, 1992.

Franken, P. A., Hill, A. E., Peters, C. W., and Weinreich, G., "Generation of optical harmonics," *Physical Review Letters*, vol. 7, no. 4, pp. 118–119, 1961.

Freestone, I., Meeks, N., Sax, M., and Higgitt, C., "The Lycurgus Cup — A Roman nanotechnology," *Gold Bulletin*, vol. 40, no. 4, pp. 270–277, 2007.

Fujishima, A., Rao, T. N., and Tryk, D. A., "Titanium dioxide photocatalysis," *Journal of Photochemistry and Photobiology C: Photochemistry Reviews*, vol. 1, no. 1, pp. 1–21, 2000.

Gao, Y., Chen, B., Li, H., and Ma, Y., "Preparation and characterization of a magnetically separated photocatalyst and its catalytic properties," *Materials Chemistry and Physics*, vol. 80, no. 1, pp. 348–355, 2003.

Gontier-Moya, E. G., Beszeda, I., and Moya, F., "Comparisons of parameters involved in mass transport and desorption at the surface of noble metals and sapphire," *Surface Science*, vol. 566–568, pp. 148–154, 2004.

Grinblat, G., Rahmani, M., Cortés, E., Caldarola, M., Comedi, D., Maier, S. A., and Bragas, A. V., "High-efficiency second harmonic generation from a single hybrid ZnO nanowire/Au plasmonic nano-oligomer," *Nano Letters*, vol. 14, no. 11, pp. 6660–6665, 2014.

Gross, K. A., Tikkanen, J., Keskinen, J., Pitkänen, V., Eerola, M., Siikamaki, R., and Rajala, M., "Liquid flame spraying for glass coloring," *Journal of Thermal Spray Technology*, vol. 8, no. 4, pp. 583 – 589, 1999.

Gunawan, C., Teoh, W. Y., Marquis, C. P., Lifia, J., and Amal, R., "Reversible antimicrobial photoswitching in nanosilver," *Small*, vol. 5, no. 3, pp. 341 – 344, 2009.

Gurav, A., Kodas, T., Pluym, T., and Xiong, Y., "Aerosol processing of materials," *Aerosol Science and Technology*, vol. 19, no. 4, pp. 411 – 452, 1993.

Haapanen, J., Aromaa, M., Teisala, H., Tuominen, M., Stepien, M., Saarinen, J. J., Heikkilä, M., Toivakka, M., Kuusipalo, J., and Mäkelä, J. M., "Binary TiO_2/SiO_2 nanoparticle coating for controlling the wetting properties of paperboard," *Materials Chemistry and Physics*, vol. 149 – 150, pp. 230 – 237, 2015.

Harra, J., "Miniaturization of a Unipolar Aerosol Charger Based on Corona Discharge," Master's thesis, Tampere University of Technology, 2010, in Finnish.

Harris, P. J. F., "Growth and structure of supported metal catalyst particles," *International Materials Reviews*, vol. 40, no. 3, pp. 97 – 115, 1995.

Haynes, C. L. and Van Duyne, R. P., "Nanosphere lithography: A versatile nanofabrication tool for studies of size-dependent nanoparticle optics," *Journal of Physical Chemistry B*, vol. 105, no. 24, pp. 5599 – 5611, 2001.

Haynes, W. M., Ed., *CRC Handbook of Chemistry and Physics*, 96th ed. Boca Raton, FL, USA: CRC Press/Taylor and Francis, 2016.

Heel, A. and Kasper, G., "Production and characterization of Pd/SiO_2 catalyst nanoparticles from a continuous MOCVS/MOCVD aerosol process at atmospheric pressure," *Aerosol Science and Technology*, vol. 39, no. 11, pp. 1027 – 1037, 2005.

Heurlin, M., Magnusson, M. H., Lindgren, D., Ek, M., Wallenberg, L. R., Deppert, K., and Samuelson, L., "Continuous gas-phase synthesis of nanowires with tunable properties," *Nature*, vol. 492, no. 7427, pp. 90 – 94, 2012.

Hinds, W. C., *Aerosol Technology: Properties, Behavior, and Measurement of Airborne Particles*, 2nd ed. New York, NY, USA: John Wiley & Sons, 1999.

Hirsch, L. R., Stafford, R. J., an S. R. Sershen, J. A. B., Rivera, B., Price, R. E., Hazle, J. D., Halas, N. J., and West, J. L., "Nanoshell-mediated near-infrared thermal therapy of tumors under magnetic resonance guidance," *Proceedings of the National Academy of Sciences of the United States of America*, vol. 100, no. 23, pp. 13 549 – 13 554, 2003.

Järvinen, A., Aitomaa, M., Rostedt, A., Keskinen, J., and Yli-Ojanperä, J., "Calibration of the new electrical low pressure impactor (ELPI+)," *Journal of Aerosol Science*, vol. 69, pp. 150 – 159, 2014.

Järvinen, A., Kuuluvainen, H., Niemi, J., Saari, S., Dal Maso, M., Pirjola, L., Hillamo, R., Janka, K., Keskinen, J., and Rönkkö, T., "Monitoring urban air quality with a diffusion charger based electrical particle sensor," *Urban Climate*, 2015, in press, doi: 10.1016/j.uclim.2014.10.002.

Jiang, Y., Wang, W.-N., Biswas, P., and Fortner, J. D., "Facile aerosol synthesis and characterization of ternary crumpled graphene–TiO_2–magnetite nanocomposites for advanced water treatment," *ACS Applied Materials & Interfaces*, vol. 6, no. 14, pp. 11 766–11 774, 2014.

Jung, K., Song, H.-J., Lee, G., Ko, Y., Ahn, K., Choi, H., Kim, J. Y., Ha, K., Song, J., Lee, J.-K., Lee, C., and Choi, M., "Plasmonic organic solar cells employing nanobump assembly *via* aerosol-derived nanoparticles," *ACS Nano*, vol. 8, no. 3, pp. 2590–2601, 2014.

Kangasluoma, J., Junninen, H., Lehtipaloa, K., Mikkilä, J., Vanhanen, J., Attoui, M., Sipilä, M., Worsnop, D., Kulmala, M., and Petäjä, T., "Remarks on ion generation for CPC detection efficiency studies in sub-3-nm size range," *Aerosol Science and Technology*, vol. 47, no. 5, pp. 556–563, 2013.

Karlsson, M. N. A., Deppert, K., Karlsson, L. S., Magnusson, M. H., Malm, J. O., and Srinivasan, N. S., "Compaction of agglomerates of aerosol nanoparticles: A compilation of experimental data," *Journal of Nanoparticle Research*, vol. 7, no. 1, pp. 43–40, 2005.

Karlsson, M. N. A., Deppert, K., Magnusson, M. H., Karlsson, L. S., and Malm, J.-O., "Size- and composition-controlled Au–Ga aerosol nanoparticles," *Aerosol Science and Technology*, vol. 38, no. 9, pp. 948–954, 2004.

Kauranen, M. and Zayats, A. V., "Nonlinear plasmonics," *Nature Photonics*, vol. 6, no. 11, pp. 737–748, 2012.

Kelly, K. L., Coronado, E., Zhao, L. L., and Schatz, G. C., "The optical properties of metal nanoparticle: The influence of size, shape, and dielectric environment," *Journal of Physical Chemistry B*, vol. 107, no. 3, pp. 668–677, 2003.

Keskinen, H., Mäkelä, J. M., Aromaa, M., Keskinen, J., Areva, S., Teixeira, C. V., Rosenholm, J. B., Pore, V., Ritala, M., Leskelä, M., Raulio, M., Salkinoja-Salonen, M. S., Levänen, E., and Mäntylä, T., "Titania and titania-silver nanoparticle deposits made by Liquid Flame Spray and their functionality as photocatalyst for organic- and biofilm removal," *Catalysis Letters*, vol. 111, no. 3–4, pp. 127–132, 2006.

Keskinen, H., Tricoli, A., Marjamäki, M., Mäkelä, J. M., and Pratsinis, S. E., "Size-selected agglomerates of SnO_2 nanoparticles as gas sensors," *Journal of Applied Physics*, vol. 106, no. 8, p. 084316, 2009.

Keskinen, J., Pietarinen, K., and Lehtimäki, M., "Electrical low pressure impactor," *Journal of Aerosol Science*, vol. 23, no. 4, pp. 353–360, 1992.

Kim, H., Kim, J., Yang, H., Suh, J., Kim, T., Han, B., Kim, S., Kim, D. S., Pikhitsa, P. V., and Choi, M., "Parallel patterning of nanoparticles via electrodynamic focusing of charged aerosols," *Nature Nanotechnology*, vol. 1, no. 2, pp. 117–121, 2006.

Klein, M. W., Enkrich, C., Wegener, M., and Linden, S., "Second-harmonic generation from magnetic metamaterials," *Science*, vol. 313, no. 5786, pp. 502–504, 2006.

Klein, M. W., Wegener, M., Feth, N., and Linden, S., "Experiments on second- and third-harmonic generation from magnetic metamaterials: Erratum," *Optics Express*, vol. 16, no. 11, pp. 8055–8055, 2008.

Knutson, E. O. and Whitby, K. T., "Aerosol classification by electric mobility: Apparatus, theory, and applications," *Journal of Aerosol Science*, vol. 6, no. 6, pp. 443–451, 1975.

Kontio, J. M., Husu, H., Simonen, J., Huttunen, M. J., Tommila, J., Pessa, M., and Kauranen, M., "Nanoimprint fabrication of gold nanocones with ∼10 nm tips for enhanced optical interactions," *Optics Letters*, vol. 34, no. 13, pp. 1979–1981, 2009.

Kreibig, U., "Interface-induced dephasing of Mie plasmon polaritons," *Applied Physics B: Lasers and Optics*, vol. 93, no. 1, pp. 79–89, 2008.

Kreibig, U. and Vollmer, M., *Optical Properties of Metal Clusters*. New York, NY, USA: Springer, 1995.

Krinke, T. J., Deppert, K., Magnusson, M. H., Schmidt, F., and Fissan, H., "Microscopic aspects of the deposition of nanoparticles from the gas phase," *Journal of Aerosol Science*, vol. 33, no. 10, pp. 1341–1359, 2002.

Kruis, F. E., Fissan, H., and Peled, A., "Synthesis of nanoparticles in the gas phase for electronic, optical and magnetic applications—A review," *Journal of Aerosol Science*, vol. 29, no. 5–6, pp. 511–535, 1998.

Ku, B. K. and Maynard, A. D., "Generation and investigation of airborne silver nanoparticles with specific size and morphology by homogeneous nucleation, coagulation and sintering," *Journal of Aerosol Science*, vol. 37, no. 4, pp. 452–470, 2006.

Kulkarni, P., Baron, P. A., and Willeke, K., Eds., *Aerosol Measurement: Principles, Techniques, and Applications*, 3rd ed. Hoboken, NJ, USA: John Wiley & Sons, 2011.

Kuuluvainen, H., Kannosto, J., Virtanen, A., Mäkelä, J. M., Kulmala, M., Aalto, P., and Keskinen, J., "Technical Note: Measuring condensation sink and ion sink of atmospheric aerosols with the electrical low pressure impactor (ELPI)," *Atmospheric Chemistry and Physics*, vol. 10, pp. 1361–1368, 2010.

Lee, H., You, S., Pikhitsa, P. V., Kim, J., Kwon, S., Woo, C. G., and Choi, M., "Three-dimensional assembly of nanoparticles from charged aerosols," *Nano Letters*, vol. 11, no. 1, pp. 119–124, 2011.

Li, X., John, V. T., Zhan, J., He, G., He, J., and Spinu, L., "The synthesis of mesoporous $TiO_2/SiO_2/Fe_2O_3$ hybrid particles containing micelle-induced macropores through an aerosol based process," *Langmuir*, vol. 27, no. 10, pp. 6252–6259, 2011.

Liz-Marzán, L. M., "Nanometals: Formation and color," *Materials Today*, vol. 7, no. 2, pp. 26–31, 2004.

Lu, H., Liu, X., Zhou, R., Gong, Y., and Mao, D., "Second-harmonic generation from metal-film nanohole arrays," *Applied Optics*, vol. 49, no. 12, pp. 2347–2351, 2010.

Lu, Z. G. and Zhu, J. H., "Thermal evaporation of pure Ag in SOFC-relevant environments," *Electrochemical and Solid State Letters*, vol. 10, no. 10, pp. B179–B182, 2007.

Luo, J., Jang, H. D., Sun, T., Xiao, L., He, Z., Katsoulidis, A. P., Kanatzidis, M. G., Gibson, J. M., and Huang, J., "Compression and aggregation-resistant particles of crumpled soft sheets," *ACS Nano*, vol. 5, no. 11, pp. 8943–8949, 2011.

Mädler, L., Stark, W. J., and Pratsinis, S. E., "Simultaneous deposition of Au nanoparticles during flame synthesis of TiO_2 and SiO_2," *Journal of Materials Research*, vol. 18, no. 1, pp. 115–120, 2003.

Mädler, L., Roessler, A., Pratsinis, S. E., Sahm, T., Gurlo, A., Barsan, N., and Weimar, U., "Direct formation of highly porous gas-sensing films by in situ thermophoretic deposition of flame-made Pt/SnO_2 nanoparticles," *Sensors and Actuators B: Chemical*, vol. 114, no. 1, pp. 283–295, 2006.

Magnusson, M. H., Deppert, K., Malm, J.-O., Bovin, J.-O., and Samuelson, L., "Gold nanoparticles: Production, reshaping, and thermal charging," *Journal of Nanoparticle Research*, vol. 1, no. 2, pp. 243–251, 1999.

Magnusson, M. H., Ohlsson, B. J., Björk, M. T., Dick, K. A., Borgström, M. T., Deppert, K., and Samuelson, L., "Semiconductor nanostructures enabled by aerosol technology," *Frontiers of Physics*, vol. 9, no. 3, pp. 398–418, 2014.

Mäkelä, J. M., Keskinen, H., Forsblom, T., and Keskinen, J., "Generation of metal and metal oxide nanoparticles by liquid flame spray process," *Journal of Materials Science*, vol. 39, no. 8, pp. 2783–2788, 2004.

Maker, P. D., Terhune, R. W., Nisenoff, M., and Savage, C. M., "Effects of dispersion and focusing on the production of optical harmonics," *Physical Review Letters*, vol. 8, no. 1, pp. 21–22, 1962.

Messing, M. E., Dick, K. A., Wallenberg, L. R., and Deppert, K., "Generation of size-selected gold nanoparticles by spark discharge — For growth of epitaxial nanowires," *Gold Bulletin*, vol. 42, no. 1, pp. 20–26, 2009.

Moravec, P., Smolík, J., and Levdansky, V. V., "Preparation of TiO_2 fine particles by thermal decomposition of titanium tetraisopropoxide vapor," *Journal of Materials Science Letters*, vol. 20, no. 20, pp. 2033–2037, 2001.

Nakaso, K., Shimada, M., Okuyama, K., and Deppert, K., "Evaluation of the change in the morphology of gold nanoparticles during sintering," *Journal of Aerosol Science*, vol. 33, no. 7, pp. 1061–1074, 2002.

O'Connor, D. and Zayats, A. V., "Data storage: The third plasmonic revolution," *Nature Nanotechnology*, vol. 5, no. 7, pp. 482–483, 2010.

Ohtani, B., Ogawa, Y., and ichi Nishimoto, S., "Photocatalytic activity of amorphous–anatase mixture of titanium(IV) oxide particles suspended in aqueous solutions," *Journal of Physical Chemistry B*, vol. 101, no. 19, pp. 3746–3752, 1997.

Okuyama, K., Kousaka, Y., Tohge, N., Yamamoto, S., Wu, J. J., Flagan, R. C., and Seinfeld, J. H., "Production of ultrafine metal oxide aerosol particles by thermal decomposition of metal alkoxide vapors," *AIChE Journal*, vol. 32, no. 12, pp. 2010–2019, 1986.

Oldenburg, S. J., Averitt, R. D., Westcott, S. L., and Halas, N. J., "Nanoengineering of optical resonances," *Chemical Physics Letters*, vol. 288, no. 2–4, pp. 243–247, 1998.

Park, S., Hahn, J. W., and Lee, J. Y., "Doubly resonant metallic nanostructure for high conversion efficiency of second harmonic generation," *Optics Express*, vol. 20, no. 5, pp. 4856–4870, 2012.

Pfeiffer, T. V., Ortiz-Gonzalez, J., Santbergen, R., Tan, H., Schmidt Ott, A., Zeman, M., and Smets, A. H. M., "Plasmonic nanoparticle films for solar cell applications fabricated by size-selective aerosol deposition," *Energy Procedia*, vol. 60, pp. 3–12, 2014.

Pfeiffer, T. V., Kedia, P., Messing, M. E., Valvo, M., and Schmidt-Ott, A., "Precursor-less coating of nanoparticles in the gas phase," *Materials*, vol. 8, no. 3, pp. 1027–1042, 2015.

Pinna, N., Grancharov, S., Beato, P., Bonville, P., Antonietti, M., and Niederberger, M., "Magnetite nanocrystals: Nonaqueous synthesis, characterization, and solubility," *Chemistry of Materials*, vol. 17, no. 11, pp. 3044–3049, 2005.

Polshettiwar, V., Luque, R., Fihri, A., Zhu, H., Bouhrara, M., and Basset, J.-M., "Magnetically recoverable nanocatalysts," *Chemical Reviews*, vol. 111, no. 5, pp. 3036–3075, 2011.

Pratsinis, S. E., "Flame aerosol synthesis of ceramic powders," *Progress in Energy and Combustion Science*, vol. 24, no. 5, pp. 197–219, 1998.

Risk, W. P., Gosnell, T. R., and Nurmikko, A. V., *Compact Blue-Green Lasers*. Cambridge, UK: Cambridge University Press, 2003.

Saarinen, J. J., Valtakari, D., Haapanen, J., Salminen, T., Mäkelä, J. M., and Uozumi, J., "Surface-enhanced Raman scattering active substrates by liquid flame spray deposited and inkjet printed silver nanoparticles," *Optical Review*, vol. 21, no. 3, pp. 339–344, 2014.

Scheibel, H. G. and Porstendörfer, J., "Generation of monodisperse Ag- and NaCl-aerosols with particle diameters between 2 and 300 nm," *Journal of Aerosol Science*, vol. 14, no. 2, pp. 113–126, 1983.

Schmidt-Ott, A., "New approaches to *in situ* characterization of ultrafine agglomerates," *Journal of Aerosol Science*, vol. 19, no. 5, pp. 553–563, 1988.

Schneider, C. A., Rasband, W. S., and Eliceiri, K. W., "NIH Image to ImageJ: 25 years of image analysis," *Nature Methods*, vol. 9, no. 7, pp. 671–675, 2012.

Schwyn, S., Garwin, E., and Schmidt-Ott, A., "Aerosol generation by spark discharge," *Journal of Aerosol Science*, vol. 19, no. 5, pp. 639–642, 1988.

Shebanova, O. N. and Lazor, P., "Raman spectroscopic study of magnetite ($FeFe_2O_4$): A new assignment for the vibrational spectrum," *Journal of Solid State Chemistry*, vol. 174, no. 2, pp. 424–430, 2003.

Shen, Y. R., "Surface properties probed by second-harmonic and sum-frequency generation," *Nature*, vol. 337, no. 6207, pp. 519–525, 1989.

Shimada, M., Seto, T., and Okuyama, K., "Size change of very fine silver agglomerates by sintering in a heated flow," *Journal of Chemical Engineering of Japan*, vol. 27, no. 6, pp. 795–802, 1994.

Sigmund, S., Akgün, E., Meyer, J., Hubbuch, J., Wörner, M., and Kasper, G., "Defined polymer shells on nanoparticles via a continuous aerosol-based process," *Journal of Nanoparticle Research*, vol. 16, no. 8, p. 2533, 2014.

Sigmund, S., Yu, M., Meyer, J., and Kasper, G., "An aerosol-based process for electrostatic coating of particle surfaces with nanoparticles," *Aerosol Science and Technology*, vol. 48, no. 2, pp. 142–149, 2014.

Skillas, G., Maisels, A., Pratsinis, S. E., and Kodas, T. T., "Manufacturing of materials by aerosol processes," in *Aerosol Measurement: Principles, Techniques, and Applications*, 3rd ed., Kulkarni, P., Baron, P. A., and Willeke, K., Eds. Hoboken, NJ, USA: John Wiley & Sons, 2011, pp. 751–770.

Sotiriou, G. A. and Pratsinis, S. E., "Antibacterial activity of nanosilver ions and particles," *Environmental Science & Technology*, vol. 44, no. 14, pp. 5649–5654, 2010.

Sotiriou, G. A., Sannomiya, T., Teleki, A., Krumeich, F., Vörös, J., and Pratsinis, S. E., "Non-toxic dry-coated nanosilver for plasmonic biosensors," *Advanced Functional Materials*, vol. 20, no. 24, pp. 4250–4257, 2010.

Sotiriou, G. A., Hirt, A. M., Lozach, P.-Y., Teleki, A., Krumeich, F., and Pratsinis, S. E., "Hybrid, silica-coated, Janus-like plasmonic-magnetic nanoparticles," *Chemistry of Materials*, vol. 23, no. 7, pp. 1985–1922, 2011.

Sotiriou, G. A., Teleki, A., Camenzind, A., Krumeich, F., Meyer, A., Panke, S., and Pratsinis, S. E., "Nanosilver on nanostructured silica: Antibacterial activity and Ag surface area," *Chemical Engineering Journal*, vol. 170, no. 2–3, pp. 547–554, 2011.

Sotiriou, G. A., Blattmann, C. O., and Pratsinis, S. E., "Flexible, multifunctional, magnetically actuated nanocomposite films," *Advanced Functional Materials*, vol. 23, no. 1, pp. 34–41, 2013.

Sotiriou, G. A., Etterlin, G. D., Spyrogianni, A., Krumeich, F., Leroux, J.-C., and Pratsinis, S. E., "Plasmonic biocompatible silver–gold alloyed nanoparticles," *Chemical Communications*, vol. 50, no. 88, pp. 13 559–13 562, 2014.

Sotiriou, G. A., Starsich, F., Dasargyri, A., Wurnig, M. C., Krumeich, F., Boss, A., Leroux, J.-C., and Pratsinis, S. E., "Photothermal killing of cancer cells by the controlled plasmonic coupling of silica-coated Au/Fe_2O_3 nanoaggregates," *Advanced Functional Materials*, vol. 24, no. 19, pp. 2818–2827, 2014.

Strobel, R. and Pratsinis, S. E., "Flame aerosol synthesis of smart nanostructured materials," *Journal of Materials Chemistry*, vol. 17, no. 45, pp. 4743–4756, 2007.

———, "Direct synthesis of maghemite, magnetite and wustite nanoparticles by flame spray pyrolysis," *Advanced Powder Technology*, vol. 20, no. 2, pp. 190–194, 2009.

Svensson, C. R., Messing, M. E., Lundqvist, M., Schollin, A., Deppert, K., Pagels, J. H., Rissler, J., and Cedervall, T., "Direct deposition of gas phase generated aerosol gold nanoparticles into biological fluids - Corona formation and particle size shifts," *PLoS ONE*, vol. 8, no. 9, p. e74702, 2013.

Swihart, M. T., "Vapor-phase synthesis of nanoparticles," *Current Opinion in Colloid and Interface Science*, vol. 8, no. 1, pp. 127–133, 2003.

Taniguchi, N., "On the basic concept of nano-technology," in *Proceeding of the International Conference on Production Engineering, Part II.* Tokyo, Japan: Japan Society of Precision Engineering, 1974, pp. 18–23.

Teleki, A., Heine, M. C., Krumeich, F., Akhtar, M. K., and Pratsinis, S. E., "*In situ* coating of flame-made TiO_2 particles with nanothin SiO_2 films," *Langmuir*, vol. 24, no. 21, pp. 12 553 – 12 558, 2008.

Thimsen, E., "Single-step aerosol synthesis and deposition of Au nanoparticles with controlled size and separation distributions," *Chemistry of Materials*, vol. 23, no. 20, pp. 4612 – 4617, 2011.

Thimsen, E., Le Formal, F., Grätzel, M., and Warren, S. C., "Influence of plasmonic Au nanoparticles on the photoactivity of Fe_2O_3 electrodes for water splitting," *Nano Letters*, vol. 11, no. 1, pp. 35 – 43, 2011.

Tikkanen, J., Gross, K. A., Berndt, C. C., Pitkänen, V., Keskinen, J., Raghu, S., Rajala, M., and Karthikeyan, J., "Characteristics of the liquid flame spray process," *Surface and Coatings Technology*, vol. 90, no. 3, pp. 210 – 216, 1997.

Tuovinen, H., Kauranen, M., Jefimovs, K., Vahimaa, P., Vallius, T., Turunen, J., Tkachenko, N. V., and Lemmetyinen, H., "Linear and second-order nonlinear optical properties of arrays of noncentrosymmetric gold nanoparticles," *Journal of Nonlinear Optical Physics & Materials*, vol. 11, no. 4, pp. 421 – 432, 2002.

Valenti, M., Dolat, D., Biskos, G., Schmidt-Ott, A., and Smith, W. A., "Enhancement of the photoelectrochemical performance of $CuWO_4$ thin films for solar water splitting by plasmonic nanoparticle functionalization," *Journal of Physical Chemistry C*, vol. 119, no. 4, pp. 2096 – 2104, 2015.

Wang, S. C. and Flagan, R. C., "Scanning electrical mobility spectrometer," *Aerosol Science and Technology*, vol. 13, no. 2, pp. 230 – 240, 1990.

Watson, S., Beydoun, D., and Amal, R., "Synthesis of a novel magnetic photocatalyst by direct deposition of nanosized TiO_2 crystals onto a magnetic core," *Journal of Photochemistry and Photobiology A: Chemistry*, vol. 148, no. 1 – 3, pp. 303 – 313, 2002.

Weber, A. P. and Friedlander, S. K., "*In situ* determination of the activation energy for restructuring of nanometer aerosol agglomerates," *Journal of Aerosol Science*, vol. 28, no. 2, pp. 179 – 192, 1997.

Willets, K. A. and Van Duyne, R. P., "Localized surface plasmon resonance spectroscopy and sensing," *Annual Review of Physical Chemistry*, vol. 58, pp. 267 – 297, 2007.

Yao, H., Fan, M., Wang, Y., Luob, G., and Feib, W., "Magnetic titanium dioxide based nanomaterials: Synthesis, characteristics, and photocatalytic application in pollutant degradation," *Journal of Materials Chemistry A*, vol. 3, no. 34, pp. 17 511 – 17 524, 2015.

Yli-Ojanperä, J., Mäkelä, J. M., Marjamäki, M., Rostedt, A., and Keskinen, J., "Towards traceable particle number concentration standard: Single charged aerosol reference (SCAR)," *Journal of Aerosol Science*, vol. 41, no. 8, pp. 719 – 728, 2010.

Zdanowicz, M., "Nonlinear Optical Response of Metal Nanoparticles and Nanocomposites," Ph.D. dissertation, Tampere University of Technology, 2014, available: http://URN.fi/URN:ISBN:978-952-15-3358-7.

Zdanowicz, M., Harra, J., Mäkelä, J. M., Heinonen, E., Ning, T., Kauranen, M., and Genty, G., "Second-harmonic response of multilayer nanocomposites of silver-decorated nanoparticles and silica," *Scientific Reports*, vol. 4, p. 5745, 2014.

Zhang, Y., Grady, N. K., Ayala-Orozco, C., and Halas, N. J., "Three-dimensional nanostructures as highly efficient generators of second harmonic light," *Nano Letters*, vol. 11, no. 12, pp. 5519 – 5523, 2011.

Zhao, C., Krall, A., Zhao, H., Zhang, Q., and Li, Y., "Ultrasonic spray pyrolysis synthesis of Ag/TiO_2 nanocomposite photocatalysts for simultaneous H_2 production and CO_2 reduction," *International Journal of Hydrogen Energy*, vol. 37, no. 13, pp. 9967 – 9976, 2012.

Zhou, R., Lu, H., Liu, X., Gong, Y., and Mao, D., "Second-harmonic generation from a periodic array of noncentrosymmetric nanoholes," *Journal of the Optical Society of America B: Optical Physics*, vol. 27, no. 11, pp. 2405 – 2409, 2010.

Zihlmann, S., Lüönd, F., and Spiegel, J. K., "Seeded growth of monodisperse and spherical silver nanoparticles," *Journal of Aerosol Science*, vol. 75, pp. 81 – 93, 2014.

Zumsteg, F. C., Bierlein, J. D., and Gier, T. E., "$K_x\ Rb_{1-x}TiOPO_4$: A new nonlinear optical material," *Journal of Applied Physics*, vol. 47, no. 11, pp. 4980 – 4985, 1976.

Publications

Paper I

Juha Harra, Jouni Mäkitalo, Roope Siikanen, Matti Virkki, Goëry Genty, Takayoshi Kobayashi, Martti Kauranen, and Jyrki M. Mäkelä

"Size-controlled aerosol synthesis of silver nanoparticles for plasmonic materials"

Journal of Nanoparticle Research, vol. 14, no. 6, p. 870, 2012

doi: 10.1007/s11051-012-0870-0

I

J Nanopart Res (2012) 14:870
DOI 10.1007/s11051-012-0870-0

RESEARCH PAPER

Size-controlled aerosol synthesis of silver nanoparticles for plasmonic materials

Juha Harra · Jouni Mäkitalo · Roope Siikanen · Matti Virkki · Goëry Genty · Takayoshi Kobayashi · Martti Kauranen · Jyrki M. Mäkelä

Received: 26 September 2011 / Accepted: 16 April 2012

Abstract Aerosol techniques were used to synthesize spherical and monodisperse silver nanoparticles for plasmonic materials. The particles were generated with an evaporation–condensation technique followed by size selection and sintering with a differential mobility analyzer and a tube furnace, respectively. Finally, the nanoparticles were collected on a glass substrate with an electrostatic precipitator. The particle size distributions were measured with a scanning mobility particle sizer and verified with a transmission electron microscope. A spectrophotometer was used to measure the optical extinction spectra of the prepared samples, which contained particles with diameters of approximately 50, 90 and 130 nm. By controlling the particle size, the dipolar peak of the localized surface plasmon resonance was tuned between wavelengths of 398 and 448 nm. In addition, quadrupolar resonances were observed at shorter wavelengths as predicted by the simplified theoretical model used to characterize the measured spectra.

Keywords Aerosol synthesis · Silver nanoparticle · Localized surface plasmon resonance

J. Harra (✉) · J. M. Mäkelä
Aerosol Physics Laboratory, Department of Physics, Tampere University of Technology, P.O. Box 692, 33101 Tampere, Finland
e-mail: juha.harra@tut.fi

J. Mäkitalo · R. Siikanen · M. Virkki · G. Genty · M. Kauranen
Optics Laboratory, Department of Physics, Tampere University of Technology, P.O. Box 692, 33101 Tampere, Finland

T. Kobayashi
Advanced Ultrafast Laser Research Center and Department of Engineering Science, University of Electro-Communications, Chofugaoka 1-5-1, Chofu, Tokyo 182-8585, Japan

T. Kobayashi
Core Research for Evolutional Science and Technology (CREST), Japan Science and Technology Agency, K's Gobancho 7, Gobancho, Chiyoda-ku, Tokyo 102-0076, Japan

Introduction

Nanoparticles are widely studied and utilized in many scientific fields due to their unique properties, which differ from the corresponding bulk material. Optical properties of noble metal nanoparticles, such as silver and gold, are dominated by coherent oscillations of conduction electrons which give rise to localized surface plasmon resonances (LSPR) (Kreibig and Vollmer 1995; Halas 2010). These resonances can be tuned to a desired wavelength by changing the particle size, shape and dielectric environment (Kelly et al. 2003). Such tunability is essential for several interesting applications of nanophotonics, including surface-enhanced Raman spectroscopy (Nie and Emory 1997), optical data storage (Ditlbacher et al. 2000), cancer imaging and therapy (Loo et al. 2005),

Published online: 03 June 2012

biomarkers (Sotiriou et al. 2011), biosensors (Hoa et al. 2007), plasmonic solar cells (Catchpole and Polman 2008) and colored coatings (Beyene et al. 2011).

Various techniques have been used to prepare both silver and gold nanoparticles for optical studies, for example ion implantation (Stepanov 2011), sputtering (Xu et al. 2005), pulsed laser deposition (Donnelly et al. 2006) and wet chemical techniques (Liz-Marzán 2004). These techniques usually offer very poor and often rather restricted size control of spherical nanoparticles which results only in relatively small particles with diameters less than ~30 nm. However, the size range of spherical nanoparticles generated in the gas phase with aerosol techniques covers practically the whole nanoscale from a few nanometers to over 100 nm. This gives the opportunity to tune the LSPR more extensively. In addition, aerosol synthesis requires neither expensive vacuum technology nor liquid solvents. Aerosol processes are also continuous, scalable, and the generated nanoparticles can be directly deposited on the desired substrate. Therefore, aerosol synthesis offers high potential for preparing nanoparticles for plasmonic materials.

Different aerosol synthesis techniques of silver nanoparticles have been widely studied (Mäkelä et al. 2004; Ku and Maynard 2006; Tabrizi et al. 2009). In addition, silver nanoparticle samples for different types of applications have been previously prepared with aerosol techniques. For example, Deppert et al. (1994) deposited spherical silver particles on a semiconductor to serve as etch masks for quantum-dot structures and Kang et al. (2004) prepared patterns consisting of silver nanoparticles for electronic devices. More recently, Sotiriou et al. (2010) used a flame aerosol method to prepare silica coated silver particles for plasmonic biosensors. The silica coating prevented flocculation of the silver particles when dispersed in aqueous suspensions. Thus, the plasmon spectrum was tuned by controlling the amount of silica in the samples. However, aerosol techniques, especially the particle size control aspects, have not been fully exploited in the preparation of plasmonic materials.

In the present study, aerosol techniques were used to prepare plasmonic materials. The prepared samples consisted of spherical and monodisperse silver nanoparticles with diameters of approximately 50, 90 and 130 nm deposited on a glass substrate. As a result of the particle size control, the dipolar resonance of the samples was tuned within the wavelengths 398–448 nm. Furthermore, the measured extinction spectra displayed additional peaks at shorter wavelengths. The theoretical calculations confirmed that these peaks are most likely quadrupolar resonances.

Experimental

Figure 1 shows a schematic diagram of the entire experimental setup to prepare the silver nanoparticle samples. The particles were generated using an evaporation–condensation technique introduced by Scheibel and Porstendörfer (1983). A ceramic crucible containing a small amount of bulk silver was placed inside the ceramic worktube of a tube furnace (Carbolite TZF 15/50/610). The silver was evaporated at the center of the furnace at temperatures between 1,300 and 1,400 °C. The formed metal vapor was first carried out of the furnace and then diluted with inert gas streams of nitrogen (N_2). Both flow rates were set at 3 L/min with mass flow controllers (MFC). Because of the sudden temperature decrease after the furnace, the silver vapor condenses to form primary nanoparticles, which then coagulate to form agglomerates. According to previous studies with similar particle generation setup, the chain-like silver agglomerates consist of spherical primary particles with diameters of approximately 20 nm (Weber and Friedlander 1997; Ku and Maynard 2006). In the present study, coagulation was enhanced by placing a coagulation chamber with a volume of 8.5 L in the flow line.

After the chamber, the aerosol passed through a radioactive Am-241 source, which was used for bipolar charging of the particles. A narrow particle size distribution was then selected from the aerosol with a differential mobility analyzer (DMA) (Knutson and Whitby 1975). This standard instrument classifies particles with an electric field according to their electrical mobility, which is a function of the size and charge of an aerosol particle. The selected particles are mostly singly charged, either negatively or positively. The mean size and the width of the selected size distribution can be altered by changing the voltage and flow rates in the DMA. The sheath and excess flow rates of the Vienna type DMA used in this study were set to 10 L/min with MFCs, while the sample flow rate was 1.5 L/min. After the DMA, the size-selected

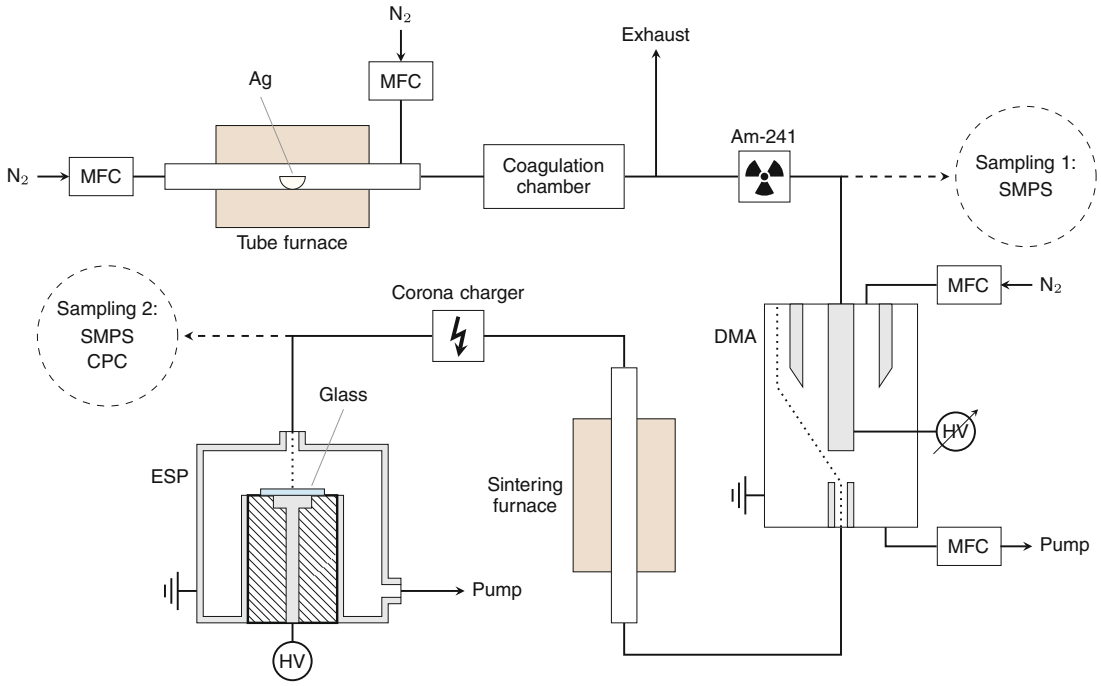

Fig. 1 The experimental setup for preparing silver nanoparticle samples

agglomerates were sintered to spherical nanoparticles in an additional tube furnace (Schmidt-Ott 1988; Karlsson et al. 2005). A quartz worktube was used in the sintering furnace (Carbolite MTF 12/38/400), and the temperature of the furnace was set to 800 °C.

Even though the size-selected and sintered silver particles were already charged, their charge level was increased with a unipolar corona charger to ensure that the electrical mobility of the particles is high enough for electrical collection. An electrostatic precipitator (ESP), similar to the one studied by Krinke et al. (2002), was used to collect the silver nanoparticles on a substrate. The cylinder shaped ESP had an inlet with a diameter of approximately 5 mm which widened to 100 mm inside the ESP. This caused the velocity of the particles to decrease, while a nearly perpendicular electric field of 2.5 kV/cm pulled the charged particles on a substrate which was placed on a round electrode with a diameter of 20 mm. Due to the increased particle charge obtained in the corona charger, the collection efficiency of the ESP exceeded 90 %. The substrates were standard 1 mm thick microscope glass slides. In addition, particles were collected on carbon-coated copper TEM grids for electron microscopy.

A scanning mobility particle sizer (SMPS) (Wang and Flagan 1990) consisting of a DMA (TSI Model 3081) and a condensation particle counter (CPC, TSI Model 3025) was used to measure particle size distributions in the gas phase both before and after the size selection at sampling 1 and sampling 2, respectively. The CPC alone measured the number concentration of the size-selected and sintered particles at sampling 2. After the collection, the nanoparticles were studied with a transmission electron microscope (TEM, Jeol JEM-2010), and particle size distributions were determined from the TEM images with an image processing program ImageJ (Abràmoff et al. 2004). In addition, a scanning electron microscope (SEM, Zeiss ULTRA PLUS) was used to study the actual glass samples with the deposited particles. The extinction spectra of the samples were measured with a UV–VIS spectrophotometer (Shimadzu UV-3600). A clean microscope glass slide was used as a reference sample.

I

Results and discussions

Aerosol measurements

Figure 2 shows the original particle size distribution of silver agglomerates before the size selection for different furnace temperatures at sampling 1. The measured distributions were log-normally distributed ranging from a few nanometers to hundreds of nanometers depending on the temperature of the tube furnace. When the temperature was increased from 1,000 to 1,400 °C, the geometric mean diameter of the size distribution increased approximately from 10 to 70 nm. In addition, the total concentration of the particles increased by approximately two orders of magnitude from 10^5 to 10^7 #/cm^3. Both increases, the particle size and concentration, resulted from the higher evaporation rate of silver at higher temperatures. In order to avoid extensive collection times during the sample preparation, it was preferable to have high particle concentration. Therefore, the tube furnace was set to temperatures of 1,300−1,400 °C during the sample preparation.

Size distributions of the size-selected and sintered particles were measured with the SMPS at sampling 2. Figure 3 shows typical examples of the particle size distributions for different sintering temperatures. When the sintering temperature was increased, the particle concentration decreased. In addition, the size distribution shifted to smaller particle sizes and became slightly narrower. However, at temperatures near the bulk melting point of silver (962 °C), the size distribution clearly broadened. It should also be noted that there is a second, much weaker, particle mode with a larger particle size. This mode partly merges into the main mode when the temperature is increased. These larger particles are most likely doubly charged by the radioactive source. Therefore, they have the same electrical mobility as the desired particles. This results in their selection in the DMA. In order to eliminate these particles and to narrow the size distribution before the collection, another DMA could be used after the sintering furnace for a second size selection. However, that might notably lower the particle concentration and lead to extended collection times.

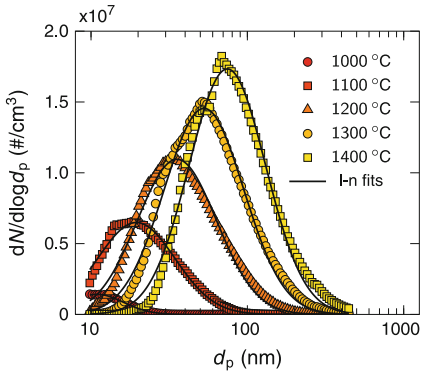

Fig. 2 Size distributions of silver agglomerates for different furnace temperatures. A log-normal distribution has been fitted to each measurement

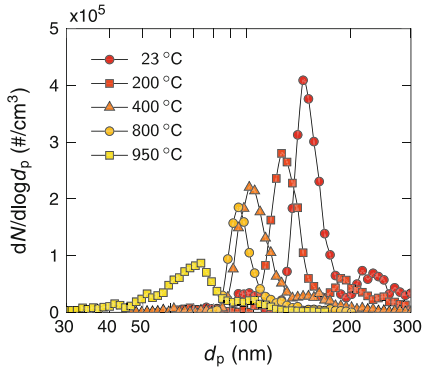

Fig. 3 Size distributions of size-selected silver particles sintered at different temperatures. The temperature of the tube furnace was 1,350 °C

Three particle sizes were chosen for the sample preparation. Agglomerate sizes of approximately 70, 150 and 220 nm were selected with the DMA and sintered to spherical nanoparticles with diameters of approximately 50, 90 and 130 nm, respectively. For the preparation of the 50, 90 and 130 nm particles, tube furnace temperatures of 1,300, 1,350 and 1,400 °C, respectively, were used. Figure 4 shows the mode sizes of the particle size distributions as a function of the sintering temperature for the three size-selected particle sizes. According to Karlsson et al. (2005), the sintering process can be divided into three steps: compaction, internal rearrangement and evaporation, which are also evident in Fig. 4. First, at near room temperatures, the diameter of the agglomerates begins to decrease due to compaction. After the sintering temperature exceeds approximately 300−500 °C, depending on the particle size, the particle

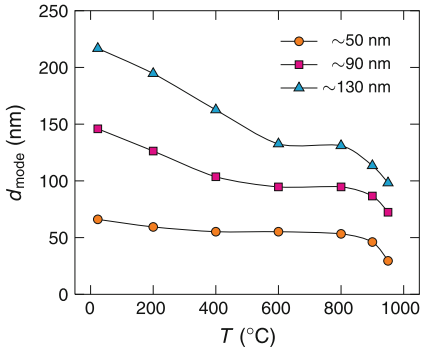

Fig. 4 The mode size of the size-selected silver particles as a function of the sintering temperature. At 800 °C, the particles are spherical with diameters of approximately 50, 90 and 130 nm

diameter stays constant. This means that the compaction has finished. However, internal rearrangements still occur, which lead to spherical particles with higher degree of crystallinity. Finally, at temperatures near the bulk melting point of silver, the particle size suddenly decreases again because of evaporation as reported by Schmidt-Ott (1988). To ensure that the silver nanoparticles were as spherical as possible without excess losses, the sintering temperature was set to 800 °C for the sample preparation.

Figure 5 shows the final normalized size distributions of the three size-selected and sintered particle sizes before the collection. Normal distributions were fitted to the size distributions with mean diameters of 50.3, 94.5 and 132.2 nm and relative standard

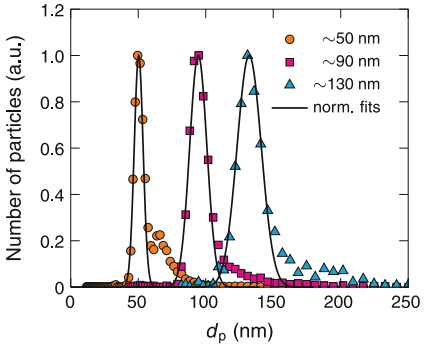

Fig. 5 Normalized size distributions of the size-selected silver particles sintered at 800 °C. The total particle number concentration was $4 \times 10^4, 3 \times 10^4$ and 1.5×10^4 #/cm^3 for the 50, 90 and 130 nm particles, respectively. A normal distribution has been fitted to each measurement

deviations of 9.1, 9.5 and 9.6 %, respectively. The small tails caused by the doubly charged particles were not taken into account in the fitting.

Electron microscopy

Figure 6 shows TEM images of the size-selected and sintered silver nanoparticles collected on carbon-coated copper TEM grids. The sintering was successful, since most of the particles are spherical. However, deviations from spherical shape can be noted with some of the larger silver particles, which are slightly elongated. In addition, some of the particles are attached to each other, most likely during the collection process, and form agglomerates consisting of two or more spherical particles. This means that when the particle coverage on the substrate is increased, the fraction of separated particles will decrease. Moreover, if the spherical particles have a galvanic connection to each other, the optical properties of the nanoparticle samples most likely differ from an ideal situation. A possible way to prevent these galvanic connections would be to coat the silver particles with a dielectric material in the gas phase before the collection. This method could also be used to change the dielectric environment of the particles.

The collection times for the 50, 90 and 130 nm silver particles in the TEM samples were 163, 68 and 57 min, respectively. Rough estimates of the particle coverage on the substrate were made before the collection based on the particle concentration measured with the CPC, the flow rate in the ESP, and the size of the collection electrode. It was assumed that the particles are monodisperse and that the collection was ideal. The estimated particle coverage in all the TEM samples was 6 %, while the coverages calculated from several TEM images for the 50, 90 and 130 nm particles were 4.2, 7.4 and 3.4 %, respectively. The measured coverages are reasonably close to the rough estimate. The reason for the low coverage of the 130 nm particles can be explained with non-ideal collection due to the low electrical mobility of the larger nanoparticles. It was evident that the collection area of the 130 nm particles was slightly larger than the area of the collection electrode.

Particle area distributions in the TEM samples were determined from several TEM images and converted to particle size distributions assuming spherical shape. Figure 7 shows size distributions of the three different

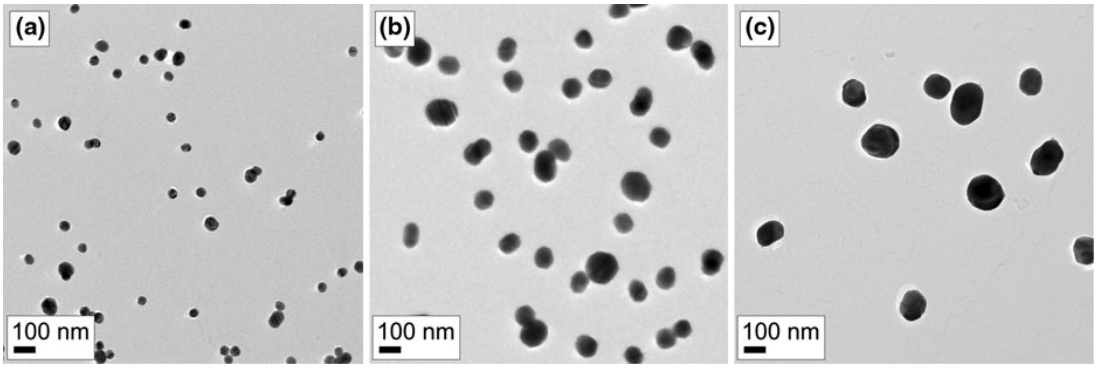

Fig. 6 TEM images of size-selected and sintered silver nanoparticles with diameters of approximately **a** 50, **b** 90 and **c** 130 nm

samples shown in Fig. 6. Clearly all of the size distributions have two distinctive modes. The largest peaks at particle sizes of 46.6, 90.9 and 130.4, with relative standard deviations of 10.7, 9.2 and 8.7, respectively, correspond to separated spherical particles. The particle sizes and deviations are in good agreement with the SMPS measurements in Fig. 5. The second mode is partly caused by the tail extending to larger particles observed in the SMPS measurements. However, the main reason is the agglomeration on the substrate during the collection process as discussed earlier. In Fig. 7, the vertical lines, near the peaks of the second modes, at particle sizes of 71, 127 and 184 nm correspond to two attached spherical 50, 90 and 130 nm particles, respectively.

Figure 8 shows SEM images of the actual samples containing 90 nm silver particles on a glass slide with surface coverages of approximately 2 and 8 %. In the sample with 2 % coverage, the particles are mostly separated whereas the sample with 8 % coverage contains also agglomerates with sizes up to a few hundred nanometers. Sotiriou et al. (2010) found micrometer sized silver agglomerates from nanosilver films on a glass slide. These large agglomerates were formed within an aqueous suspension. However, no similar large silver agglomerates can be found in Fig. 8b and the particles are rather homogeneously dispersed, most likely because in this study the particles were deposited directly on the glass substrate from the aerosol phase. Direct deposition was also applied by Mädler et al. (2006) in the preparation of tin dioxide films using a flame aerosol method. These films were homogeneous and highly porous with a thickness of up to a few tens of micrometers. Evidently, the process yield in flame techniques is much higher than in the more delicate size selective furnace technique used in this study, in which the total process yield was estimated to be on the order of 10 μg/h.

Comparing the optical measurements with the theoretical calculations

Figure 9a–c show extinction spectra of the prepared silver nanoparticle samples with particle diameters of approximately 50, 90 and 130 nm, respectively. Three extinction spectra are shown with each particle size. These spectra correspond to samples with different particle coverages ranging approximately from 2 to 8 %. Obviously, as the particle coverage on the substrate increases, the extinction increases as well.

For qualitative analysis of the measured extinction spectra, the systems were modeled by using a classical electrodynamical approach. A single homogeneous spherical particle in a homogeneous background medium was assumed and the excitation source was modeled as a time-harmonic plane wave. The solution for the problem was obtained by using Mie theory (Bohren and Huffman 1998), and finally the extinction cross-sections were deduced. Two refractive indices, 1.0 and 1.5, were used for the dielectric background medium to examine two extreme cases where the surrounding medium is air or the glass substrate. In addition to single particles, the cross-sections for distributions of spherical particles were calculated by using the size distributions from Fig. 7. The calculated spectra are shown in Fig. 9d–f, for silver particles with diameters of 50, 90 and 130 nm, respectively.

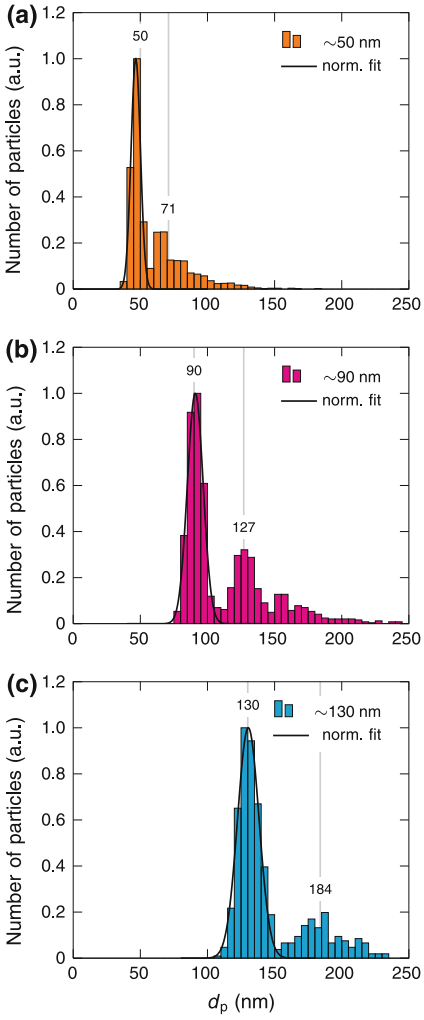

Fig. 7 Size distributions of size-selected and sintered silver nanoparticles with diameters of approximately **a** 50, **b** 90 and **c** 130 nm. The distributions were calculated from several TEM images assuming that particles are spherical. The number of counted particles was 2546, 1289 and 594 for the 50, 90 and 130 nm particles, respectively

The measured extinction spectra display multiple peaks, of which two are near 400 nm and one at a longer wavelength. By comparing the measured spectra to the two single particle theoretical spectra, it can be concluded that the peaks (peak 1) at wavelengths of 398, 415 and 448 nm for the 50, 90 and 130 nm particles, respectively, are most likely dipolar LSPR peaks. The positions of these peaks fit between the dipolar resonance peaks of the two extreme cases.

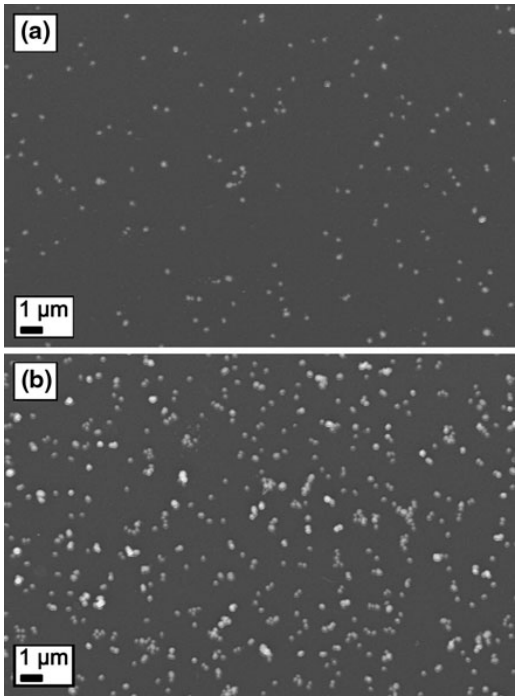

Fig. 8 SEM images of 90 nm silver particles on a glass slide with a surface coverage of approximately **a** 2 and **b** 8 %

In addition to the red-shift of approximately 50 nm, the dipolar LSPR peaks broaden with increasing particle size, as expected from the theoretical calculations. However, the peaks in the measured spectra are not as sharp as implied by the theoretical calculations. This discrepancy can be explained with the low particle coverage in the samples. The average distance between the particles is roughly of the order of the wavelength and the samples contain particle free areas which lead to absorption flattening (Duysens 1956).

In addition to the dipolar resonances, the measured spectra show extinction peaks (peak 2) at shorter wavelengths of 367, 374 and 388 nm for the 50, 90 and 130 nm particles, respectively. Similar resonance peaks, which increase with particle size and refractive index, can be observed in the theoretical results. These peaks are quadrupolar plasmon resonances, as was verified by the theory. For the 50 nm particles, the theory is unable to explain the extinction peak in the measured spectrum as the quadrupolar resonance is very weak. For the larger particles, the quadrupolar resonance most likely contributes to the measurements.

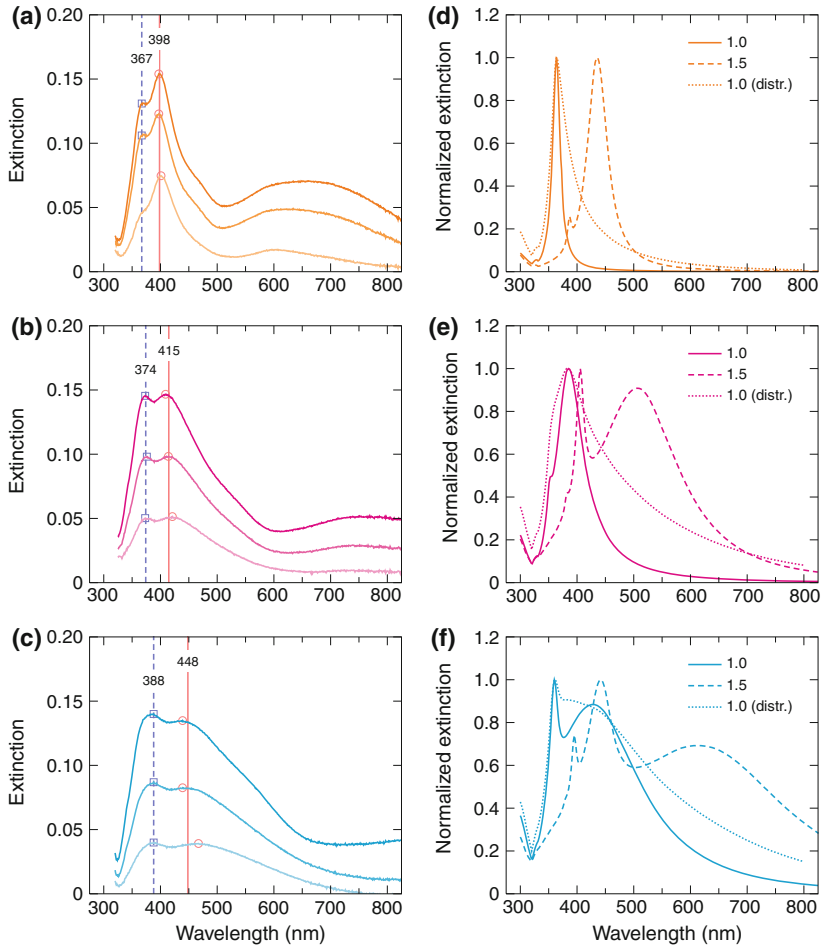

Fig. 9 Measured extinction spectra of the silver nanoparticle samples with particle sizes of approximately **a** 50, **b** 90 and **c** 130 nm and calculated theoretical extinction spectra of spherical silver particles with diameters of **d** 50, **e** 90 and **f** 130 nm. The three measured spectra in **a**–**c** correspond to different particle coverages. Theoretical spectra in **d**–**f** were calculated for single particle using refractive indices of 1.0 and 1.5 and for particle size distribution using a refractive index of 1.0 for the dielectric environment

In Fig. 10, the wavelengths of peaks 1 and 2 are presented as a function of the particle diameter together with the theoretical wavelengths of the dipolar and quadrupolar peaks for dielectric indices of 1.0–1.3. Even though the particle size dependence of the measured peaks differs from the theoretical resonances, these results strengthen the previous hypotheses, i.e. the dipolar and quadrupolar resonances clearly contribute to the measured peaks.

The broad extinction peaks in the measured spectra at longer wavelengths, approximately at 650, 750 and over 800 nm for 50, 90 and 130 nm particles, respectively, are not visible in any of the theoretical results. The extinction of these peaks as well as the ones below 400 nm becomes stronger in relation to the dipolar resonances with increasing particle coverage. This

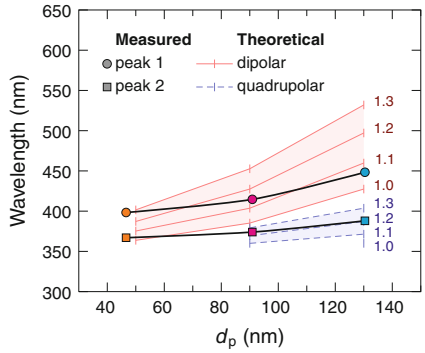

Fig. 10 The wavelengths of the extinction peaks as a function of the particle diameter. The theoretical dipolar and quadrupolar LSPR peaks for different refractive indices of the background medium were calculated from the single particle model

implies that the extinction peaks are likely related to the agglomeration of the particles during the collection.

The theoretical calculations that use the particle distributions instead of single particle show better correspondence to the measurements for the long wavelength part of the dipolar resonance peak. They also suggest that higher order resonance peaks are nearly indistinguishably merged to the dipolar resonance peaks. However, even these calculations cannot fully explain the extinction peak of the 50 nm particles below 400 nm and the peaks over 600 nm.

The theoretical model predicts the main characteristics of the prepared silver nanoparticle samples, i.e. the locations of the dipolar plasmon resonances. Discrepancies occur mostly for two reasons. First, to keep the model simple, the dielectric substrate has been neglected even though the substrate is known to significantly redshift plasmon resonances (Malinsky et al. 2001). To some extent, this effect can be accounted for by tuning the refractive index of the surrounding medium but for quantitative analysis this is insufficient. Second, the real particle distributions also contain some non-spherical particles as shown in Fig. 6. Prolate ellipsoids and elongated bar shaped particles have been shown to exhibit plasmon oscillations along distinctive particle dimensions with significantly different resonance wavelengths (Gotschy et al. 1996; Kooij and Poelsema 2006). In addition, dimers of metal nanoparticles display different plasmon resonances for incident wave polarizations parallel and perpendicular to dimer axis. The wavelengths of these resonances are red and blue-shifted, respectively, in comparison to the single particle resonance (Atay et al. 2004).

Conclusions

Plasmonic silver nanoparticle samples were prepared with aerosol techniques. The preparation technique consisted of a continuous chain of consecutive steps in the gas phase. First, agglomerated silver particles were generated in a tube furnace with an evaporation–condensation technique. The particle generation was followed by a selection of a narrow particle size distribution with a differential mobility analyzer and a sintering step in an additional furnace to obtain spherical particles. Finally, the size-selected and spherical silver nanoparticles were collected on glass substrates with an electrostatic precipitator.

The size of the silver particles calculated from the transmission electron microscope images was consistent with the measurements in the gas phase with the SMPS. This shows that the particle size control, which is important for tuning the localized surface plasmon resonance, can be very accurate when using aerosol techniques. In the present study, the size of the particles ranged within approximately 50–130 nm with a relative standard deviation close to 10 %. However, a small tail caused by doubly charged particles was also observed in the size distributions. At the expense of the collection time, it might be possible to further narrow the particle size distribution.

Since chain-like silver agglomerates were not present in the electron microscopy images and most of the particles were spherical, the sintering was effective. However, some of the larger nanoparticles, with diameters over $\sim$100 nm, were slightly elongated. The authors are not aware of any prior work that contains aerosol synthesis of spherical silver particles with diameters over 100 nm. Therefore, it is possible that the sintering step might set some limitations to the synthesis of large and completely spherical silver nanoparticles. The electron microscopy images also revealed that the particles attach to each other during the collection and form dimers, trimers, etc. on the substrate. These unwanted contacts could be eliminated by coating the nanoparticles in the gas phase with dielectric material before the collection.

The dipolar resonance of the prepared silver nanoparticle samples was tuned from 398 to 448 nm by changing the particle size in the samples. In addition to the dipolar resonance peak, other peaks were observed in the extinction spectra. The quadrupolar resonances evidently contributed to the extinction, especially with the larger particles. However, the dipolar and quadrupolar resonance peaks predicted by the simplified model were not able to explain all the characteristics of the measured extinction spectra, most likely because the theoretical model did not take into account particle dimers, elongated particles and the effects caused by the substrate.

All in all, plasmonic silver nanoparticle samples were successfully prepared. Furthermore, the possibility to control the size of the nanoparticles over a wide size range with the help of aerosol techniques improves the tunability of the localized surface plasmon resonance. Consequently, aerosol techniques offer high potential for tailoring nanoparticles for plasmonic materials.

Acknowledgments This study was supported by the Academy of Finland (136080) under the binational Finnish-Japanese joint program on 'Materials Research for Photonics, Optoelectronics, Solar Cells and Batteries'. J.M. acknowledges the support from the Graduate School of Tampere University of Technology. The authors also kindly thank Dr. Mari Honkanen from Department of Materials Science, Tampere University of Technology, for electron microscopy imaging.

References

Abràmoff MD, Magalhães PJ, Ram SJ (2004) Image processing with ImageJ. Biophotonics Int 11(7):36–41

Atay T, Song JH, Nurmikko AV (2004) Strongly interacting plasmon nanoparticle pairs: from dipole–dipole interaction to conductively coupled regime. Nano Lett 4(9):1627–1631

Beyene HT, Tichelaar FD, Verheijen MA, van de Sanden MCM, Creatore M (2011) Plasma-assisted deposition of Au/SiO_2 multi-layers as surface plasmon resonance-based red-colored coatings. Plasmonics 6(2):255–260

Bohren CF, Huffman DR (1998) Absorption and scattering of light by small particles. Wiley, New York

Catchpole KR, Polman A (2008) Plasmonic solar cells. Opt Express 16(26):21793–21800

Deppert K, Maximov I, Samuelson L, Hansson HC, Weidensohler A (1994) Sintered aerosol masks for dry-etched quantum dots. Appl Phys Lett 64(24):3293–3295

Ditlbacher H, Krenn JR, Lamprecht B, Leitner A, Aussenegg FR (2000) Spectrally coded optical data storage by metal nanoparticles. Opt Lett 25(8):563–565

Donnelly T, Doggett B, Lunney JG (2006) Pulsed laser deposition of nanostructured Ag films. Appl Surf Sci 252(13):4445–4448

Duysens LNM (1956) The flattening of the absorption spectrum of suspensions, as compared to that of solutions. Biochim Biophys Acta 19(1):1–12

Gotschy W, Vonmetz K, Leitner A, Aussenegg FR (1996) Optical dichroism of lithographically designed silver nanoparticle films. Opt Lett 21(15):1099–1101

Halas NJ (2010) Plasmonics: an emerging field fostered by Nano Letters. Nano Lett 10(10):3816–3822

Hoa XD, Kirk AG, Tabrizian M (2007) Towards integrated and sensitive surface plasmon resonance biosensors: a review of recent progress. Biosens Bioelectron 23(2):151–160

Kang M, Kim H, Han B, Suh J, Park J, Choi M (2004) Nanoparticle pattern deposition from gas phase onto charged flat surface. Microelectron Eng 71(2):229–236

Karlsson MNA, Deppert K, Karlsson LS, Magnusson MH, Malm JO, Srinivasan NS (2005) Compaction of agglomerates of aerosol nanoparticles: a compilation of experimental data. J Nanopart Res 7(1):43–49

Kelly KL, Coronado E, Zhao LL, Schatz GC (2003) The optical properties of metal nanoparticles: the influence of size, shape, and dielectric environment. J Phys Chem B 107(3):668–677

Knutson EO, Whitby KT (1975) Aerosol classification by electric mobility: apparatus, theory, and applications. J Aerosol Sci 6(6):443–451

Kooij ES, Poelsema B (2006) Shape and size effects in the optical properties of metallic nanorods. Phys Chem Chem Phys 8(28):3349–3357

Kreibig U, Vollmer M (1995) Optical properties of metal clusters. Springer, Berlin

Krinke TJ, Deppert K, Magnusson MH, Schmidt F, Fissan H (2002) Microscopic aspects of the deposition of nanoparticles from the gas phase. J Aerosol Sci 33(10):1341–1359

Ku BK, Maynard AD (2006) Generation and investigation of airborne silver nanoparticles with specific size and morphology by homogeneous nucleation, coagulation and sintering. J Aerosol Sci 37(4):452–470

Liz-Marzán LM (2004) Nanometals: formation and color. Mater Today 7(2):26–31

Loo C, Lowery A, Halas N, West J, Drezek R (2005) Immunotargeted nanoshells for integrated cancer imaging and therapy. Nano Lett 5(4):709–711

Mädler L, Roessler A, Pratsinis SE, Sahm T, Gurlo A, Barsan N, Weimar U (2006) Direct formation of highly porous gas-sensing films by in situ thermophoretic deposition of flame-made Pt/SnO_2 nanoparticles. Sens Actuators B 114(1):283–295

Mäkelä JM, Keskinen H, Forsblom T, Keskinen J (2004) Generation of metal and metal oxide nanoparticles by liquid flame spray process. J Mater Sci 39(8):2783–2788

Malinsky MD, Kelly KL, Schatz GC, van Duyne RP (2001) Nanosphere lithography: effect of substrate on the localized surface plasmon resonance spectrum of silver nanoparticles. J Phys Chem B 105(12):2343–2350

Nie S, Emory SR (1997) Probing single molecules and single nanoparticles by surface-enhanced Raman scattering. Science 275(5303):1102–1106

Scheibel HG, Porstendörfer J (1983) Generation of monodisperse Ag- and NaCl-aerosols with particle diameters between 2 and 300 nm. J Aerosol Sci 14(2):113–126

Schmidt-Ott A (1988) New approaches to in situ characterization of ultrafine agglomerates. J Aerosol Sci 19(5):553–563

Sotiriou GA, Sannomiya T, Teleki A, Krumeich F, Vörös J, Pratsinis SE (2010) Non-toxic dry-coated nanosilver for plasmonic biosensors. Adv Funct Mater 20(24):4250–4257

Sotiriou GA, Hirt AM, Lozach PY, Teleki A, Krumeich F, Pratsinis SE (2011) Hybrid, silica-coated, Janus-like plasmonic-magnetic nanoparticles. Chem Mater 23(7):1985–1992

Stepanov AL (2011) Nonlinear optical properties of implanted metal nanoparticles in various transparent matrixes: a review. Rev Adv Mater Sci 27(2):115–145

Tabrizi NS, Ullmann M, Vons VA, Lafont U, Schmidt-Ott A (2009) Generation of nanoparticles by spark discharge. J Nanopart Res 11(2):315–332

Wang SC, Flagan RC (1990) Scanning electrical mobility spectrometer. Aerosol Sci Technol 13(2):230–240

Weber AP, Friedlander SK (1997) In situ determination of the activation energy for restructuring of nanometer aerosol agglomerates. J Aerosol Sci 28(2):179–192

Xu G, Tazawa M, Jin P, Nakao S (2005) Surface plasmon resonance of sputtered Ag films: substrate and mass thickness dependence. Appl Phys A 80(7):1535–1540

Paper II

Juha Harra, Juha-Pekka Nikkanen, Mikko Aromaa, Heikki Suhonen, Mari Honkanen, Turkka Salminen, Saara Heinonen, Erkki Levänen, and Jyrki M. Mäkelä

"Gas-phase synthesis of encapsulated iron oxide–titanium dioxide composite nanoparticles by spray pyrolysis"

Powder Technology, vol. 243, pp. 46–52, 2013

doi: 10.1016/j.powtec.2013.03.027

II

Powder Technology 243 (2013) 46–52

Contents lists available at SciVerse ScienceDirect

Powder Technology

journal homepage: www.elsevier.com/locate/powtec

Gas phase synthesis of encapsulated iron oxide–titanium dioxide composite nanoparticles by spray pyrolysis

J. Harra [a,*], J.-P. Nikkanen [b], M. Aromaa [a,c], H. Suhonen [a], M. Honkanen [b], T. Salminen [d], S. Heinonen [b], E. Levänen [b], J.M. Mäkelä [a]

[a] Aerosol Physics Laboratory, Department of Physics, Tampere University of Technology, P.O. Box 692, 33101 Tampere, Finland
[b] Department of Materials Science, Tampere University of Technology, P.O. Box 589, 33101 Tampere, Finland
[c] Division of Chemistry and Chemical Engineering, California Institute of Technology, 1200 E. California Blvd., Pasadena CA 91125, USA
[d] Optoelectronics Research Centre, Tampere University of Technology, P.O. Box 692, 33101 Tampere, Finland

ARTICLE INFO

Article history:
Received 29 November 2012
Received in revised form 14 March 2013
Accepted 16 March 2013
Available online 25 March 2013

Keywords:
Aerosol synthesis
Composite nanoparticles
Iron oxide
Titanium dioxide

ABSTRACT

Composite nanoparticles are of a great interest due to the possibility of combining properties of several different materials. In this study, a spray pyrolysis process utilizing flame-synthesized nanopowder was used to generate iron oxide–titanium dioxide (γ-Fe_2O_3–TiO_2) composite nanoparticles. Iron oxide and titanium dioxide were selected because they are known to have magnetic and photocatalytic properties, respectively. First, dry γ-Fe_2O_3 nanopowder was prepared with the liquid flame spray technique. After that, the flame-synthesized nanoparticles were mixed with liquid titanium(IV) isopropoxide (TTIP) and isopropyl alcohol. This mixed-phase precursor was sprayed into a tube furnace where TTIP thermally decomposed to form solid TiO_2, encapsulating the γ-Fe_2O_3 powder particles. The synthesized nanoparticles were characterized with aerosol measurements, transmission electron microscopy, X-ray diffraction and Raman spectroscopy. The size distributions of the composite nanoparticles were broad, and the mode diameters were 80–130 nm. The particles consisted of a γ-Fe_2O_3 agglomerate that was either partially or fully encapsulated by a spherical TiO_2 particle, depending on the concentration of TTIP in the mixed-phase precursor. The flame-synthesized iron oxide powder was crystalline maghemite, whereas, spray pyrolyzed titanium dioxide had amorphous phase. The as-synthesized composite nanoparticles were calcinated to attain crystalline anatase TiO_2. The crystal structures as well as demonstrated photoactivity and magnetic response suggest that the composite nanoparticles could find use as magnetically separable photocatalyst.

1. Introduction

Combining different materials at the nanoscale provides an opportunity to engineer composite nanoparticles with enhanced or multiple unique properties, such as antibacterial, catalytic, magnetic, and plasmonic functionalities. Depending on the desired functional properties, the morphology of the composite nanoparticles can be, for example, core–shell, decorated, or Janus-like [1–3]. Therefore, controlled and flexible synthesis techniques are required.

Maghemite iron oxide crystallites (γ-Fe_2O_3) and anatase titanium dioxide (TiO_2) are known for their magnetic response and photocatalytic activity, respectively. If these two materials are combined at the nanoscale, the formed γ-Fe_2O_3–TiO_2 composite nanoparticles could serve as magnetically separable photocatalyst for water treatment and other applications [4,5]. Most syntheses of such composite nanoparticles are based on wet chemical techniques [6–9]. Gas phase synthesis techniques, however, have gained popularity because they are versatile, inexpensive, and scalable [10–12].

Both flame synthesis and different synthesis techniques utilizing high-temperature furnaces have been used for gas phase synthesis of multicomponent nanoparticles. When using flame aerosol techniques, different liquid or solution-based precursors can be mixed together [13], or the flame-synthesized particles can be coated in an enclosed reactor [14]. Furnace aerosol techniques, on the other hand, have been used to synthesize composite nanoparticles, for example, by the evaporation–condensation technique [1] or by spray pyrolysis [15]. Moreover, both flames and furnaces have been used to produce composite nanoparticles composed of iron oxide and titanium dioxide [16,17]. However, by combining the advantages of both techniques, the high production yield and the simplicity of the flame as well as the controllability of the furnace, more flexibility and versatility could be achieved in the nanoparticle synthesis process.

In this study, a synthesis technique that takes advantage of both flame and furnace techniques has been used. Fig. 1 shows a schematic presentation of an extremely simple method to synthesize composite

* Corresponding author. Tel.: +358 40 198 1180.
E-mail address: juha.harra@tut.fi (J. Harra).

0032-5910/$ – see front matter © 2013 Elsevier B.V. All rights reserved.
http://dx.doi.org/10.1016/j.powtec.2013.03.027

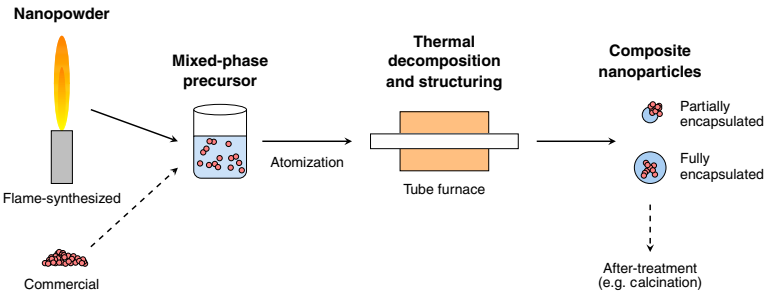

Fig. 1. A schematic presentation of gas phase synthesis of composite nanoparticles by a spray pyrolysis process that utilizes dry nanopowder.

nanoparticles with a spray pyrolysis process that utilizes flame-synthesized nanopowder. First, the dry nanopowder is mixed into a thermally decomposable liquid precursor. After that, this mixed-phase precursor is atomized into a tube furnace where the sprayed liquid droplets thermally decompose via the liquid-to-particle aerosol route to form solid nanoparticles that are bound to the surface of the powder particles. Thus, the powder particles are encapsulated by the particles formed from the liquid precursor. The morphology of the resulting composite nanoparticles depends mainly on the composition of the mixed-phase precursor. The structure of these as-synthesized composite nanoparticles can be further tailored using after-treatment techniques, such as calcination. Commercial nanopowder could be used in place of the flame-synthesized powder, but the capability to tailor the properties or to employ multicomponent nanoparticles would be lost, at least to some extent.

Somewhat similar techniques have been used to synthesize, for example, luminescent ZnO–SiO_2 [18] and photocatalytic Ag–TiO_2 nanocomposites [15]. In contrast to this study, the synthesized composite particles have been mesoporous, nearly micron-sized spheres comprised mostly from the colloid precursor nanoparticles. In this study, encapsulated γ-Fe_2O_3–TiO_2 composite nanoparticles, with diameters of approximately 100 nm were synthesized. The morphology of the nanoparticles was tailored to achieve partially and fully encapsulated composite nanoparticles. Furthermore, aerosol measurements, transmission electron microscopy, X-ray diffraction and Raman spectroscopy were used to characterize the nanoparticulate product. In addition, photoactivity and magnetic response of the synthesized composite nanoparticles were demonstrated.

2. Experimental

Dry iron oxide nanopowder was prepared with the liquid flame spray (LFS) [19] technique that has previously been used for both single component and multicomponent nanoparticle synthesis [20–22], and for producing functional coatings [23,24]. In the LFS, a liquid precursor is atomized into a turbulent high-temperature hydrogen–oxygen (H_2–O_2) flame, where the precursor evaporates and undergoes chemical reactions that lead to particle nucleation. Condensation and coagulation contribute to particle growth. A more detailed description of the LFS can be found from a previous study [25].

In this study, the precursor for the LFS contained 32 mg(Fe)/ml of ferrocene ($Fe(C_5H_5)_2$, Alfa Aesar 99%) dissolved in xylene. The precursor feed rate was set to 4 ml/min, while the O_2 and H_2 gas flows in the burner were 20 and 40 l/min, respectively. The iron oxide nanoparticles formed in the flame were collected with an electrostatic precipitator consisting of two parallel metal plates separated by a distance of approximately 60 mm. The high-voltage plate had several corona needles attached to it to generate ions that charge the particles, while the grounded plate served as a collection substrate. After the collection, the dry flame-synthesized iron oxide powder was scraped off of the collection substrate.

A scanning mobility particle sizer (SMPS) [26] consisting of a radioactive neutralizer (Krypton-85), differential mobility analyzer (TSI 3081), and a condensation particle counter (TSI 3025) was used to measure the size distribution of the flame-synthesized nanoparticles in the gas phase. The SMPS measures the so-called electrical mobility diameter, which for a spherical particle equals the diameter of the particle [27].

For the synthesis of the composite nanoparticles, a mixed-phase precursor containing flame-synthesized nanopowder, liquid titanium(IV) isopropoxide (TTIP, $Ti\{OCH(CH_3)_2\}_4$, Alfa Aesar 97%), and isopropyl alcohol (IPA) as a solvent, was prepared. In order to prevent sedimentation and further agglomeration of the nanopowder, the precursor was mixed by sonification throughout the spraying process conducted with an atomizer aerosol generator (Topas ATM 220). An inert gas stream of nitrogen with a flow rate of 0.5 l/min was used in the air-blast atomizer. In addition, the aerosol was diluted with nitrogen (1.5 l/min) before entering a quartz worktube inside a tube furnace (Carbolite MTF 12/38/400). The nitrogen flow rates were controlled with mass flow controllers. Different furnace temperatures were used, ranging from 200 to 500 °C, and the estimated residence time of the aerosol in the furnace was 7.7 s.

In the furnace, isopropyl alcohol evaporated from the precursor droplets, whereas, TTIP thermally decomposed to produce solid titanium dioxide. Particle formation by pyrolysis of TTIP has been reported to occur already at a temperature of 100 °C [28]. The synthesized two-component nanoparticles consisted of an agglomerated iron oxide powder particle encapsulated by a spherical titanium dioxide particle. By changing the composition of the mixed-phase precursor, the encapsulation state of the composite nanoparticles was varied. Two precursors, whose compositions are listed in Table 1, were used in the present study. The weight percent of iron oxide nanopowder was the same in both precursors, whereas, the weight percent of liquid TTIP was tenfold higher in precursor 2 than in precursor 1. This means that the diameter of the spherical TiO_2 particles synthesized from precursor 2 should be more than twice the diameter of the TiO_2 particles synthesized from precursor 1, assuming that the droplet size generated by the atomizer is the same when using both precursors.

The SMPS was used to measure the size distribution of the composite nanoparticles in the gas phase. In order to use electrostatic particle collection, the nanoparticles were charged in the gas phase with

Table 1
Compositions of the mixed-phase precursors used in the present study.

Precursor	γ-Fe_2O_3 (wt.%, mg/ml)	TTIP (wt.%)	IPA (wt.%)
1	0.5, 4.0	2.9	96.6
2	0.5, 4.2	29.0	70.5

a unipolar corona charger. The charged particles were then collected with an electrostatic precipitator [29] on carbon films (Agar, Carbon film 300 mesh Cu). A transmission electron microscope (TEM, Jeol JEM-2010) equipped with an energy-dispersive X-ray spectrometer (EDS, Thermo Scientific Noran Vantage, Si(Li) detector) was used for imaging and elemental analysis. The crystal structure of the synthesized nanopowder was determined with an X-ray diffractometer (XRD, Siemens Kristalloflex D500, Cu Kα radiation).

The flame-synthesized iron oxide nanopowder was characterized with Raman spectroscopy carried out with a spectrometer (Andor Shamrock 303) and a cooled CCD-camera (Newton 940P). The excitation laser was a 532 nm wavelength Cobolt Samba with a beam diameter of 0.7 mm. The sample was illuminated with a collimated laser beam in an approximately 30° angle with respect to the sample surface. The laser power was adjusted to 100 mW, and the beam was unfocused to avoid sample heating. The scattered light was collected with a microscope objective along the normal of the surface of the sample, and Rayleigh scattered light was filtered out with a Semrock Razoredge filter.

A photocatalytic measurement was performed in an aqueous solution of methylene blue (MB). Synthesized composite nanopowder (10 mg) was dispersed into a 100 ml of 0.015 mM MB solution in an open beaker and the dispersion was magnetically stirred during the whole experiment. In order to reach adsorption equilibrium, the test solution was first kept in the dark for 60 min, after which a UV lamp was turned on. Illumination was done from above with a power of 100 W/m^2 using Ledia NIS330U-M UV-Gun (peak maximum at 365 $\pm$ 5 nm). The concentration of the MB in the solution was followed by UV–VIS spectroscopy (Shimadzu UV-2501PC Spectrophotometer). At one-hour intervals a 3 ml sample was taken and subjected to centrifugation to separate the photocatalyst particles from the solution. After this, the absorbance of the MB at a wavelength of 665 nm was measured. The discoloration of the MB under a UV irradiation but without the nanopowder was also tested to confirm that the irradiation does not decompose the MB intrinsically.

3. Results and discussion

3.1. Flame-synthesized γ-Fe_2O_3 nanoparticles

A TEM image of the flame-synthesized iron oxide nanopowder is shown in Fig. 2. The particles are highly agglomerated and consist of spherical primary particles with diameters of approximately 5–20 nm. Fig. 3 shows the normalized mobility size distribution of the iron oxide agglomerates measured with the SMPS in the gas phase. The distribution was lognormal with a mode diameter of approximately 80 nm and a geometric standard deviation (GSD) of approximately 1.7.

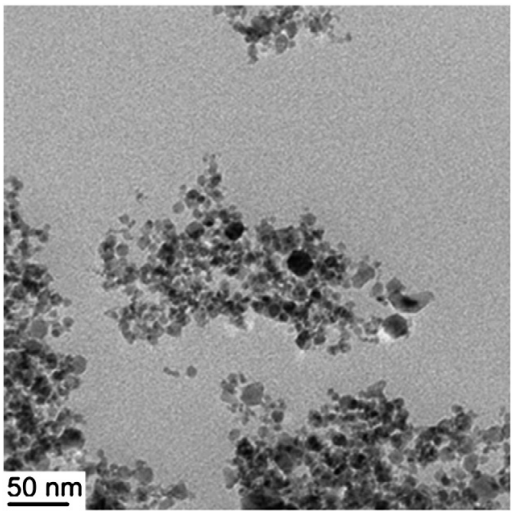

Fig. 2. A TEM image of the flame-synthesized iron oxide nanopowder.

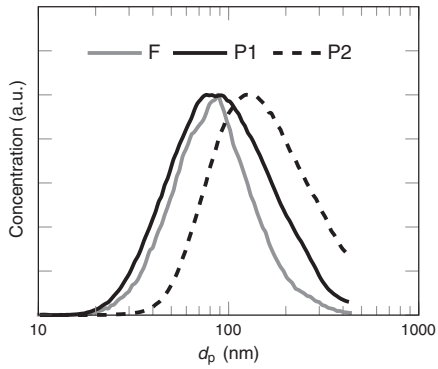

Fig. 3. Normalized mobility size distributions of the flame-synthesized iron oxide nanoparticles (F) and the γ-Fe_2O_3–TiO_2 composite nanoparticles synthesized from precursors 1 (P1) and 2 (P2). The distributions were measured in the gas phase with the SMPS. For the synthesis of the composite particles, the temperature of the furnace was set to 300 °C.

The XRD pattern of the flame-synthesized iron oxide nanopowder (Fig. 4) is typical to either maghemite (γ-Fe_2O_3) or magnetite (Fe_3O_4) crystal structure. Diffraction peaks at 2θ equal to 30.4°, 35.7°, 43.8°, 57.0°, and 63.1° can be indexed as (220), (311), (400), (511), and (440) lattice planes of maghemite (JCPDS 39-1346) or magnetite (JCPDS 19-629), respectively. The high intensity diffraction peaks of hematite (α-Fe_2O_3) that differ from those of maghemite and magnetite, located at around 33° and 49° (JCPDS 33-664), were not observed. Thus, unwanted weakly ferromagnetic hematite, which decreases the average saturation magnetization of the nanoparticulate product, was not present.

Due to the nearly identical XRD patterns of maghemite and magnetite, Raman spectroscopy can be used to distinguish the different structural phases of iron oxide [30]. Fig. 5 shows a Raman spectrum of the flame-synthesized iron oxide nanopowder displaying three broad Raman bands. According to literature [31,32], maghemite has three broad bands at around 350, 500 and 700 cm^{-1}, while magnetite has a sharper band at 668 cm^{-1} and two weaker bands at 306 and 538 cm^{-1}. The measured Raman spectrum suggests that the iron oxide nanopowder is mostly maghemite phase. Due to the broad Raman bands, a minor contribution from magnetite phase cannot be completely excluded, though, according to previous studies,

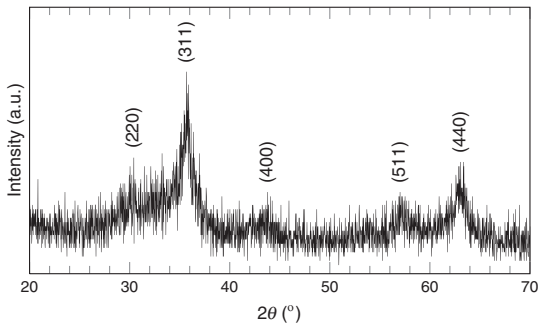

Fig. 4. An XRD pattern of the flame-synthesized iron oxide nanopowder.

II

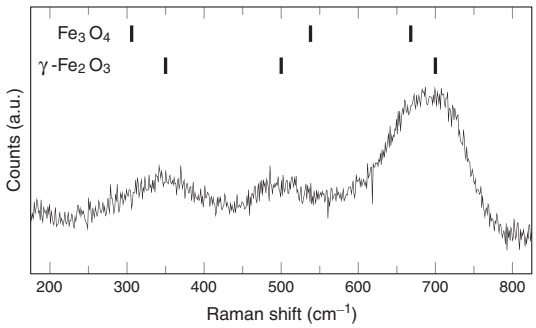

Fig. 5. A Raman spectrum of the flame-synthesized iron oxide nanopowder. The Raman bands of maghemite (γ-Fe_2O_3) and magnetite (Fe_3O_4) according to literature are shown as a reference.

flame synthesis of iron oxide nanoparticles usually leads to maghemite phase [33,34]. Hematite phase can be distinguished from the two other phases of iron oxide, for example, from a sharp and strong band at 412 cm^{-1}, which was not observed in the Raman spectrum, thus, supporting the conclusions made from the XRD measurement.

The average crystallite size was estimated by applying the Scherrer equation ($D = 0.9\lambda / B\cos\theta$) [35] to the diffraction peak (311). The result was approximately 7 nm, which corresponds to the size of the primary nanoparticles observed in the TEM image (Fig. 2). Thus, the iron oxide agglomerates consist of monocrystalline maghemite primary particles.

The magnetic properties of the flame-synthesized iron oxide nanopowder were not measured quantitatively. However, maghemite is a ferrimagnetic material, and the dry nanopowder clearly showed magnetic response in the presence of an external magnetic field, that is, the powder particles were attracted to a permanent magnet. Magnetic properties of flame-synthesized iron oxide nanoparticles are widely reported in the literature [33,34,36,37].

3.2. Partially encapsulated γ-Fe_2O_3–TiO_2 nanoparticles

Fig. 3 shows the normalized mobility size distribution of the composite γ-Fe_2O_3–TiO_2 nanoparticles synthesized from precursor 1 at a furnace temperature of 300 °C. The mode diameter of the size distribution remains practically the same, at approximately 80 nm, after the encapsulation. This suggests that the liquid TTIP fills some of the voids in the γ-Fe_2O_3 agglomerates without fully encapsulating the particles. The GSD of the size distribution was approximately 1.9, and the size distribution broadened to cover also larger particle sizes. The broadening can be explained with the broad size distribution of the liquid droplets generated by the air-blast atomizer, for which the GSD is typically greater than 1.8 [27].

Fig. 6 shows TEM images of composite nanoparticles synthesized from precursor 1 at furnace temperatures of 200, 300 and 500 °C. The composite particles in Fig. 6(a) and (b), with diameters of approximately 80 nm, consist of γ-Fe_2O_3 agglomerates that are partially encapsulated by spherical, approximately 50–70 nm diameter, TiO_2 particles. Some fully encapsulated particles, similar to the one seen in Fig. 6(c), with diameters of a few hundreds of nanometers were also detected. This is in line with the broadening of the size distribution observed in the SMPS measurements.

No visible differences were found between the particles generated at temperatures below 500 °C. At 500 °C, however, small agglomerates, as small as 10 nm, were detected in the TEM images, as seen in Fig. 6(c). These particles were identified as titanium dioxide. This suggests that at higher temperatures a fraction of the TTIP evaporates from the droplets before it decomposes thermally. TiO_2 vapor then nucleates and coagulates to form small agglomerates. Similar observation, also at a synthesis temperature of 500 °C, has been reported in an earlier study [38]. Some of these agglomerates are most likely attached on to the composite nanoparticles.

Fig. 7 shows a TEM image of a single partially encapsulated γ-Fe_2O_3–TiO_2 nanoparticle formed at a temperature of 200 °C and two EDS measurements from different sides of the composite particle, one from the agglomerated part and the other from the spherical part. The measurement from the agglomerated part showed larger iron content than that from the spherical part. For titanium the situation was reversed. The peaks of carbon, copper, and silicon in the EDS measurements were caused by the TEM grid and the equipment.

3.3. Fully encapsulated γ-Fe_2O_3–TiO_2 nanoparticles

Based on the measurements when using precursor 1, a temperature of 300 °C was used to synthesize composite nanoparticles from precursor 2 to minimize gas-to-particle conversion. Fig. 3 shows the normalized mobility size distribution of the γ-Fe_2O_3–TiO_2 nanoparticles synthesized from precursor 2. Due to the higher concentration of TTIP in the precursor, the mode diameter of the size distribution shifted to approximately 130 nm. This suggests that the γ-Fe_2O_3 agglomerates were fully encapsulated by the formed TiO_2.

Fig. 8(a) shows a TEM image of spherical TiO_2 nanoparticles whose diameters range from smaller than 100 nm to several hundreds of nanometers, consistent with the SMPS measurement of the particle size range. The mode diameter of the TiO_2 particles synthesized from precursor 2 is roughly twice that of the TiO_2 particles from precursor 1, as predicted. Moreover, the estimated original droplet size required to generate TiO_2 particles of approximately 60 and 130 nm from precursors 1 and 2, respectively, was about 500 nm, which is a quite realistic value for the used atomizer.

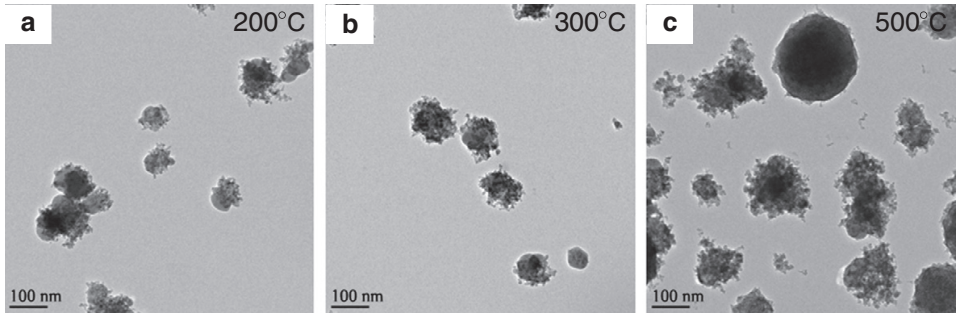

Fig. 6. TEM images of partially encapsulated γ-Fe_2O_3–TiO_2 nanoparticles synthesized from precursor 1 at furnace temperatures of (a) 200, (b) 300 and (c) 500 °C.

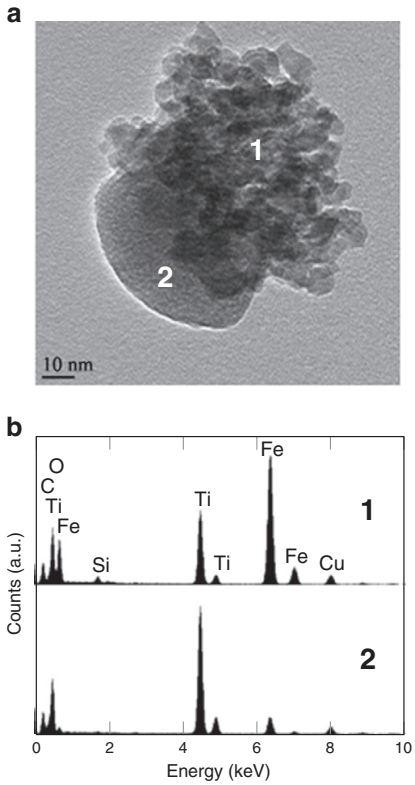

Fig. 7. (a) A TEM image of a partially encapsulated γ-Fe_2O_3–TiO_2 composite nanoparticle synthesized from precursor 1, and (b) EDS spectra from different sides of the particle. The temperature of the furnace was 200 °C.

A closer inspection of a spherical nanoparticle synthesized from precursor 2, shown in Fig. 8(b), reveals an agglomerated γ-Fe_2O_3 core inside the spherical particle. Thus, the γ-Fe_2O_3 agglomerates are fully encapsulated. Moreover, no partially encapsulated particles were detected. The EDS measurement from the fully encapsulated particle (Fig. 8(c)) confirms the presence of iron.

EDS measurements were conducted for several fully encapsulated γ-Fe_2O_3–TiO_2 composite nanoparticles with different diameters. Fig. 9 shows the mass ratio of iron to titanium as a function of particle size according to the EDS measurements. The particle sizes were determined from TEM images. According to the measurements, the particle size has no clear effect on the composition of the fully encapsulated nanoparticles, thus, the atomizer keeps the composition of the mixture fairly uniform. In addition, the average mass ratio of the measured particles is close to the theoretical ratio determined from the composition of the mixed-phase precursor. The theoretical weight percents of γ-Fe_2O_3 and TiO_2 in the composite nanoparticles were 5.6 and 94.4%, respectively.

In the EDS measurements, it was also observed that a portion of the smallest particles had no iron oxide core (triangle markers in Fig. 9). This suggests that some of the sprayed droplets did not contain a powder particle. Using a rough estimation that half of the smallest particles (< 80 nm) had no core particle, and based on the particle size distribution measured with the SMPS, approximately 90% of the particles were, nonetheless, composite particles. This constitutes clearly over 99% of the particulate mass. Moreover, magnetic separation can be used to select only the composite nanoparticles from the synthesized nanoparticulate product.

Fig. 10 shows an XRD pattern of the fully encapsulated γ-Fe_2O_3–TiO_2 composite nanopowder synthesized from precursor 2. The characterless XRD pattern of the as-synthesized particles showed no clear diffraction peaks suggesting that the phase of the TiO_2 was amorphous. This is supported by previous studies with similar synthesis temperatures [28,39]. The anatase phase transition is reported to initiate at 500 °C in a nitrogen atmosphere [38]. However, at such high temperatures small TiO_2 agglomerates were formed due to the evaporation of TTIP. The diffraction peaks of maghemite were neither observed in the XRD pattern. Due to the low concentration of iron oxide as well as the encapsulation, the detection of the iron oxide core with an XRD might be difficult.

Because amorphous titanium dioxide is almost inactive as photocatalyst [40], calcination is required to transform amorphous titanium dioxide to crystalline anatase. The calcination temperature for the crystallization of TiO_2 should be kept as low as possible in order to avoid the oxidation of the ferrimagnetic core to weakly ferromagnetic hematite [41]. Consequently, the composite nanopowder was calcinated at 400 °C for 1 h. Fig. 10 shows an XRD pattern of the calcinated composite nanopowder that is typical to anatase titanium dioxide. Diffraction peaks at 2θ equal to 25.4°, 38.0°, 48.1°, 54.1°, 55.1°, and 63.0° can be indexed as (101), (004), (200), (105), (211), and (204) lattice planes of anatase (JCPDS 84-1286), respectively. According to the Scherrer equation applied to the diffraction peak (101), the average anatase crystallite size was approximately 14 nm.

Photoactivity of the fully encapsulated and calcinated composite nanopowder synthesized from precursor 2 was measured with the discoloration of methylene blue in an aqueous solution under a UV lamp. In Fig. 11, the relative absorbance of methylene blue at a wavelength of 665 nm is presented as a function of time, showing that the synthesized composite nanopowder was photoactive. The same

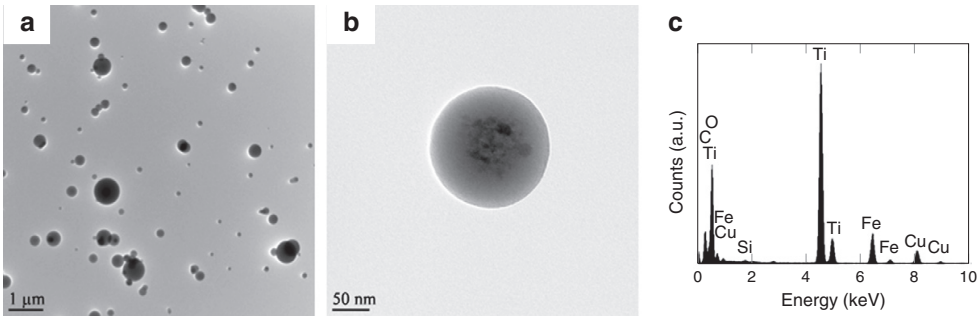

Fig. 8. (a) A TEM image of fully encapsulated γ-Fe_2O_3–TiO_2 nanoparticles synthesized from precursor 2 at a furnace temperature of 300 °C, (b) a TEM image of a single composite particle, and (c) an EDS spectrum from the particle.

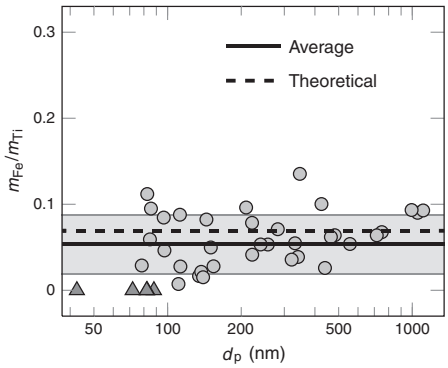

Fig. 9. The mass ratio of iron to titanium in the fully encapsulated composite nanoparticles synthesized from precursor 2 as a function of particle size according to EDS measurements. The particle sizes were determined from TEM images. The round and triangle markers correspond to particles with and without an iron oxide core, respectively, and, the shaded area corresponds to the standard deviation. The theoretical ratio is based on the composition of the mixed-phase precursor.

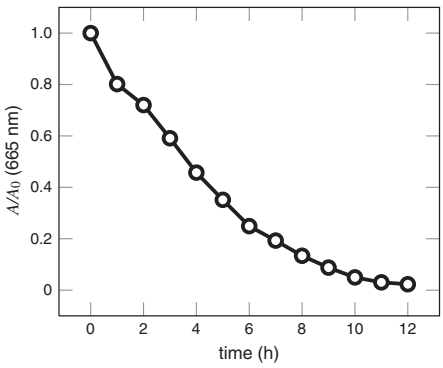

Fig. 11. Relative absorbance of methylene blue at a wavelength of 665 nm as a function of time. The fully encapsulated and calcinated composite nanopowder synthesized from precursor 2 was used as a photocatalyst.

photocatalytic measurement was also conducted to the partially encapsulated and calcinated composite nanopowder synthesized from precursor 1 at a furnace temperature of 300 °C. The measurement revealed that the partially encapsulated nanopowder was inactive as photocatalyst. The reason for this is most likely due to the morphology of the particles. As seen from the TEM images (Fig. 6), the titanium dioxide in the partially encapsulated particles is mostly buried inside the agglomerated iron oxide. Thus, the surface area of the titanium dioxide is significantly reduced by the masking iron oxide. In other words, for photocatalytic applications, the two materials in the partially encapsulated particles are in an adverse order.

Recent studies have discussed about the possible photocatalytic mechanism for iron oxide–titanium dioxide systems in which iron oxide is dissolved into the titanium dioxide lattice [42] or clustered on the surface [43]. However, these particle morphologies differ considerably from the fully encapsulated particles synthesized in the present study. In a research concerning a more similar system, titanium dioxide-coated magnetite particles, the electron interactions between the iron oxide core and titanium dioxide shell are discussed in detail [6]. All in all, different parameters, such as synthesis method, particle morphology and the amount of iron-dopant, affect whether the iron oxide increases or decreases the photoactivity of the titanium dioxide. Thus, a more detailed study is required to fully understand the photocatalytic mechanism of the encapsulated nanoparticles synthesized in the gas phase.

The magnetic properties of the calcinated composite nanopowder synthesized from precursor 2 were tested qualitatively. Fig. 12(a) shows a photograph of the nanopowder dispersed homogeneously in an aqueous suspension. In Fig. 12(b), the suspension is transparent and the powder particles are attracted to the wall of the beaker due to an external magnetic field caused by a permanent magnet. Thus, the nanoparticles showed magnetic response after the encapsulation and calcination.

Due to the lower titanium dioxide–iron oxide ratio, the partially encapsulated particles are presumably more magnetic than the fully encapsulated particles. On the other hand, the photocatalytic measurements suggested that it might be favorable to enclose the iron oxide core with titanium dioxide. Therefore, at least to some extent, the optimum magnetically separable photocatalytic nanopowder is a trade-off between the two desired functional properties.

4. Conclusions

This study described the synthesis of partially and fully encapsulated γ-Fe_2O_3–TiO_2 composite nanoparticles through a spray pyrolysis process that utilized flame-synthesized nanopowder. A mixed-phase precursor containing flame-synthesized γ-Fe_2O_3 nanoparticles, liquid TTIP, and isopropyl alcohol was mixed and then sprayed into a tube furnace. In the furnace, the alcohol evaporated from the droplets and TTIP thermally decomposed to form solid TiO_2. The resulting composite nanoparticles consisted of agglomerated γ-Fe_2O_3 particles which

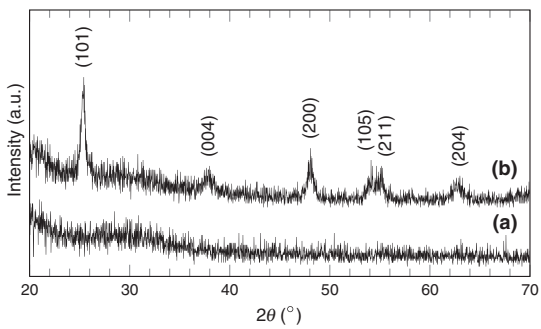

Fig. 10. An XRD pattern of (a) the as-synthesized and (b) the calcinated nanopowder synthesized from precursor 2 at 300 °C. The nanopowder was calcinated at 400 °C for 1 h.

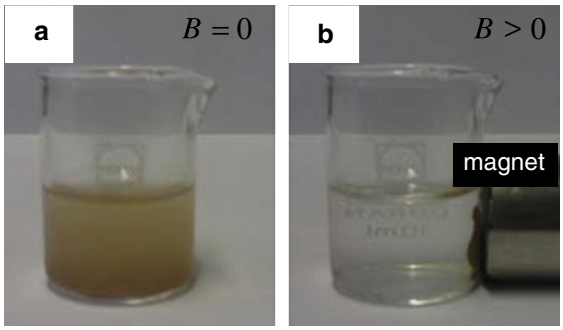

Fig. 12. Photographs of fully encapsulated and calcinated composite nanoparticles synthesized from precursor 2 in an aqueous suspension (a) before and (b) after the application of an external magnetic field.

were either partially or fully encapsulated by spherical TiO_2 particles, depending on the concentration of TTIP in the mixed-phase precursor.

The flame-synthesized iron oxide nanopowder was crystalline maghemite, which is a ferrimagnetic material. With a calcination process, the titanium dioxide in the composite nanoparticles was crystallized to anatase, which is known to have photocatalytic properties. Photoactivity and magnetic response were also demonstrated. Thus, the resulting composite nanoparticles could find use as magnetically separable photocatalyst, for example, for water treatment applications. However, further research and optimization of the magnetic and photocatalytic properties of the composite nanoparticles are still required.

The spray pyrolysis process used in this study takes advantage of dry nanopowder dispersed in a liquid precursor that is thermally decomposable. Thus, synthesis of composite nanoparticles comprised from various different materials is likely compatible with this technique. In addition, the morphology of the synthesized nanoparticles can be tailored to suit different types of applications. All in all, this extremely simple and highly versatile synthesis technique is a promising tool for engineering composite nanoparticles.

Acknowledgments

This study was supported by the Academy of Finland (decision 136080). The authors thank Prof. R. C. Flagan for his helpful comments and suggestions.

References

[1] M.N.A. Karlsson, K. Deppert, M.H. Magnusson, L.S. Karlsson, J.-O. Malm, Size- and composition-controlled Au–Ga aerosol nanoparticles, Aerosol Science and Technology 38 (2004) 948–954.
[2] A.M. Boies, P. Lei, S. Calder, S.L. Girshick, Gas-phase production of gold-decorated silica nanoparticles, Nanotechnology 22 (2011) 315603.
[3] G.A. Sotiriou, A.M. Hirt, P.-Y. Lozach, A. Teleki, F. Krumeich, S.E. Pratsinis, Hybrid, silica-coated, Janus-like plasmonic–magnetic nanoparticles, Chemistry of Materials 23 (2011) 1985–1992.
[4] S. Shylesh, V. Schünemann, W.R. Thiel, Magnetically separable nanocatalysts: bridges between homogeneous and heterogeneous catalysis, Angewandte Chemie International Edition 49 (2010) 3428–3459.
[5] V. Polshettiwar, R. Luque, A. Fihri, H. Zhu, M. Bouhrara, J.-M. Basset, Magnetically recoverable nanocatalysts, Chemical Reviews 111 (2011) 3036–3075.
[6] D. Beydoun, R. Amal, G.K.-C. Low, S. McEvoy, Novel photocatalyst: titania-coated magnetite. Activity and photodissolution, Journal of Physical Chemistry B 104 (2000) 4387–4396.
[7] S. Watson, D. Beydoun, R. Amal, Synthesis of a novel magnetic photocatalyst by direct deposition of nanosized TiO_2 crystals onto a magnetic core, Journal of Photochemistry and Photobiology A 148 (2002) 303–313.
[8] Y. Gao, B. Chen, H. Li, Y. Ma, Preparation and characterization of a magnetically separated photocatalyst and its catalytic properties, Materials Chemistry and Physics 80 (2003) 348–355.
[9] P.M. Álvarez, J. Jaramillo, F. López-Piñero, P.K. Plucinski, Preparation and characterization of magnetic TiO_2 nanoparticles and their utilization for the degradation of emerging pollutants in water, Applied Catalysis B 100 (2010) 338–345.
[10] A. Gurav, T. Kodas, T. Pluym, Y. Xiong, Aerosol processing of materials, Aerosol Science and Technology 19 (1993) 411–452.
[11] W.J. Stark, S.E. Pratsinis, Aerosol flame reactors for manufacture of nanoparticles, Powder Technology 126 (2002) 103–108.
[12] W.Y. Teoh, R. Amal, L. Mädler, Flame spray pyrolysis: an enabling technology for nanoparticles design and fabrication, Nanoscale 2 (2010) 1324–1347.
[13] H. Keskinen, J.M. Mäkelä, M. Vippola, M. Nurminen, J. Liimatainen, T. Lepistö, J. Keskinen, Generation of silver/palladium nanoparticles by liquid flame spray, Journal of Materials Research 19 (2004) 1544–1550.
[14] A. Teleki, M.C. Heine, F. Krumeich, M.K. Akhtar, S.E. Pratsinis, In situ coating of flame-made TiO_2 particles with nanothin SiO_2 films, Langmuir 24 (2008) 12553–12558.
[15] C. Zhao, A. Krall, H. Zhao, Q. Zhang, Y. Li, Ultrasonic spray pyrolysis synthesis of Ag/TiO_2 nanocomposite photocatalysts for simultaneous H_2 production and CO_2 reduction, International Journal of Hydrogen Energy 37 (2012) 9967–9976.
[16] K. Buyukhatipoglu, A. Morss Clyne, Controlled flame synthesis of αFe_2O_3 and Fe_3O_4 nanoparticles: effect of flame configuration, flame temperature, and additive loading, Journal of Nanoparticle Research 12 (2010) 1495–1508.
[17] X. Li, V.T. John, J. Zhan, G. He, J. He, L. Spinu, The synthesis of mesoporous $TiO_2/SiO_2/Fe_2O_3$ hybrid particles containing micelle-induced macropores through an aerosol based process, Langmuir 27 (2011) 6252–6259.
[18] M. Abdullah, S. Shibamoto, K. Okuyama, Synthesis of ZnO/SiO_2 nanocomposites emitting specific luminescence colors, Optical Materials 26 (2004) 95–100.
[19] J. Tikkanen, K.A. Gross, C.C. Berndt, V. Pitkänen, J. Keskinen, S. Raghu, M. Rajala, J. Karthikeyan, Characteristics of the liquid flame spray process, Surface and Coatings Technology 90 (1997) 210–216.
[20] J.M. Mäkelä, H. Keskinen, T. Forsblom, J. Keskinen, Generation of metal and metal oxide nanoparticles by liquid flame spray process, Journal of Materials Science 39 (2004) 2783–2788.
[21] H. Keskinen, J.M. Mäkelä, M. Aromaa, J. Ristimäki, T. Kanerva, E. Levänen, T. Mäntylä, J. Keskinen, Effect of silver addition on the formation and deposition of titania nanoparticles produced by liquid flame spray, Journal of Nanoparticle Research 9 (2007) 569–588.
[22] J.-P. Nikkanen, H. Keskinen, M. Aromaa, M. Järn, T. Kanerva, E. Levänen, J.M. Mäkelä, T. Mäntylä, Iron oxide doped alumina–zirconia nanoparticle synthesis by liquid flame spray from metal organic precursors, Research Letters in Nanotechnology 2008 (2008) 516478.
[23] H. Keskinen, J.M. Mäkelä, M. Aromaa, J. Keskinen, S. Areva, C.V. Teixeira, J.B. Rosenholm, V. Pore, M. Ritala, M. Leskelä, M. Raulio, M.S. Salkinoja-Salonen, E. Levänen, T. Mäntylä, Titania and titania–silver nanoparticle deposits made by Liquid Flame Spray and their functionality as photocatalyst for organic- and biofilm removal, Catalysis Letters 111 (2006) 127–132.
[24] M. Aromaa, A. Arffman, H. Suhonen, J. Haapanen, J. Keskinen, M. Honkanen, J.-P. Nikkanen, E. Levänen, M.E. Messing, K. Deppert, H. Teisala, M. Tuominen, J. Kuusipalo, M. Stepien, J.J. Saarinen, M. Toivakka, J.M. Mäkelä, Atmospheric synthesis of superhydrophobic TiO_2 nanoparticle deposits in a single step using Liquid Flame Spray, Journal of Aerosol Science 52 (2012) 57–68.
[25] M. Aromaa, H. Keskinen, J.M. Mäkelä, The effect of process parameters on the Liquid Flame Spray generated titania nanoparticles, Biomolecular Engineering 24 (2007) 543–548.
[26] S.C. Wang, R.C. Flagan, Scanning electrical mobility spectrometer, Aerosol Science and Technology 13 (1990) 230–240.
[27] P. Kulkarni, P.A. Baron, K. Willeke (Eds.), Aerosol Measurement: Principles, Techniques, and Applications, John Wiley & Sons, Inc., 2011
[28] P. Moravec, J. Smolík, V.V. Levdansky, Preparation of TiO_2 fine particles by thermal decomposition of titanium tetraisopropoxide vapor, Journal of Materials Science Letters 20 (2001) 2033–2037.
[29] J. Harra, J. Mäkitalo, R. Siikanen, M. Virkki, G. Genty, T. Kobayashi, M. Kauranen, J.M. Mäkelä, Size-controlled aerosol synthesis of silver nanoparticles for plasmonic materials, Journal of Nanoparticle Research 14 (2012) 870.
[30] N. Pinna, S. Grancharov, P. Beato, P. Bonville, M. Antonietti, M. Niederberger, Magnetite nanocrystals: nonaqueous synthesis, characterization, and solubility, Chemistry of Materials 17 (2005) 3044–3049.
[31] D.L.A. de Faria, S.V. Silva, M.T. de Oliveira, Raman microspectroscopy of some iron oxides and oxyhydroxides, Journal of Raman Spectroscopy 28 (1997) 873–878.
[32] O.N. Shebanova, P. Lazor, Raman spectroscopic study of magnetite ($FeFe_2O_4$): a new assignment for the vibrational spectrum, Journal of Solid State Chemistry 174 (2003) 424–430.
[33] S. Grimm, M. Schultz, S. Barth, R. Müller, Flame pyrolysis—a preparation route for ultrafine pure γ-Fe_2O_3 powders and the control of their particle size and properties, Journal of Materials Science 32 (1997) 1083–1092.
[34] R. Strobel, S.E. Pratsinis, Direct synthesis of maghemite, magnetite and wustite nanoparticles by flame spray pyrolysis, Advanced Powder Technology 20 (2009) 190–194.
[35] B.D. Cullity, Elements of X-ray Diffraction, Addison-Wesley Publishing Company, Inc., 1967
[36] D. Li, W.Y. Teoh, C. Selomulya, R.C. Woodward, R. Amal, B. Rosche, Flame-sprayed superparamagnetic bare and silica-coated maghemite nanoparticles: synthesis, characterization, and protein adsorption–desorption, Chemistry of Materials 18 (2006) 6403–6413.
[37] B.M. Kumfer, K. Shinoda, B. Jeyadevan, I.M. Kennedy, Gas-phase flame synthesis and properties of magnetic iron oxide nanoparticles with reduced oxidation state, Journal of Aerosol Science 41 (2010) 257–265.
[38] P.P. Ahonen, E.I. Kauppinen, J.C. Joubert, J.L. Deschanvres, G.G. Van Tendeloo, Preparation of nanocrystalline titania powder via aerosol pyrolysis of titanium tetrabutoxide, Journal of Materials Research 14 (1999) 3938–3948.
[39] J.G. Choi, K.Y. Park, Effect of reaction atmosphere on particle morphology of TiO_2 produced by thermal decomposition of titanium tetraisopropoxide, Journal of Nanoparticle Research 8 (2006) 269–278.
[40] B. Ohtani, Y. Ogawa, S. Nishimoto, Photocatalytic activity of amorphous–anatase mixture of titanium(IV) oxide particles suspended in aqueous solutions, Journal of Physical Chemistry B 101 (1997) 3746–3752.
[41] D. Beydoun, R. Amal, Implications of heat treatment on the properties of a magnetic iron oxide–titanium dioxide photocatalyst, Materials Science and Engineering B 94 (2002) 71–81.
[42] T.K. Ghorai, M. Chakraborty, P. Pramanik, Photocatalytic performance of nanophotocatalyst from TiO_2 and Fe_2O_3 by mechanochemical synthesis, Journal of Alloys and Compounds 509 (2011) 8158–8164.
[43] Q. Sun, W. Leng, Z. Li, Y. Xu, Effect of surface Fe_2O_3 clusters on the photocatalytic activity of TiO_2 for phenol degradation in water, Journal of Hazardous Materials 229–230 (2012) 224–232.

II

Paper III

Juha Harra, Paxton Juuti, Janne Haapanen, Miika Sorvali, Eleftheria Roumeli, Mari Honkanen, Minnamari Vippola, Jaakko Yli-Ojanperä, and Jyrki M. Mäkelä

"Coating of silica and titania aerosol nanoparticles by silver vapor condensation"

Aerosol Science and Technology, vol. 49, no. 9, pp. 767 – 776, 2015

doi: 10.1080/02786826.2015.1072263

III

Aerosol Science and Technology, 49:767–776, 2015

ISSN: 0278-6826 print / 1521-7388 online
DOI: 10.1080/02786826.2015.1072263

Coating of Silica and Titania Aerosol Nanoparticles by Silver Vapor Condensation

Juha Harra,[1] Paxton Juuti,[1] Janne Haapanen,[1] Miika Sorvali,[1] Eleftheria Roumeli,[1] Mari Honkanen,[2] Minnamari Vippola,[2] Jaakko Yli-Ojanperä,[1] and Jyrki M. Mäkelä[1]
[1]*Department of Physics, Tampere University of Technology, Tampere, Finland*
[2]*Department of Materials Science, Tampere University of Technology, Tampere, Finland*

III

Silica and titania aerosol nanoparticles are coated with silver through a physical coating process. The silver is evaporated in a tubular furnace flow system and condensed on the ceramic carrier particles with diameters of approximately 100 nm. The temperature gradient in the furnace system is optimized in order to avoid homogeneous nucleation of the silver. The generated ceramic–silver composite nanoparticles are characterized with aerosol measurements and analytical transmission electron microscopy. Two completely different particle morphologies are clearly observed, silver-decoration and composite doublet, with amorphous silica and crystalline rutile titania as the carrier particles, respectively. The former morphology consists of multiple silver nanodots with diameters of 1–10 nm, while in the latter morphology the silver had formed a larger structure with a size comparable to that of the carrier particle. Different shapes are observed in these larger silver structures, such as triangular, rodlike, and hexagonal. Differences in the silver particle migration on the surface of the silica and titania particles is proposed to be the key factor resulting into the two distinct particle morphologies.

1. INTRODUCTION

Ceramic nanoparticles (e.g., SiO_2, TiO_2, and Al_2O_3) coated via aerosol methods with noble metals (Pd, Ag, Pt, and Au) have been utilized as gas sensors (Mädler et al. 2006), catalysts (Height et al. 2006; Keskinen et al. 2007; Faust et al. 2013), antibacterials (Sotiriou et al. 2011), as well as in optical applications, such as plasmonics (Boies et al. 2011; Zdanowicz et al. 2013) and nonlinear optics (Zdanowicz et al. 2013, 2014). Both chemical and physical routes to the coating of nanoparticles in the aerosol phase have been demonstrated. Chemical coating routes, such as flame synthesis methods (Keskinen et al. 2007; Teoh et al. 2010) and chemical vapor deposition (Binder et al. 2007), are known for the high production rate and the precise control of the coating parameters, respectively. However, finding the suitable precursors for the desired chemical processes can be challenging. Physical coating routes usually rely on the coagulation of smaller metal particles or clusters and larger carrier particles (Boies et al. 2011; Pfeiffer et al. 2015). Even though the particle coagulation can be enhanced with the electrical attraction between oppositely charged metal and carrier particles (Sigmund et al. 2014), the amount of the metal coating on an individual carrier particle has been usually low.

Condensation of vaporized material onto a seed particle is a physical coating route exploited extensively, for example, in aerosol measurement instruments and reference aerosol generation (Yli-Ojanperä et al. 2010). In these applications, it is more practical to use liquid as a "coating" material. Due to the low vapor pressures of noble metals, high temperatures are required for their substantial vaporization. Sparks are an efficient method to vaporize metals for nanoparticle production (Pfeiffer et al. 2014). However, the huge temperature drop after the spark leads quickly to particle formation through homogeneous nucleation. More controlled temperature gradients can be achieved in systems where the complete gas flow is heated within a tubular reactor. Backman et al. (2004) used such a reactor in their evaporation/condensation system for coating titania agglomerates with silver, resulting in nanometer-sized silver particles on the surface of the carrier particles. Much higher amounts of condensated material was achieved by Zihlmann et al. (2014), who grew gold seed particles with silver. In their experiments, the produced particles were spherical, although not core–shell, as the two materials were evenly distributed in the particles, forming a metal alloy.

Here, we study the coating process of two ceramic materials, amorphous silica and crystalline rutile titania, via silver vapor condensation. The size of the coated particles is around 100 nm. The produced composite particles are characterized using aerosol instruments and analytical transmission electron microscope. In the case of the silica carrier particles, we find that the silver forms separate nanodots (a.k.a. decoration). This is probably the most common morphology obtained in

Received 6 May 2015; accepted 4 July 2015.
Address correspondence to Juha Harra, Department of Physics, Tampere University of Technology, Korkeakoulunkatu 3, 33720 Tampere, Finland. E-mail: juha.harra@tut.fi

the different coating processes for aerosol nanoparticles (Backman et al. 2004; Binder et al. 2007; Boies et al. 2011; Zdanowicz et al. 2013; Sigmund et al. 2014; Pfeiffer et al. 2015). However, the silver behaves quite differently on the crystalline titania, forming larger particles and resulting into a morphology that could be described as a composite doublet.

2. EXPERIMENTAL METHODS

In this study, two separate aerosol synthesis processes were combined in order to produce ceramic–silver composite nanoparticles. In the first process, ceramic aerosol nanoparticles were produced with a flame method and collected into a nanopowder. The second process involved the spraying of the previously produced nanopowder into a closed gas flow, followed by the sintering of the sprayed ceramic nanoparticles, and finally the coating of these particles with silver. It should be noted that as both of the used synthesis processes take place in the aerosol phase, it might be possible to combine them into one continuous aerosol process. However, as the current research concentrates on studying the coating process of the ceramic nanoparticles, it was more convenient to utilize two separate aerosol synthesis processes.

2.1. Generation of the Silica and Titania Carrier Particles

The silica and titania carrier particles were generated from nanopowders of the said materials. The nanopowders were produced with a flame synthesis method called the Liquid Flame Spray (LFS) (Tikkanen et al. 1997). In the LFS, a precursor dissolved in a liquid solution is atomized into a turbulent H_2/O_2 flame. Due to the high temperature, the precursor evaporates and undergoes chemical reactions that lead to a particle nucleation. The formed particles grow through condensation from the vapor phase and coagulation with other particles, usually leading to a highly agglomerated end product (Eggersdorfer and Pratsinis 2014). A more detailed description of the LFS can be found from the previous studies (Aromaa et al. 2007; Haapanen et al. 2015). In this study, tetraethyl orthosilicate (TEOS, Alfa Aesar 98%) and titanium isopropoxide (TTIP, Alfa Aesar 97%) dissolved in isopropyl alcohol (50 mg(Si)/mL and 50 mg(Ti)/mL) were used as precursors for silica and titania, respectively. Furthermore, the precursor feed rates were 4.2 and 6.0 mL/min and the H_2/O_2 flow rates in the burner were 30/30 and 40/20 L/min for the generation of the silica and titania nanoparticles, respectively. The LFS-generated particles were collected into a nanopowder with an electrostatic precipitator (Harra et al. 2013).

A schematic illustration of the experimental setup used for the continuous production of the ceramic–silver composite particles is shown in Figure 1. The setup can be divided into three sections: (1) generation of the carrier particles, (2) coating of the carrier particles with silver, and (3) aerosol measurement and sampling. In Section 1, aqueous dispersion of LFS-generated silica (3 mg/mL) and titania (6 mg/mL) nanopowders were aerosolized with an atomizer aerosol generator (Topas ATM 220) using nitrogen as a carrier gas. The sprayed aerosol was diluted with nitrogen in order to avoid water condensation on the tube walls, resulting into a relative humidity of approximately 90% at the room temperature. In order to study the coating process, the agglomerated particles were sintered in a tube furnace (Carbolite TZF 15/50/610, alumina tube, inner diameter 25 mm) at a temperature of 1500 °C, while the flow rate was 1.5 L/min. The water was removed from the gas phase with a diffusion drier only after the furnace, as the water vapor is known to enhance the sintering process (Goertz et al. 2011). A differential mobility analyzer (DMA, Vienna-type) was used as an option to select certain particle sizes and also to reduce the particle number concentration. The DMA was preceded by a radioactive neutralizer

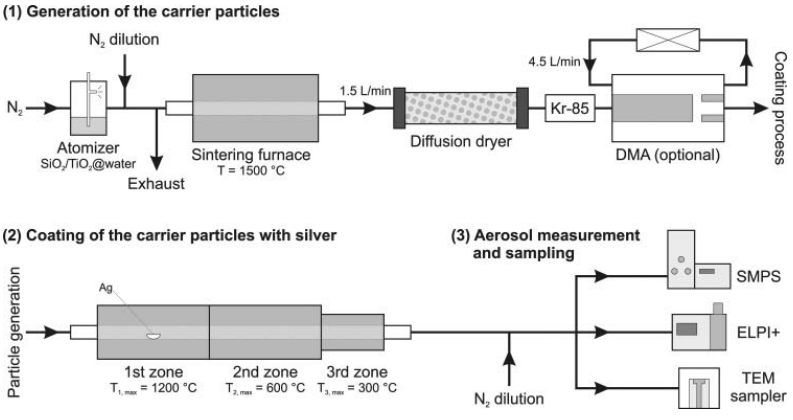

FIG. 1. A schematic illustration of the experimental setup divided into three sections.

(Krypton-85), and the aerosol/sheath flow rate in the DMA was 1.5/4.5 L/min.

The particle number size distributions were measured with a scanning mobility particle sizer (SMPS) depicted in Section 3 (Figure 1). The SMPS composed of a radioactive neutralizer (Krypton-85), a DMA (TSI 3081), and a condensation particle counter (CPC, TSI 3025). The total condensation sink (CS) of the carrier particles was estimated relatively using an electrical low pressure impactor (ELPI+) (Keskinen et al. 1992; Järvinen et al. 2014), as the total current measured by the ELPI is directly proportional to the total CS (Kuuluvainen et al. 2010; Järvinen et al. 2015). Table 1 lists the parameters of the carrier particles used in this study. Examples of the particle number size distributions are shown in Figure 2. The distributions before the DMA were broad with geometric standard deviations near 1.6. Due to this, the doubly charged particles form a large fraction of the size distributions after the DMA. We take advantage of this, and analyze both particle sizes in the bimodal distribution by fitting log-normal distributions to the measurements.

2.2. Coating of the Carrier Particles with Silver

The coating section of the experimental setup (Section 2 in Figure 1) consisted of an alumina tube (inner diameter 25 mm) heated inside two consecutive tube furnaces (Carbolite MTF 12/38/400), both with a heated length of 400 mm. A heater band with a length of approximately 300 mm was added as a third heating zone. Three pieces of bulk silver with diameters of approximately 5 mm were placed in a crucible in the middle of the first heating zone (temperature T_1). The nitrogen flow rate through the coating section was 1.5 L/min, and the maximum silver evaporation temperature was 1200 °C.

The amount of the evaporated silver in different temperatures was estimated by measuring the total mass of the silver particles formed through homogeneous nucleation with the SMPS directly after the first furnace. This gives the lower limit

Table 1
The parameters of the generated carrier particles

Material	DMA	GMD (nm)	N (cm^{-3})	CS (a.u.)
SiO_2	Yes	96	2.7×10^4	1.0
		149	1.9×10^4	
SiO_2	No	150	8.2×10^5	35
TiO_2	Yes	64	4.0×10^4	1.3
		93	2.0×10^4	
TiO_2	Yes	123	7.7×10^4	3.8
		177	2.2×10^4	
TiO_2	No	107	2.1×10^6	55

The geometric mean diameter (GMD) and particle number concentration (N) of both particle modes after the differential mobility analyzer (DMA) are presented. The presented total condensation sink (CS) values are the normalized total currents measured by the ELPI+.

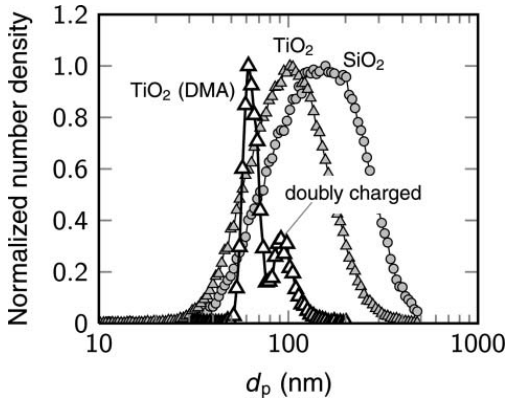

FIG. 2. Examples of the number size distributions of the carrier particles before and after the DMA.

to the actual evaporated mass. The upper limit is obtained by assuming that the gas is saturated with silver. Furthermore, values calculated from the evaporation rates of silver in a gas flow (Lu and Zhu 2007) provide intermediate estimations. The functional form of the vapor pressure of silver (Alcock et al. 1984) was fitted to the measured and calculated values. The estimations of the total mass concentration of silver as a function of the evaporation temperature are presented in Figure 3a.

In order to avoid homogeneous nucleation of silver, the temperature gradient inside the heating zones was optimized. To find the correct temperature gradient, we measured the total mass of the generated silver particles with the SMPS as a function of the temperature of the second heating zone (T_2), while the evaporation temperature in the first heating zone was set to 1200 °C. The results are shown in Figure 3b. With lower temperatures, the temperature gradient is steep enough for the particle nucleation to occur. On the other hand, higher temperatures shift the location of the particle nucleation after the second heating zone. At intermediate temperatures of approximately 500–800 °C, no particles were detected, even with the CPC alone (cut point 3 nm). Thus, the homogeneous nucleation is minimized and the silver vapor condenses on the tube walls. The temperature of the second and third (T_3) heating zones were chosen to be 600 and 300 °C, respectively, for further experiments.

In the presence of the carrier particles, some of the evaporated silver forms coating on the carrier particles through heterogeneous nucleation and vapor condensation. The effect of the coating to the mobility size of the particles was measured with the SMPS. In order to analyze the particles with an analytical transmission electron microscope (TEM, Jeol JEM-2010), they were charged with a corona charger (Arffman et al. 2014) and deposited on carbon coated copper grids using an electrostatic precipitator (Krinke et al. 2002; Harra et al. 2012). Morphology and crystal structure studies of the

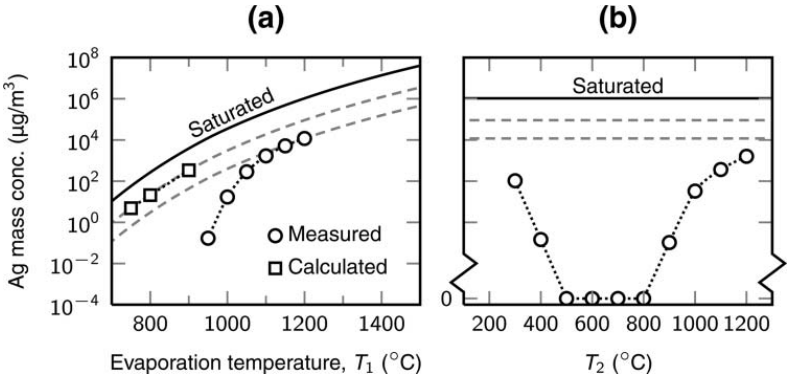

FIG. 3. (a) The total mass concentration of silver as a function of the evaporation temperature (T_1) measured with the SMPS directly after the first heating zone. The calculated values are derived from the evaporation rates determined by Lu and Zhu (2007). (b) The total mass concentration of silver as a function of the temperature of the second heating zone (T_2) measured with the SMPS. The evaporation temperature was $T_1 = 1200\,^{\circ}\mathrm{C}$. At intermediate temperatures (500–800 °C), no particles were detected with the CPC. In both figures, the solid line corresponds to a full saturation concentration at the evaporation temperature, and the dashed gray lines represent fits of the functional form of the silver vapor pressure to the measured and calculated values.

particles were done by TEM imaging and selected area electron diffraction (SAED), respectively. In addition, elemental analysis of the particles was performed with an energy-dispersive X-ray spectrometer (EDS, Thermo Scientific Noran Vantage, Si(Li) detector). The weight percents of different elements were determined by the conventional qualitative and quantitative EDS analysis procedures using Noran Vantage Spectral Display software. The reference library used in the crystal structure analyses was the database (PDF+ 2014) from International Centre for Diffraction Data (ICDD).

3. RESULTS AND DISCUSSION

3.1. Particle Sizes Measured in the Aerosol

The mobility size of the particles selected with the DMA was measured with the SMPS at different evaporation temperatures. The temperatures of the second and the third heating zones were the same as the evaporation temperature until at 600 and 300 °C, respectively, after which only the evaporation temperature was increased. The particle sizes were determined from the measurements using bimodal log-normal fits. In the case of the largest titania particles, only the first mode was properly resolved. Figure 4 shows the mobility diameter of the size-selected silica and titania particles as a function of the silver evaporation temperature. With both particle materials, the mobility diameter stays constant, until, after the melting point of bulk silver, the particle diameter begins to rapidly increase. With all of the studied particle sizes, at the maximum evaporation temperature of 1200 °C, the diameter of the silica and titania particles had increased approximately 10 and 20 nm, respectively.

The ELPI+ was also used to measure the particle number size distributions. However, even though greased impaction substrates were used, particle bounce and subsequent charge transfer interfered with the measurements (Kuuluvainen et al. 2013; Arffman et al. 2015). Interestingly, at least the charge transfer ended when the particle size began to increase, presumably, due to the formation of the conductive metal on top of the dielectric particle material. Although, the size distributions measured with the ELPI+ were unreliable, the total measured current could be used as an estimation of the total CS of the aerosol particles.

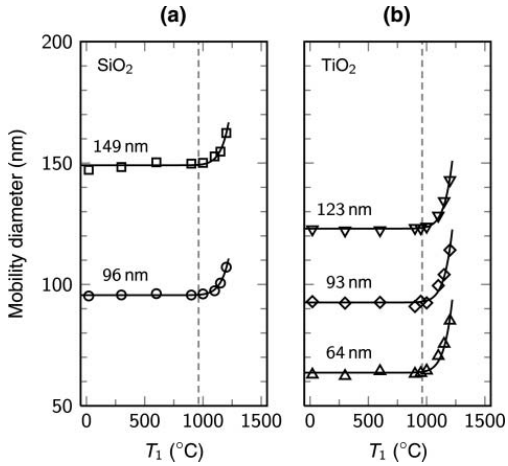

FIG. 4. The mobility diameter of the size-selected (a) silica and (b) titania particles as a function of the silver evaporation temperature (T_1). The temperatures of the second and third heating zones were the same as the evaporation temperature until $T_2 = 600$ and $T_3 = 300\,^{\circ}\mathrm{C}$, after which only the evaporation temperature was increased. The dashed lines correspond to the melting point of bulk silver (962 °C).

3.2. Particle Morphologies Observed with Electron Microscopy

The TEM micrographs shown in Figure 5a reveal that the silica particles were quite compact but not fully sintered to spheres after the sintering step. Obviously, the residence time in the furnace (approximately 2 s) was insufficient for complete sintering. Similar observations on the sintering behavior of pure silica have been reported in the literature (Binder et al. 2010; Goertz et al. 2011). The titania particles in Figure 5b, on the other hand, were sintered to a faceted form, as expected (Ahonen et al. 2001; Binder et al. 2010). Based on the previous studies, the LFS-generated titania nanopowder is mostly crystalline anatase (Aromaa et al. 2007, 2012). However, after the sintering step at 1500 °C, we expect that the phase of the titania changes to rutile (Ahonen et al. 2001). In order to confirm the phase of the titania carrier particles, the corresponding electron diffraction (ED) patterns were analyzed (Figure 6) and the distance between the adjacent lattice fringes from the TEM micrographs was measured. The ED patterns indicated the crystal structure of rutile with main crystal orientations [001] and [111]. In addition, a lattice spacing of 0.324 nm was obtained, which can be assigned to the interplanar distance of rutile phase [110] plane.

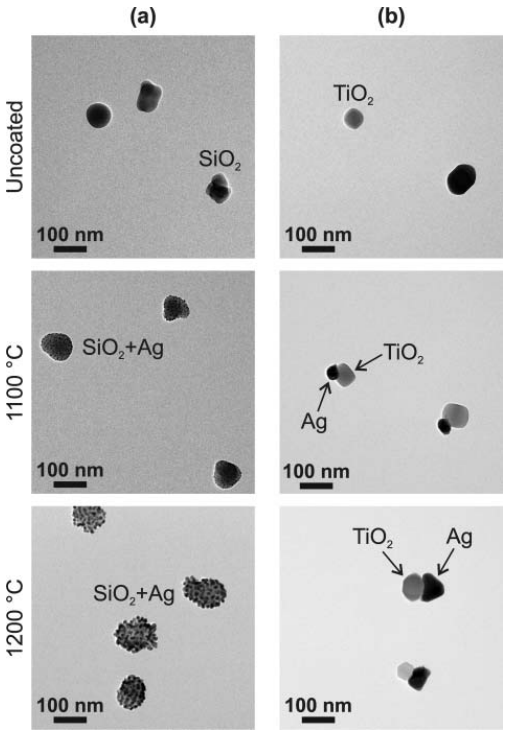

FIG. 5. TEM micrographs of (a) silica and (b) titania particles before and after the coating with silver at evaporation temperatures (T_1) of 1100 and 1200 °C. Silver-decoration and composite doublets were formed with silica and titania carrier particles, respectively.

At silver evaporation temperatures of 1100 and 1200 °C (Figure 5), we see two totally different particle morphologies. In the case of the silica, the silver forms nanodots, referred here as decoration, that cover the silica particles uniformly. The size of the dots increases with the evaporation temperature. However, with titania, the silver forms a single larger particle whose size increases with the evaporation temperature, leading to a composite doublet morphology. No individual silver particles were detected with the TEM.

The different particle morphologies for silica and titania are consistent with the SMPS mobility size measurements. For silica at 1200 °C, the evenly distributed silver particles have a diameter of approximately 10 nm, and thus the mobility size increases less than 20 nm. For doublets of spheres, the mobility size is about 1.3 times the size of the individual spheres (Kasper 1983). In the case of the 60 nm titania particles, the silver particles have about the same size, and thus the mobility diameter increases approximately 20 nm.

TEM micrographs at a higher magnification from approximately 90 nm silica and titania particles coated at different silver evaporation temperatures are shown in Figure 6. Before coating, the particle surfaces are clean, but already at 900 °C we observe extremely small (<1 nm) silver nanodots on top of both carrier particle materials. With silica, as the size of the spherical decorations increases with the temperature, their number density on the particle decreases. On the titania particles at 1000 °C, larger silver structures have been formed. As the evaporation temperature increases, the size of these structures increases as well. However, we still see some smaller silver dots on the titania particles.

Titania particles smaller than 120 nm contained only one larger silver particle. However, multiple silver structures were found in larger carrier particles. Figure 7a shows a nearly 400 nm titania particle containing several silver structures, whereas an approximately 160 nm titania particle with a grain boundary in the middle contains two silver particles on each side as seen in Figure 7b. The silver structures observed on the titania particles had a variety of different shapes, including triangular, rodlike, and hexagonal.

The ED pattern in Figure 6 for an uncoated silica particle shows diffuse rings, characteristic to an amorphous material. At the evaporation temperature of 1200 °C, the ED pattern of the silica particle decorated with approximately 10 nm silver particles shows crystalline rings, marked with arrows, characteristic to nanocrystalline material. As the size of the silver decorations decrease with lower evaporation temperatures, the rings can be expected to become more diffuse. Furthermore, as these rings are similar to the ones caused by the amorphous silica, we were unable to detect the effect of the silver decorations on the ED patterns at the lower evaporation temperatures. For uncoated titania particles, we observed reflections caused by the crystalline rutile structure with main crystal orientations

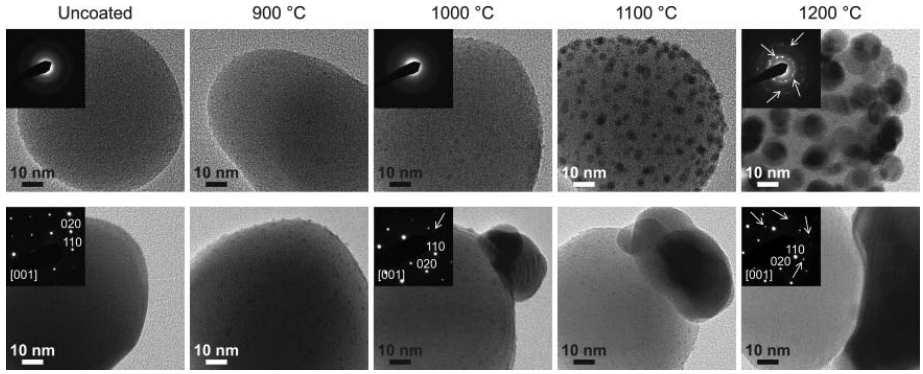

FIG. 6. TEM micrographs of approximately 90 nm silica (top row) and titania (bottom row) particles coated with silver at different evaporation temperatures (T_1). The insets show typical electron diffraction (ED) patterns from the particles at the corresponding temperatures. The ED patterns indicate amorphous silica and crystalline titania particles. At $T_1 = 1200\,^{\circ}\mathrm{C}$, reflections (marked with arrows) from nanocrystalline silver on silica, and starting at $T_1 = 1000\,^{\circ}\mathrm{C}$, reflections from crystalline silver structures on titania particles can be observed.

[001] and [111] at every evaporation temperature. Thus, no additional crystal phase shift occurs with titania in the coating section. At the evaporation temperature of 1000 °C, extra reflections caused by the silver were detected. The number of these reflections increased with the evaporation temperature, as the size of the silver structure increased.

3.3. Characterization of the Silver Coating Using Elemental Analysis

An EDS analysis was performed on several individual particles in order to determine the weight percents of the different elements in the particles. Only elemental silver (Ag) and silicon/titanium (Si/Ti) were included in the analysis. From the obtained weight percents, we could calculate the mass of silver on an individual carrier particle by assuming that each Si/Ti atom is bonded to two oxygen atoms, i.e., we have pure silica/titania (SiO_2/TiO_2). Also, bulk densities for the substances, 2.2, 4.23, and 10.49 g/cm^3 for silica, titania, and silver, respectively, were assumed. For each obtained value, approximately five measurements from different individual particles were averaged.

Figure 8a shows the number density of the decorative silver dots on the silica particles as a function of the diameter of the silver decorations. The average dot size was determined from the TEM micrographs and the number density was calculated using the mass of silver obtained from the EDS analysis and the dot sizes. Interestingly, all the calculated values from the silica particles with different sizes, as well as with completely different total CSs (gray markers), are on the same line, with the number density approximately inversely proportional to the dot size. The size of the silver dots varies between approximately 1 and 10 nm. If we extrapolate the line to larger dot sizes, eventually maximum packing density is reached, that is, all the silver spheres are in contact with their neighboring particles. Based on this study, we can only speculate whether a silver shell structure would be formed on the silica cores. In order to reach the maximum packing density, higher evaporation temperatures are required. Based on the available data, we estimate that this critical temperature for the size-selected silica particles is approximately 1250 °C, resulting into a silver shell with a thickness of approximately 12 nm.

For the titania particles, we calculated the mass equivalent size of the formed silver particles from the EDS measurements. The calculated size of the silver particles was consistent with the TEM micrographs. Figure 8b shows this diameter as a function of the evaporation temperature for titania carrier particles with different diameters and total CSs. Besides the evaporation temperature, the size of the silver particles increases with larger titania particles and lower total CS. This shows that the particle sizes of both

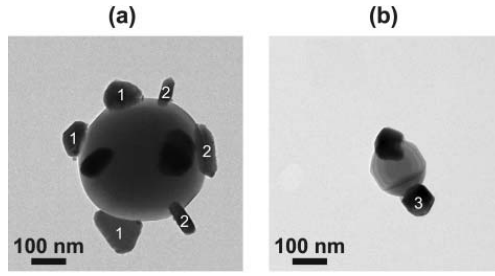

FIG. 7. A TEM micrograph of (a) a large titania particle containing several silver structures and (b) a titania particle with a grain boundary containing two silver structures. Different shaped silver structures were observed, including (1) triangular, (2) rodlike, and (3) hexagonal. The evaporation temperature was $T_1 = 1200\,^{\circ}\mathrm{C}$.

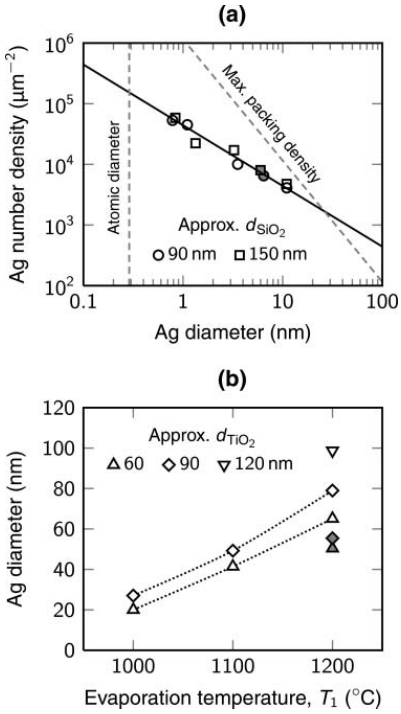

FIG. 8. (a) The number density of the decorative silver dots on a silica particle as a function of the diameter of the silver dots. (b) The diameter of the silver particle on a titania particle as a function of the evaporation temperature. In both figures, the open and gray markers represent results calculated from particles with and without the DMA selection, respectively.

materials, titania and silver, can be independently tuned in the composite doublet particles. Here, the size of the silver particles on the titania particles varied from approximately 20 to 100 nm.

The amount of the silver coating on an individual carrier particle depends on the amount of silver vapor, the size of the carrier particle, and the total CS of the carrier aerosol particles. In Figure 9a, the mass of silver in an individual approximately 90 nm silica and titania particle is presented as a function of the vapor pressure of silver, i.e., the amount of the evaporated silver controlled with the evaporation temperature. The two different carrier particle materials are comparable, as the size of the carrier particles and the total CSs are similar. We can see that for titania, the mass is directly proportional to the silver vapor pressure. For silica, this is not the case. At the lowest evaporation temperature (900 °C), the mass of silver on the different materials is quite similar, as seen also from the TEM micrographs (Figure 6). With higher temperatures, there is approximately an order of magnitude difference in the silver mass, until at the highest evaporation temperature, the relative difference decreases again. The observed results could be explained with the formation of the different sized silver structures on the silica and titania particles. That is, the condensation rate of silver on the silica carrier particles containing small silver nanodots is limited by the higher effective vapor pressure of silver. As larger silver structures are quickly formed on the titania particles, already at the evaporation temperature of 1000 °C (Figure 6), the condensation rate is no longer limited by this Kelvin effect.

The effect of the size of the carrier particles and the total CS for the mass of the silver coating on the titania particles

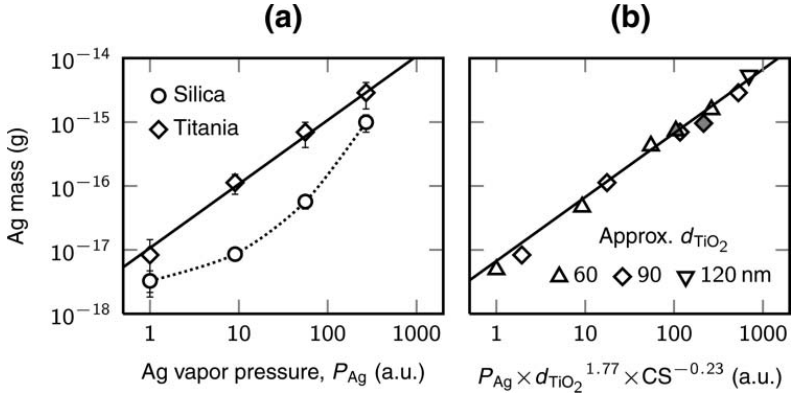

FIG. 9. (a) The mass of silver in a carrier particle as a function of the silver vapor pressure. The particle diameters (approximately 90 nm) and total CSs for both particle materials are similar. The error bars represent the standard deviation of several measurements. (b) The result of a minimization to find out the dependency between the silver mass and the diameter of the titania particle and the total CS. The open and gray markers represent results calculated from particles with and without the DMA selection, respectively.

was estimated using a least squares minimization. The minimized expression was

$$\sum \left[\log\left(a \times P_{\mathrm{Ag}} \times d_{\mathrm{TiO_2}}^{b} \times \mathrm{CS}^{c}\right) - \log\left(m_{\mathrm{Ag}}\right)\right]^2, \qquad [1]$$

where a, b, and c are the output parameters obtained from the minimization. The result derived from the minimization is shown in Figure 9b. We found that the mass is proportional to the diameter of the carrier particles with a power of 1.77 and to the total CS with a power of −0.23. The former exponent is close to the particle size dependency of the CS near 100 nm (Kuuluvainen et al. 2010). Furthermore, the total CS affects the mass in two ways. With higher total CS, the same amount of silver distributes to a larger particle population. However, a larger particle population also reduces the wall losses of the silver vapor. These two effects partially cancel each other, and therefore the dependency is rather small.

3.4. Formation of the Different Particle Morphologies

A schematic illustration showing the proposed routes for the formation of the different particle morphologies is presented in Figure 10. The TEM micrographs at the lowest evaporation temperature (Figure 6, $T_1 = 900\,^{\circ}\mathrm{C}$) suggest that the initial particle formation by heterogeneous nucleation and vapor condensation on the silica and titania particles are quite similar. With higher evaporation temperatures, vapor saturation, and thus the beginning of the condensation, is reached earlier. From Figure 3a, we can estimate that at the evaporation temperature of 1200 °C, the vapor begins to condensate at a temperature of approximately 1000 °C. Already at a temperature of 800 °C, over 99% of the available vapor has condensed. This temperature is reached between the first and the second heating zone; thus the second zone with the temperature of 600 °C acts as a sintering step (residence time approximately 3 s), where the formed silver particles can migrate on top of the carrier particles.

The two different particle morphologies suggest that the silver migration on the silica particles is rather slow compared to that of the titania particles, on which nearly all silver has been collected into a single large particle. Binder et al. (2010) conducted similar sintering experiments for palladium-decorated silica and titania particles, and found that the palladium particles grew faster on titania. They speculated that the rougher surface of the amorphous silica compared to that of the titania could hinder the palladium particle migration or even trap the particles. Especially, pores with sizes equivalent to the diameter of the decorative dots can increase their stability during the sintering (Bartholomew 2001). From Figure 8, we saw that the silver particle number density on silica decreased with the size of the Ag particles. Therefore, some particle migration, even though hindered, could be expected to have occurred in our system. In the case of palladium on silica, an increase in the particle size of approximately 50% was observed at 600 °C (Binder et al. 2010). Gold particles, on the other hand, remained stable on silica at temperatures under 900 °C (Boies et al. 2011). As it is challenging to estimate the sizes of the possible pores on the silica particles, thorough comparison with other studies might be difficult.

In the case of titania carrier particles, Binder et al. (2010) found that the size of the palladium dots had approximately doubled at a sintering temperature of 600 °C, nevertheless, maintaining their original decorated morphology. As palladium has considerably higher melting point than silver, we could expect that palladium particles are more stable on a support than silver (Bartholomew 2001). Also, as an indirect evidence of the particle migration, the TEM micrographs (Figure 6, T_1 = 1000–1100 °C) clearly show approximately

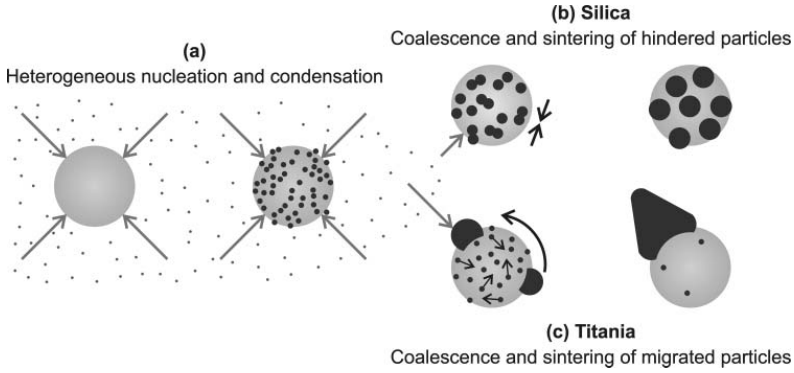

FIG. 10. A schematic illustration of the formation of the ceramic–silver composite particles with different morphologies. (a) The initial steps are similar for both silica and titania carrier particles. Due to the differences in the Ag particle migration on (b) silica and (c) titania, decoration and composite doublets, respectively, are formed.

10 nm silver particles merging into larger silver structures. In order to estimate whether the particle migration of such large particles is indeed relevant in our system, we can calculate the diffusion coefficient for a spherical 10 nm particle using the derivation presented for example by Harris (1995). With the literature values collected by Gontier-Moya et al. (2004), the diffusion coefficient of a 10 nm silver and palladium particle at 600 °C receives values of 2×10^{-9} and 7×10^{-15} cm^2s^{-1}, respectively. As a consequence, the migration distance in a time period of 3 s for silver and palladium particles could be estimated to be approximately 1.5 μm and 3 nm, respectively. Thus, in the light of these values, it is likely that the migration of the silver particles is the key factor controlling the particle morphology. Furthermore, the migration of silver particles is considerably faster than that of palladium particles, and therefore with silver on titania, the decorated morphology is not maintained. Instead, the silver forms larger structures through particle collisions and subsequent coalescence.

The silver particles observed on titania have a variety of different shapes, such as triangular, rodlike, and hexagonal (Figure 7). Similarly shaped metal particles on ceramic supports have been reported in earlier studies as a consequence of sintering (Wynblatt 1976; Kim and Ihm 1985; Harris 1986). Harris (1995) suggested that such shapes are formed by the abnormal growth of twinned structures, resulting from the coalescence of single crystals. Thus, the presence of these structures also implies that particle migration is really the key factor for the different particle morphologies. All in all, our coating process includes simultaneous condensation of new material on the carrier particles and on existing silver structures. The condensation rate is most likely affected by the size of the different silver structures, as speculated with Figure 9. In addition, metal–substrate related interactions between the formed silver particles and the ceramic carrier particle affect the particle migration and sintering. With the current coating setup, the complete distinction between all these different processes might be challenging.

4. CONCLUSIONS

Ceramic–silver composite nanoparticles were synthesized with a physical coating process. Silver was evaporated and condensated on silica and titania carrier particles in a tubular furnace flow system. The homogeneous nucleation of the evaporated silver vapor was avoided by optimizing the temperature gradient in the furnace system. The effect of the carrier particle material, particle size, total CS, and evaporation temperature on the formed silver coating was investigated.

We found that the different ceramic carrier particle materials, amorphous silica and crystalline titania, resulted in completely different coating morphologies. Typical silver-decoration was formed on the silica particles. Interestingly, the number density of the decorative silver dots on the silica was inversely proportional to the diameter of the dots. The dot size increased with the evaporation temperature from less than 1 to over 10 nm. Furthermore, the results suggest that a core–shell structure could form on the silica when using higher evaporation temperatures than in this study (>1200 °C).

On the titania carrier particles, the silver coating formed substantially larger nanostructures, with sizes ranging from approximately 20 to 100 nm, thus forming titania–silver composite doublets. Furthermore, it was possible to independently tailor the particle sizes of the two materials. The size of the silver particles increased with the evaporation temperature and carrier particle size, and decreased with the total CS of the carrier particles. The large silver structures consisting of different shapes, including triangular, rodlike, and hexagonal, suggest that the silver particles on the crystalline titania have grown due to the particle migration and coalescence. In the case of the amorphous silica, the rougher surface structure hindered the particle migration.

The coating process of ceramic carrier particles with silver used in this study is purely physical, and thus no chemical precursors are required. Furthermore, the amount of the coating material achieved is substantially larger than with the physical coating processes that rely on the coagulation of smaller metal particles and larger carrier particles. In addition, here the homogeneous nucleation of the coating material was avoided. We expect that the synthesized silica/titania–silver composite particles are relevant in different nanotechnology applications, such as optical, catalytic, and antibacterial.

FUNDING

Juha Harra acknowledges the TUT's graduate school for financial support.

REFERENCES

Ahonen, P. P., Joutsensaari, J., Richard, O., Tapper, U., Brown, D. P., Jokiniemi, J. K., and Kauppinen, E. I. (2001). Mobility Size Development and the Crystallization Path during Aerosol Decomposition Synthesis of TiO_2 Particles. *J. Aerosol Sci.*, 32(5): 615–630.

Alcock, C. B., Itkin, V. P., and Horrigan, M. K. (1984). Vapour Pressure Equations for the Metallic Elements: 298–2500K. *Can. Metall. Quart.*, 23(3): 309–313.

Arffman, A., Kuuluvainen, H., Harra, J., Vuorinen, O., Juuti, P., Yli-Ojanperä, J., Mäkelä, J. M., and Keskinen, J. (2015). The Critical Velocity of Rebound Determined for Sub-micron Silver Particles with a Variable Nozzle Area Impactor. *J. Aerosol Sci.*, 86: 32–43.

Arffman, A., Yli-Ojanperä, J., Kalliokoski, J., Harra, J., Pirjola, L., Karjalainen, P., Rönkkö, T., and Keskinen, J. (2014). High-resolution Low-Pressure Cascade Impactor. *J. Aerosol Sci.*, 78: 97–109.

Aromaa, M., Arffman, A., Suhonen, H., Haapanen, J., Keskinen, J., Honkanen, M., Nikkanen, J.-P., Levänen, E., Messing, M. E., Deppert, K., Teisala, H., Tuominen, M., Kuusipalo, J., Stepien, M., Saarinen, J. J., Toivakka, M., and Mäkelä, J. M. (2012). Atmospheric Synthesis of Superhydrophobic TiO_2 Nanoparticle Deposits in a Single Step Using Liquid Flame Spray. *J. Aerosol Sci.*, 52: 57–68.

Aromaa, M., Keskinen, H., and Mäkelä, J. M. (2007). The Effect of Process Parameters on the Liquid Flame Spray Generated Titania Nanoparticles. *Biomol. Eng.*, 24(5): 543–548.

Backman, U., Tapper, U., and Jokiniemi, J. K. (2004). An Aerosol Method to Synthesize Supported Metal Catalyst Nanoparticles. *Synth. Met.*, 142(1–3): 169–176.

Bartholomew, C. H. (2001). Mechanisms of Catalyst Deactivation. *Appl. Catal. A.*, 212(1–2): 17–60.

Binder, A., Heel, A., and Kasper, G. (2007). Deposition of Palladium Nanodots of Controlled Size and Density Onto Surface-Modified SiO_2 Particles by an Atmospheric Pressure CVS/MOCVD Process. *Chem. Vap. Deposition*, 13(1): 48–54.

Binder, A., Seipenbusch, M., and Kasper, G. (2010). Sintering of Pd Catalyst Particles on SiO_2–TiO_2 Carrier Particles of Different Mixing Ratios. *J. Phys. Chem. C.*, 114(17): 7816–7821.

Boies, A. M., Lei, P., Calder, S., and Girshick, S. L. (2011). Gas-Phase Production of Gold-Decorated Silica Nanoparticles. *Nanotechnology*, 22(31): 315603.

Eggersdorfer, M. L., and Pratsinis, S. E. (2014). Agglomerates and Aggregates of Nanoparticles Made in the Gas Phase. *Adv. Powder Technol.*, 25(1): 71–90.

Faust, M., Enders, M., Bruns, M., Bräse, S., Gao, K., and Seipenbusch, M. (2013). Synthesis of Nanostructured Pt/Oxide Catalyst Particles by MOCVD Process at Ambient Pressure. *Surf. Coat. Technol.*, 230: 284–289.

Goertz, V., Weis, F., Keln, E., Nirschl, H., and Seipenbusch, M. (2011). The Effect of Water Vapor on the Particle Structure and Size of Silica Nanoparticles during Sintering. *Aerosol Sci. Technol.*, 45(11): 1287–1293.

Gontier-Moya, E. G., Beszeda, I., and Moya, F. (2004). Comparisons of Parameters Involved in Mass Transport and Desorption at the Surface of Noble Metals and Sapphire. *Sur. Sci.*, 566–568: 148–154.

Haapanen, J., Aromaa, M., Teisala, H., Tuominen, M., Stepien, M., Saarinen, J. J., Heikkilä, M., Toivakka, M., Kuusipalo, J., and Mäkelä, J. M. (2015). Binary TiO_2/SiO_2 Nanoparticle Coating for Controlling the Wetting Properties of Paperboard. *Mater. Chem. Phys.*, 149–150: 230–237.

Harra, J., Mäkitalo, J., Siikanen, R., Virkki, M., Genty, G., Kobayashi, T., Kauranen, M., and Mäkelä, J. M. (2012). Size-Controlled Aerosol Synthesis of Silver Nanoparticles for Plasmonic Materials. *J. Nanopart. Res.*, 14 (6): 870.

Harra, J., Nikkanen, J.-P., Aromaa, M., Suhonen, H., Honkanen, M., Salminen, T., Heinonen, S., Levänen, E., and Mäkelä, J. M. (2013). Gas Phase Synthesis of Encapsulated Iron Oxide–Titanium Dioxide Composite Nanoparticles by Spray Pyrolysis. *Powder Technol.*, 243: 46–52.

Harris, P. J. F. (1986). The Sintering of Platinum Particles in an Alumina-Supported Catalyst: Further Transmission Electron Microscopy Studies. *J. Catal.*, 97(2): 527–542.

Harris, P. J. F. (1995). Growth and Structure of Supported Metal Catalyst Particles. *Int. Mater. Rev.*, 40(3): 97–115.

Height, M. J., Pratsinis, S. E., Mekasuwandumrong, O., and Praserthdam, P. (2006). Ag-ZnO Catalysts for UV-Photodegradation of Methylene Blue. *Appl. Catal. B*, 63(3–4): 305–312.

Järvinen, A., Aitomaa, M., Rostedt, A., Keskinen, J., and Yli-Ojanperä, J. (2014). Calibration of the New Electrical Low Pressure Impactor (ELPI+). *J. Aerosol Sci.*, 69: 150–159.

Järvinen, A., Kuuluvainen, H., Niemi, J., Saari, S., Dal Maso, M., Pirjola, L., Hillamo, R., Janka, K., Keskinen, J., and Rönkkö, T. (2015). Monitoring Urban Air Quality with a Diffusion Charger Based Electrical Particle Sensor. *Urban Climate*, doi:10.1016/j.uclim.2014.10.002.

Kasper, G. (1983). Note on the Slip Coefficient of Doublets of Spheres. *J. Aerosol Sci.*, 14(6): 753–754.

Keskinen, H., Mäkelä, J. M., Aromaa, M., Ristimäki, J., Kanerva, T., Levänen, E., Mäntylä, T., and Keskinen, J. (2007). Effect of Silver Addition on the Formation and Deposition of Titania Nanoparticles Produced by Liquid Flame Spray. *J. Nanopart. Res.*, 9(4): 569–588.

Keskinen, H., Mäkelä, J. M., Heikkinen, R., Suopanki, A., and Keskinen, J. (2007). Synthesis of Pd–Alumina and Pd–Lanthana Suspension for Catalytic Applications by One-Step Liquid Flame Spray. *Catal. Lett.*, 119 (1–2): 172–178.

Keskinen, J., Pietarinen, K., and Lehtimäki, M. (1992). Electrical Low Pressure Impactor. *J. Aerosol Sci.*, 23(4): 353–360.

Kim, K.-T., and Ihm, S.-K. (1985). Sintering Behavior of Nickel Particles Supported on Alumina Model Catalyst in Hydrogen Atmosphere. *J. Catal.*, 96 (1): 12–22.

Krinke, T. J., Deppert, K., Magnusson, M. H., Schmidt, F., and Fissan, H. (2002). Microscopic Aspects of the Deposition of Nanoparticles from the Gas Phase. *J. Aerosol Sci.*, 33(10): 1341–1359.

Kuuluvainen, H., Arffman, A., Saukko, E., Virtanen, A., and Keskinen, J. (2013). A New Method for Characterizing the Bounce and Charge Transfer Properties of Nanoparticles. *J. Aerosol Sci.*, 55: 105–115.

Kuuluvainen, H., Kannosto, J., Virtanen, A., Mäkelä, J. M., Kulmala, M., Aalto, P., and Keskinen, J. (2010). Technical Note: Measuring Condensation Sink and Ion Sink of Atmospheric Aerosols with the Electrical Low Pressure Impactor (ELPI). *Atmos. Chem. Phys.*, 10: 1361–1368.

Lu, Z. G., and Zhu, J. H. (2007). Thermal Evaporation of Pure Ag in SOFC-Relevant Environments. *Electrochem. Solid State Lett.*, 10(10): B179–B182.

Mädler, L., Roessler, A., Pratsinis, S. E., Sahm, T., Gurlo, A., Barsan, N., and Weimar, U. (2006). Direct Formation of Highly Porous Gas-Sensing Films by In Situ Thermophoretic Deposition of Flame-Made Pt/SnO_2 Nanoparticles. *Sens. Actuators B*, 114(1): 283–295.

Pfeiffer, T. V., Feng, J., and Schmidt-Ott, A. (2014). New Developments in Spark Production of Nanoparticles. *Adv. Powder Technol.*, 25(1): 56–70.

Pfeiffer, T. V., Kedia, P., Messing, M. E., Valvo, M., and Schmidt-Ott, A. (2015). Precursor-Less Coating of Nanoparticles in the Gas Phase. *Materials*, 8(3): 1027–1042.

Sigmund, S., Yu, M., Meyer, J., and Kasper, G. (2014). An Aerosol-Based Process for Electrostatic Coating of Particle Surfaces with Nanoparticles. *Aerosol Sci. Technol.*, 48(2): 142–149.

Sotiriou, G. A., Teleki, A., Camenzind, A., Krumeich, F., Meyer, A., Panke, S., and Pratsinis, S. E. (2011). Nanosilver on Nanostructured Silica: Antibacterial Activity and Ag Surface Area. *Chem. Eng. J.*, 170(2–3): 547–554.

Teoh, W. Y., Amal, R., and Mädler, L. (2010). Flame Spray Pyrolysis: An Enabling Technology for Nanoparticles Design and Fabrication. *Nanoscale*, 2: 1324–1347.

Tikkanen, J., Gross, K. A., Berndt, C. C., Pitkänen, V., Keskinen, J., Raghu, S., Rajala, M., and Karthikeyan, J. (1997). Characteristics of the Liquid Flame Spray Process. *Surf. Coat. Technol.*, 90(3): 210–216.

Wynblatt, P. (1976). Particle Growth in Model Supported Metal Catalysts—II. Comparison of Experiment with Theory. *Acta Metallurgica*, 24(12): 1175–1182.

Yli-Ojanperä, J., Mäkelä, J. M., Marjamäki, M., Rostedt, A., and Keskinen, J. (2010). Towards Traceable Particle Number Concentration Standard: Single Charged Aerosol Reference (SCAR). *J.Aerosol Sci.*, 41(8): 719–728.

Zdanowicz, M., Harra, J., Mäkelä, J. M., Heinonen, E., Ning, T., Kauranen, M., and Genty, G. (2013). Ordered Multilayer Silica-Metal Nanocomposites for Second-Order Nonlinear Optics. *Appl. Phys. Lett.*, 103(25): 251907.

Zdanowicz, M., Harra, J., Mäkelä, J. M., Heinonen, E., Ning, T., Kauranen, M., and Genty, G. (2014). Second-Harmonic Response of Multilayer Nanocomposites of Silver-Decorated Nanoparticles and Silica. *Sci. Rep.*, 4: 5745.

Zihlmann, S., Lüönd, F., and Spiegel, J. K. (2014). Seeded Growth of Monodisperse and Spherical Silver Nanoparticles. *J. Aerosol Sci.*, 75: 81–93.

Paper IV

Mariusz Zdanowicz, Juha Harra, Jyrki M. Mäkelä, Esa Heinonen,
Tingyin Ning, Martti Kauranen, and Goëry Genty

"Ordered multilayer silica-metal nanocomposites
for second-order nonlinear optics"

Applied Physics Letters, vol. 103, no. 25, p. 251907, 2013

doi: 10.1063/1.4852795

Ordered multilayer silica-metal nanocomposites for second-order nonlinear optics

Mariusz Zdanowicz,[1,a)] Juha Harra,[1,b)] Jyrki M. Mäkelä,[1] Esa Heinonen,[2] Tingyin Ning,[1] Martti Kauranen,[1] and Goëry Genty[1]
[1]*Department of Physics, Tampere University of Technology, P.O. Box 692, FI-33101 Tampere, Finland*
[2]*Center of Microscopy and Nanotechnology, University of Oulu, P.O. Box 7150, FI-90014, Finland*

(Received 22 October 2013; accepted 6 December 2013; published online 18 December 2013)

We use aerosol synthesis to fabricate ordered metal-silica nanocomposites consisting of alternating layers of pure silica and silica nanoparticles decorated with silver nanodots. These multilayer structures preserve the narrow plasmon resonance of the nanodots even for high optical densities and allow second-harmonic generation due to spontaneous symmetry breaking arising from the interfaces between silica and nanoparticle layers. Our concept opens up perspectives for complex structures for advanced optical applications. © *2013 AIP Publishing LLC*. [http://dx.doi.org/10.1063/1.4852795]

The optical responses of metal nanoparticles arise from the plasmonic oscillations of their conduction electrons. The resulting localized surface plasmon (LSP) resonances give rise to strong electromagnetic fields near the metal-dielectric interface. Such local-field enhancement has many attractive applications in biosensing,[1,2] imaging,[3,4] and solar cells.[5,6] In addition, the plasmon resonances depend sensitively on the particle size,[7,8] shape,[9–12] as well as their dielectric environment, allowing broad tailorability of the resonances for a given application.

The local-field enhancement is particularly important for nonlinear optical effects, which scale with a high power of the field. Indeed, enhancement of third-order effects, with no particular symmetry constraints, has been demonstrated in bulk-type metal-dielectric nanocomposites.[13,14] Second-order effects, such as second harmonic generation (SHG), on the other hand, require non-centrosymmetric samples, and their observation has so far been limited to surface geometries. Enhancement of SHG by rough metal surfaces was demonstrated early on in a traditional surface geometry where the incident beam is applied on the sample at oblique angle.[15] More recently, lithographic arrays of non-centrosymmetric particles have been introduced as second-order metamaterials whose response can be accessed at normal incidence,[16–19] but such samples are not easy to fabricate.

The nonlinear responses (both second and third-order) of a macroscopic sample can be enhanced by tuning the incident laser close to the plasmon resonance of the particles[20,21] or by increasing the density of the particles. Unfortunately, the latter approach spoils the quality (shape and linewidth) of the resonances either due to agglomeration of particles, which gives rise to inhomogeneous broadening,[22,23] or because of near field coupling.[24] An associated problem is the difficulty of fabricating bulk-type composite materials with the required non-centrosymmetry for second-order. For other types of materials, the organic ones in particular, the non-centrosymmetry can be induced afterwards by poling in an electric field[25] or by using self-assembly, which in some cases gives rise to a non-centrosymmetric structure.[26] With regard to metal nanostructures, the focus has been on the plasmonic enhancement of the nonlinearity,[27] but no methods have been demonstrated for fabricating thick non-centrosymmetric structures.

Nanoparticle synthesis by aerosol techniques is fairly inexpensive, simple, highly versatile, and also scalable.[28,29] Particles can be generated in a continuous process and deposited directly from the gas phase onto the desired substrate. Recently, aerosol techniques have been used to produce plasmonic metal nanoparticles from different materials and with various morphologies.[23,30,31] In addition, the synthesized nanoparticles have been incorporated into multilayer polymer films in order to achieve for example magnetic and plasmonic functionalities.[32] However, even though aerosol synthesized nanoparticles have been studied extensively using linear spectroscopy, their applicability in nonlinear optical materials remains to be explored.

In this Letter, we use aerosol techniques to fabricate ordered multilayer metal-silica nanocomposites with controllable linear and nonlinear optical responses. Our nanocomposites consist of alternating layers of silver-decorated silica particles and pure silica glass. The fabrication technique allows for precise control of the synthesis and deposition of the silver-decorated particles, thus preventing the formation of silver clusters and resulting in samples with reproducible optical properties. The shape of the plasmon resonance in the extinction spectrum of the ordered composites is perfectly maintained during the layer growth and its amplitude grows linearly as the number of layers increases. Significantly, we further show that symmetry is inherently broken due to interfaces between pure silica and a layer of decorated nanoparticles, resulting in spontaneous growth of a non-centrosymmetric structure and a SHG signal that increases with the number of layers. The SHG is dramatically larger than that observed from a single layer of decorated particles with equivalent thickness.

Silver-decorated silica nanoparticles (Fig. 1(a)) were synthesized in a continuous flow of nitrogen. The silica particles generated by chemical vapor synthesis from liquid tetraethyl orthosilicate (TEOS)[33] were subsequently sintered in

[a)]Also at Transmission and Optical Technologies Department, National Institute of Telecommunications, Szachowa Str. 1, 04-894 Warsaw, Poland.; Electronic mail: mariusz.zdanowicz@tut.fi.
[b)]M. Zdanowicz and J. Harra contributed equally to this work.

IV

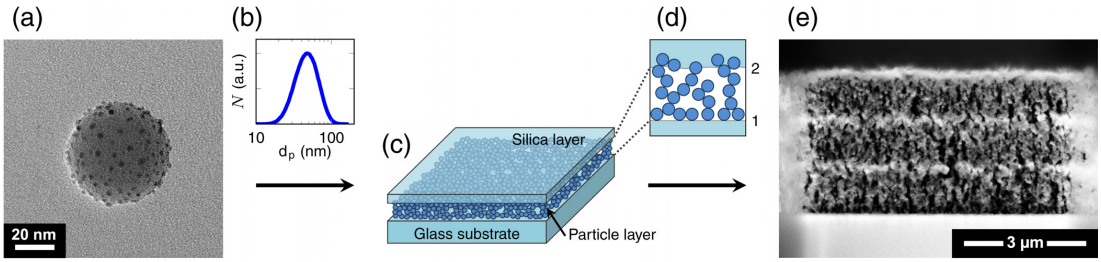

FIG. 1. (a) TEM image of a silver-decorated silica nanoparticle. (b) Size distribution of the silica particles (note the log scale in the horizontal axis). (c) Schematic image of one layer, which consist of a particle layer covered by a pure silica layer. (d) Schematic image of two neighboring interfaces explaining the symmetry breaking. (e) TEM image of the cross-section of a fabricated three-layer sample.

IV

a tubular high-temperature furnace in order to obtain spherical carrier particles. Figure 1(b) shows the log-normal size distribution of the sintered silica particles, measured with a scanning mobility particle size (SMPS),[34] with a geometric mean diameter of 50 nm and a geometric standard deviation of 1.4. The silver decoration on the silica carrier particles was achieved by evaporation and subsequent condensation of silver from a small piece of bulk material.[31] This resulted in the formation of silver nanodots with diameters of 1–2 nm. The synthesized silver-decorated silica particles were then deposited from the gas phase onto glass substrates (1 mm thick microscope glass slides) by electrostatic collection.[35] The circular particle collection area on the substrate had a diameter of 2 cm.

The thickness of the particle layer on the substrate depends on collection time. Here, the collection time was set to 30 min, corresponding to particle layer thickness of approximately 1 μm with an estimated porosity of over 90%. This rough evaluation is based on the aerosol measurements (particle size and number concentration), particle collection parameters (gas flow rate, collection area and time) and realized layer thickness. Moreover, our estimation is consistent with previous reports of high porosity values for dry deposition of nanoparticles.[36] The layer of decorated nanoparticles was subsequently covered with a layer of pure silica using an electron-beam dielectric coater and with thickness, here approximately 200 nm, also determined by the deposition time (Fig. 1(c)). Repeating the particle deposition and coating processes multiple times and with identical deposition times allowed us to fabricate ordered multilayer nanocomposites whose linear and nonlinear optical properties can be controlled via the number of layers. Because the layer of silver-decorated particles is very porous, the silica coating penetrates it. However, the silica coating diffuses much less towards the bottom of the particle layer, and hence the overall symmetry of each layer is broken between the bottom and top interfaces (1 and 2, respectively, in Fig. 1(d)). Because each individual layer exhibits the same type of asymmetry the SHG response can grow significantly with the number of layers. In what follows, we use the term layer to refer to the combination of a single layer of decorated particles coated with a silica layer. Figure 1(e) shows a transmission electron microscope (TEM) image of the cross-section of a fabricated nanocomposite with three layers where the alternating layers of decorated nanoparticles and silica can be identified.

We first examined the linear optical properties of the fabricated samples. For this purpose, we measured their extinction spectra as a function of the number of layers with a high-sensitivity, high-resolution UV-Vis-NIR spectrophotometer (Shimadzu UV-3600). First, we clearly identify in each case the typical plasmon resonance of silver particles centered at around 370 nm (Fig. 2(a)) indicating the absence of silver clusters that would significantly broaden the resonance. Significantly, we also see how the magnitude of the extinction maximum grows linearly with the number of layers (see inset in Fig. 2(a)) and how the spectral location and width of the plasmon resonance remain unchanged with the number of layers. Oscillations visible for the wavelength

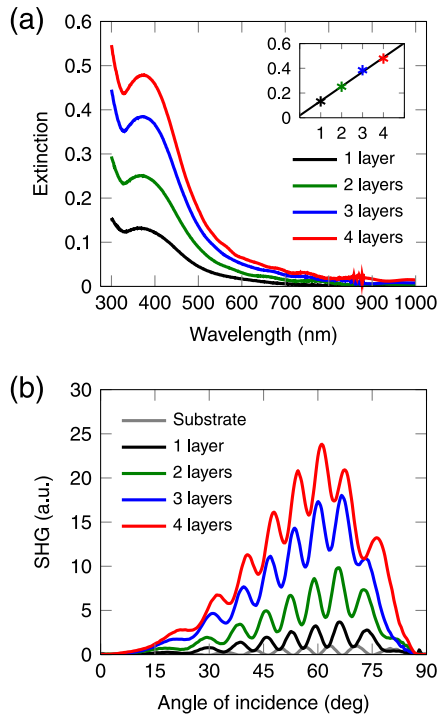

FIG. 2. (a) Extinction spectra of the multilayer nanocomposites. The inset shows the maximum extinction as a function of the number of layers. (b) Second-harmonic signal generated as a function of the angle of incidence.

TABLE I. Normalized SHG signals for different input-output polarization configurations.

p_{in}–p_{out}	s_{in}–p_{out}	p_{in}–s_{out}	s_{in}–s_{out}
1	8.9×10^{-2}	4.4×10^{-3}	0.7×10^{-3}

above 600 nm arise from weak Fabry-Perot effects within the active layers.

We then proceeded to investigate the second-order nonlinear response of the multilayer composites. The nonlinear response was characterized by measuring the SHG response as a function of the incidence angle in a Maker-fringe setup.[37,38] The fundamental beam was derived from a Nd:YAG laser producing 70 ps pulses at 1 kHz repetition rate and with 1064 nm wavelength. A 25 cm focal-length lens was used to weakly focus the beam into a spot size of around 20 μm at the sample plane, leading to the generation of SHG radiation at the 532 nm wavelength. Any potential SHG from the laser itself was removed with a long-pass IR filter inserted before the sample. The fundamental beam was blocked after the sample with a combination of a short-pass filter and an interference filter (central wavelength 532 nm, bandwidth 10 nm). The transmitted SHG signal was detected by a photomultiplier tube and the polarization states of the fundamental and SHG beams were controlled with calcite Glan polarizers. The sample was mounted on a high precision rotation stage to detect the SHG as a function of the angle of incidence. The SHG signal was found to be a highly directional beam, thus verifying the coherent character of the process.

The measurements were performed for samples consisting of 1 to 4 layers, for various polarization configurations and the maximum SHG was observed for the input and output polarizations parallel to the plane of incidence (p_{in}–p_{out} configuration, Table I). Very weak SHG signals for the p_{in}–s_{out} and s_{in}–s_{out} combinations suggest that the sample is isotropic in the plane of the sample as expected due to the fabrication process. In order to eliminate the possible influence of inhomogeneity in the sample plane, a series of measurements were conducted at ten different spatial locations on the samples. The SHG intensity was then averaged over all ten measurements. The results (Fig. 2(b)) show that the maximum of the SHG signal occurs for an incidence angle of approximately 60°. Most importantly, the strength of the SHG signal increases with the number of layers in the sample. The Maker-fringes are also clearly observed and result from interference between the SHG signals arising from the back side of the 1 mm thick glass substrate. The thickness of any composite itself is much smaller than that of the substrate and their effect on the Maker-fringes cannot be resolved. The shift of the SHG signal maximum originates from the fact that that the values of the susceptibility components for the active layers and the bottom surface of the substrate are different. As the active layer becomes thicker, its response becomes more important giving rise to changes in the fringe structure.

In order to evaluate the origin of the second-order response of the structures, we fabricated two additional control samples (see Fig. 3(a) for a schematic illustration). The first (CS1) consists of a single layer of silver-decorated particles coated with one layer of silica on top. Both layers were deposited so as to match the effective thicknesses of the respective layers in the four-layer sample. The other control sample (CS2), was prepared by depositing four layers of silica particles with no silver decoration. The collection time for the silica particles and the thickness of the deposited silica were identical to those of the four-layer sample with the silver decoration. The purpose of these two samples is two-fold: CS1 allows us to investigate the effect of structuring the samples into multiple layers whilst CS2 allows verifying the role of the silver particles in the nonlinear response.

We first compare in Fig. 3(b) the extinction spectra of the control samples and the four-layer sample. The linear response of the samples is seen to be essentially independent of the exact layer structure and only depends on the total silver and silica content. This can be understood from the fact that the only parameter that determines the overall extinction is the total amount of silver dots and silica and not the particular arrangement within the sample. This is an important result as it implies that any differences in the nonlinear response can be ascribed to the structuring of the samples into multiple layers. On the other hand, in the linear response of CS2 with no silver inclusions, we note, as expected, the absence of the plasmon resonance with an increase in the extinction for decreasing wavelengths consistent with typical silica absorption. These results clearly show that the extinction of the samples with silver-decorated particles is

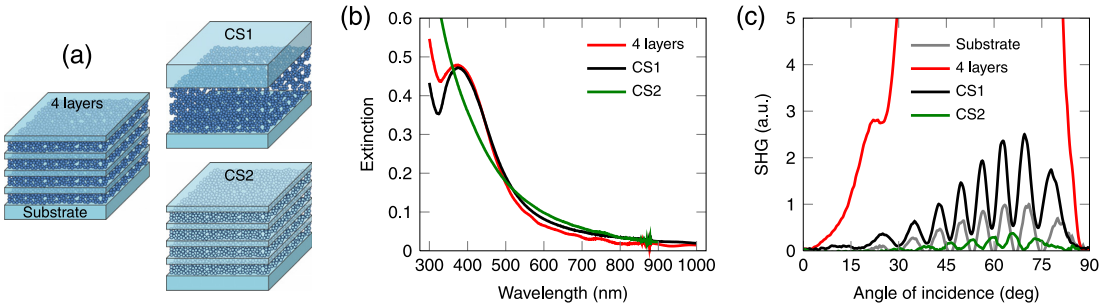

FIG. 3. (a) Schematic images of the multilayer nanocomposites and control samples. (b) Comparison of the extinction spectra between the four-layer sample and the control samples: CS1 with equivalent amount of metal and silica and CS2 with layers organized identically with four-layer structure, but without silver inclusions. (c) Comparison of the SH signal for the four-layer sample and the control samples CS1 and CS2.

dominated by the plasmon resonance as determined by the silver particle size and their total amount.

We subsequently performed the Maker-fringe experiments for the control samples under conditions identical to that of the multilayer composites. The results are presented in Fig. 3(c) along with the SHG intensity obtained from the four-layer structure and from the sole substrate. We first note that CS2 containing no decorated particles produces negligible SHG. In fact, the SHG signal from CS2 is even weaker than that from the substrate itself. On the other hand, CS1, which contains decorated particles, shows an increase in SHG compared to CS2 or the substrate, showing evidence of the importance of the silver nanoparticles in the SHG process. But most importantly, the SHG signal is more than order of magnitude weaker than that generated from the four-layer sample with the same quantity of silver. This is a truly remarkable result illustrating that (i) the multilayer structure plays a central role in enhancing SHG and (ii) SHG arises from the multiple coherent second-harmonic contributions induced by the symmetry-breaking arising from the differences between the top and bottom interfaces of each layer.

IV

The SHG response from the multilayer samples can be modeled by assuming that each individual layer of silver-decorated nanoparticles covered with a silica layer is equivalent to a thin film source of SHG signal. Within this approximation and because the thickness of each layer is identical, the amplitude of the elementary SHG field generated from each layer is the same. With this model, we can express the total SHG field as $E_{SHG} = C(1 + Nb)$, where E_{SHG} represents the total SHG field generated within a nanocomposite with N active layers. Here, C is the normalization constant representing the SHG contribution from the back side of the substrate[39,40] and b is the contribution from one nanocomposite layer normalized to the response of the substrate. Note that to account for the possible phase differences in the elementary metal-dielectric sources, we allow b to be complex. The corresponding total intensity is given by $I_{SHG} = C^2|1 + Nb|^2$ and the measured SHG intensity averaged over all angles of incidence was fitted with this model as a function of the number of layers. The result (Fig. 4) shows excellent agreement with the experiment. The contribution from the thin film source manifested by parameter b exceeds that from the substrate which is normalized to 1, consistent with the observations of Fig. 3(c). Corresponding value of the conversion efficiency of the second-order process was estimated to be of the order of 10^{-12} for the 4-layer sample, based on the experimental data. We also remark that the imaginary part of b is extremely small (1.1×10^{-5}), which is consistent with the fact that the SHG wavelength of 532 nm is significantly detuned from the plasmon resonance (see Fig. 3(b)). In principle and according to our model, the strength of the SHG signal could be boosted even more by depositing more active layers in the structure. In fact, with our thickest four-layer sample, we already observe 43-fold stronger SHG signal than the one measured for the substrate (see Fig. 4). In addition, the structures prepared for the present experiments are non-optimized. Therefore we expect that further development and optimization process allows the second-order response to be increased even more.

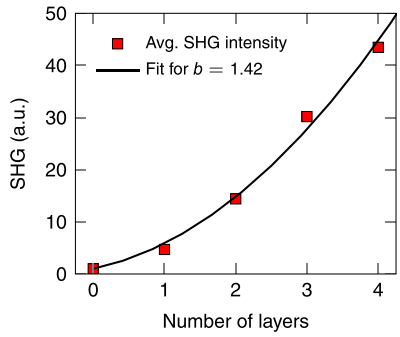

FIG. 4. Average SHG intensity as a function of the number of layers. Zero layers correspond to the substrate. The black line shows a fit with a model that separates contributions from the substrate and layers of the nanocomposite.

In conclusion, we have introduced a concept for the fabrication of silica-metal nanocomposites with controllable linear and nonlinear optical properties. Aerosol synthesis techniques were used to fabricate nanoparticle structures with enhanced nonlinear optical properties. The fabrication process allows creating ordered multilayer structures that preserve the shape of the plasmon resonance independently of the number of layers. We have further shown that separating multiple layers of decorated nanoparticles by silica results in an overall non-centrosymmetry that leads to second-harmonic generation that scales with the number of layers. Due to the flexibility of the used aerosol synthesis techniques, the material as well as the size of the carrier particles and the decorative nanodots can be varied to obtain nanocomposites with different optical responses (linear and nonlinear).

This work was supported by the Academy of Finland (136080 and 134980). M. Z. acknowledges the Wihuri Foundation for financial support. The authors thank Dr. Mari Honkanen (Department of Materials Science, Tampere University of Technology) for electron microscopy imaging, and Antti Rantamäki (Optoelectronics Research Centre, Tampere University of Technology) for preparing silica layers on the samples.

[1]T. Okamoto, I. Yamaguchi, and T. Kobayashi, Opt. Lett. **25**, 372 (2000).
[2]J. J. Mock, D. R. Smith, and S. Schultz, Nano Lett. **3**, 485 (2003).
[3]A. Holden, Photonics Nanostruct. Fundam. Appl. **3**, 96 (2005).
[4]J. B. Pendry, Phys. Rev. Lett. **85**, 3966 (2000).
[5]M. A. Green and S. Pillai, Nature Photonics **6**, 130 (2012).
[6]A. Pors, A. V. Uskov, M. Willatzen, and I. E. Protsenko, Opt. Commun. **284**, 2226 (2011).
[7]J. J. Mock, S. J. Oldenburg, D. R. Smith, D. A. Schultz, and S. Schultz, Nano Lett. **2**, 465 (2002).
[8]J. R. Heath, Phys. Rev. B **40**, 9982 (1989).
[9]J. Krenn, G. Schider, W. Rechberger, B. Lamprecht, A. Leitner, F. Aussenegg, and J. Weeber, Appl. Phys. Lett. **77**, 3379 (2000).
[10]N. J. Halas, Nano Lett. **10**, 3816 (2010).
[11]S. A. Maier, *Plasmonics: Fundamentals and Applications* (Springer, 2008).
[12]H. Husu, J. Mäkitalo, J. Laukkanen, M. Kuittinen, and M. Kauranen, Opt. Express **18**, 16601 (2010).
[13]J. E. Sipe and R. W. Boyd, Phys. Rev. A **46**, 1614 (1992).
[14]R. W. Boyd and J. E. Sipe, J. Opt. Soc. Am. B **11**, 297 (1994).
[15]C. K. Chen, A. R. B. de Castro, and Y. R. Shen, Phys. Rev. Lett. **46**, 145 (1981).

[16]H. Tuovinen, M. Kauranen, K. Jefimovs, P. Vahimaa, T. Vallius, J. Turunen, N.-V. Tkachenko, and H. Lemmetyinen, J. Nonlinear Opt. Phys. Mater. **11**, 421 (2002).
[17]S. Kujala, B. K. Canfield, M. Kauranen, Y. Svirko, and J. Turunen, Phys. Rev. Lett. **98**, 167403 (2007).
[18]R. Czaplicki, M. Zdanowicz, K. Koskinen, J. Laukkanen, M. Kuittinen, and M. Kauranen, Opt. Express **19**, 26866 (2011).
[19]M. W. Klein, C. Enkrich, M. Wegener, and S. Linden, Science **313**, 502 (2006).
[20]F. Niesler, N. Feth, S. Linden, J. Niegemann, J. Gieseler, K. Busch, and M. Wegener, Opt. Lett. **34**, 1997 (2009).
[21]M. Hentschel, T. Utikal, H. Giessen, and M. Lippitz, Nano Lett. **12**, 3778 (2012).
[22]G. Xu, M. Tazawa, P. Jin, and S. Nakao, Appl. Phys. A **80**, 1535 (2005).
[23]J. Harra, J. Mäkitalo, R. Siikanen, M. Virkki, G. Genty, T. Kobayashi, M. Kauranen, and J. M. Mäkelä, J. Nanopart. Res. **14**, 870 (2012).
[24]S. Linden, F. B. P. Niesler, J. Förstner, Y. Grynko, T. Meier, and M. Wegener, Phys. Rev. Lett. **109**, 015502 (2012).
[25]D. M. Burland, R. D. Miller, and C. A. Walsh, Chem. Rev. **94**, 31 (1994).
[26]S. I. Stupp, V. LeBonheur, K. Walker, L. S. Li, K. E. Huggins, M. Keser, and A. Amstutz, Science **276**, 384 (1997).
[27]K. Chen, C. Durak, J. R. Heflin, and H. D. Robinson, Nano Lett. **7**, 254 (2007).
[28]A. Gurav, T. Kodas, T. Pluym, and Y. Xiong, Aerosol Sci. Technol **19**, 411 (1993).
[29]F. Kruis, H. Fissan, and A. Peled, J. Aerosol Sci. **29**, 511 (1998).
[30]G. A. Sotiriou, T. Sannomiya, A. Teleki, F. Krumeich, J. Vörös, and S. E. Pratsinis, Adv. Funct. Mater. **20**, 4250 (2010).
[31]A. M. Boies, P. Lei, S. Calder, and S. L. Girshick, Nanotechnology **22**, 315603 (2011).
[32]G. A. Sotiriou, C. O. Blattmann, and S. E. Pratsinis, Adv. Funct. Mater. **23**, 34 (2013).
[33]A. Binder, A. Heel, and G. Kasper, Chem. Vap. Deposition **13**, 48 (2007).
[34]S. C. Wang and R. C. Flagan, Aerosol Sci. Technol. **13**, 230 (1990).
[35]T. J. Krinke, K. Deppert, M. H. Magnusson, F. Schmidt, and H. Fissan, J. Aerosol Sci. **33**, 1341 (2002).
[36]L. Mädler, A. Roessler, S. Pratsinis, T. Sahm, A. Gurlo, N. Barsan, and U. Weimar, Sens. Actuators B **114**, 283 (2006).
[37]P. D. Maker, R. W. Terhune, M. Nisenoff, and C. M. Savage, Phys. Rev. Lett. **8**, 21 (1962).
[38]J. Jerphagnon and S. K. Kurtz, J. Appl. Phys. **41**, 1667 (1970).
[39]The literature values for the surface susceptibility of glass vary but are on the order of 10^{-22} m^2/V, see Ref. 40.
[40]F. J. Rodriguez, F. X. Wang, and M. Kauranen, Opt. Express **16**, 8704 (2008).

Tampereen teknillinen yliopisto
PL 527
33101 Tampere

Tampere University of Technology
P.O.B. 527
FI-33101 Tampere, Finland

ISBN 978-952-15-3628-1
ISSN 1459-2045